Check for updates

Wide-Bandgap Perovskite-Inspired Materials: Defect-Driven Challenges for High-Performance Optoelectronics

G. Krishnamurthy Grandhi, David Hardy, Mokurala Krishnaiah, Brenda Vargas, Basheer Al-Anesi, Mahesh P. Suryawanshi, Diego Solis-Ibarra, Feng Gao, Robert L. Z. Hoye, and Paola Vivo*

The remarkable success of lead halide perovskites (LHPs) in photovoltaics and other optoelectronics is significantly linked to their defect tolerance, although this correlation remains not fully clear. The tendency of LHPs to decompose into toxic lead-containing compounds in the presence of humid air calls for the need of low-toxicity LHP alternatives comprising of cations with stable oxidation states. To this aim, a plethora of low-dimensional and wide-bandgap perovskite-inspired materials (PIMs) are proposed. Unfortunately, the optoelectronic performance of PIMs currently lags behind that of their LHP-based counterparts, with a key limiting factor being the high concentration of defects in PIMs, whose rich and complex chemistry is still inadequately understood. This review discusses the defect chemistry of relevant PIMs belonging to the halide elpasolite, vacancy-ordered double perovskite, pnictogen-based metal halide, Ag-Bi-I, and metal chalcohalide families of materials. The defect-driven optical and charge-carrier transport properties of PIMs and their device performance within and beyond photovoltaics are especially discussed. Finally, a view on potential solutions for advancing the research on wide-bandgap PIMs is provided. The key insights of this review will help to tackle the commercialization challenges of these emerging semiconductors with low toxicity and intrinsic air stability.

1. Introduction

Lead halide perovskites (LHPs), with a general formula "ABX_3" (where A = monovalent cations such as Cs^+ or methylammonium, MA^+; B = Pb^{2+}; X = Cl^-, Br^-, I^-), have emerged as the premier emerging photovoltaic technology, as they enable high-performance devices combined with cost-effective low-temperature solution processability. Notably, the certified record power conversion efficiency (PCE) of LHP-based solar cells has now exceeded 26%, and is approaching the PCE of the most efficient crystalline silicon solar cell (26.8%).[1,2] Such a remarkable performance stems from the long charge-carrier diffusion lengths, high photoluminescence quantum yields (PLQYs), low exciton binding energies, sharp absorption onsets, and high absorption coefficients. The ability to achieve high PLQYs and long diffusion lengths from low-temperature solution-processed films is remarkable, and

G. K. Grandhi, B. Al-Anesi, P. Vivo
Hybrid Solar Cells
Faculty of Engineering and Natural Sciences
Tampere University
P.O. Box 541, Tampere FI-33014, Finland
E-mail: paola.vivo@tuni.fi

D. Hardy, F. Gao
Department of Physics
Chemistry and Biology (IFM)
Linköping University
Linköping SE-58183, Sweden

M. Krishnaiah
Department of Electronic Engineering
Incheon National University
Incheon 406-772, Republic of Korea

B. Vargas, D. Solis-Ibarra
Laboratorio de Fisicoquímica y Reactividad de Superficies (LaFReS)
Instituto de Investigaciones en Materiales
Universidad Nacional Autónoma de México
Circuito Exterior s/n, CU, Ciudad de Maáxico, Coyoacán 04510, Mexico

M. P. Suryawanshi
School of Photovoltaic and Renewable Energy Engineering
University of New South Wales
Sydney, New South Wales 2052, Australia

R. L. Z. Hoye
Inorganic Chemistry Laboratory
Department of Chemistry
University of Oxford
South Parks Road, Oxford OX1 3QR, UK

has been attributed to "defect tolerance", but there are still many questions regarding its origins and nature.

Research into LHPs has tremendously advanced over the last few years, with remarkable improvements in the environmental and operational stability of LHP-based devices.[1,3] However, the toxicity of the lead cation (Pb^{2+}) in the most efficient LHP compositions still raises concerns about their widespread commercialization, with the allowed limit of lead in electronic devices being $\leq 0.1\%$ by weight according to the European Union.[4] Photovoltaics for rooftop and utility-scale applications are exempt from these regulations, but other applications, such as light-emitting diodes or indoor photovoltaics, are not, and this may limit the use of LHP devices in consumer electronics. Furthermore, when in contact with humid air or water, LHPs decompose to water-soluble lead compounds that could possibly leach out to the environment. This may cause the accumulation of lead halide salts in the food chain more effectively than for other lead-based compositions (e.g., PbS) used in existing technologies such as lead-acid batteries.[5,6] Therefore, the high water solubility of the LHPs makes them potentially hazardous to the environment and human beings, particularly children. The possible leakage of lead into the environment during the life cycle of LHP-based devices may still be possible even with effective encapsulation.[4,7] Therefore, the design and synthesis of lead-free perovskite-inspired materials (PIMs) with substantially reduced toxicity is a heavily investigated topic, yet still requiring further attention. It should be noted that while the compounds with an ABX_3 stoichiometry and a crystal lattice made of a cubic network of corner-sharing BX_6 octahedra are termed halide perovskites,[8] both the three-dimensional (3D) halide perovskite derivatives, namely Sn(II) halide perovskites and halide elpasolites, and electronic analogs of the halide perovskites (i.e., zero- (0D), one-(1D), and two-dimensional (2D) metal halides containing various mono, tri, and tetravalent cations) have been commonly known as PIMs.[9]

A large fraction of the studies into PIMs have focused on Sn-based perovskites obtained by the homovalent substitution of Pb^{2+} (at the B-site) with Sn^{2+} to retain the three-dimensional (3D) perovskite crystal structure. The narrow bandgaps of Sn-based perovskites in the 1.2–1.4 eV range[10] are close to the optimum value (1.34 eV) for solar light absorbers.[11] However, Sn-based perovskites currently face a major shortcoming, namely the rapid oxidation of Sn^{2+} to Sn^{4+} in air. By contrast, low-toxicity and oxidatively stable cations such as Ag^+, Na^+, Bi^{3+}, Sb^{3+}, In^{3+}, Sn^{4+}, Ti^{4+}, Te^{4+}, etc. have been employed to synthesize a plethora of PIM compositions that belong to the halide elpasolites, vacancy-ordered double perovskites, pnictogen-based metal halides, and so on. However, owing to the differences in the size and valence state of these ions compared to Pb^{2+}, the resultant PIMs often do not retain the 3D perovskite structure but instead crystallize in 0D, 1D, and 2D structures. These PIMs usually also display wider bandgaps in the 1.6–2.5 eV range than their Pb^{2+} or Sn^{2+} counterparts, in turn, being of interest for a range of emerging applications, such as photocatalysis, tandem solar cells, and indoor photovoltaics. Low-toxicity PIMs comprising Group V cations Bi^{3+} and Sb^{3+} are anticipated to be promising due to their ns^2 valence electron configuration and high polarizabilities (similar to Pb^{2+}). Nevertheless, the PCE of devices employing these materials is far below that of LHP-based counterparts. In addition to the high exciton binding energies and constrained charge carrier transport arising from their low dimensionality, the high concentration of defects in the wide-bandgap PIMs remains a major obstacle to their material and device performance. The dominant non-radiative recombination in most of the wide-bandgap PIM compositions is evident from their low PLQYs and high non-radiative recombination rate, which correlates with losses in the open-circuit voltage (V_{OC}). Although some progress has been made in understanding the role of defects in these materials from both experimental and theoretical viewpoints, dedicated follow-up studies are a pressing priority for an in-depth understanding of the defect mitigation pathways and the identification of defect-tolerant PIM candidates. These future studies will benefit from the critical assessment of the existing knowledge on the defect chemistry of PIMs and the related device performance limitations.

Although a few other reviews on PIMs exist,[9,12–15] a comprehensive study focusing on the defect chemistry of wide-bandgap PIMs to explain their still modest performance in applications within and beyond photovoltaics is currently lacking. In this review, we aim to address this knowledge gap by discussing the up-to-date experimental and theoretical information on the influence of the defects on the optical and electronic properties of PIMs for key device applications, namely solar cells, indoor photovoltaics, photodetectors, and memristors. In addition to the perovskite-inspired metal halide compositions, we also discuss relevant examples from the chalcohalide and metal chalcogenide families, given the enormous interest of the community in these absorbers for future optoelectronics. These materials are still considered PIMs because of the similarity in their electronic structure at band extrema to LHPs, which may be conducive to achieving defect tolerance.

In this review, we first provide a brief overview of the structural and stability aspects and optical properties of the investigated PIMs. We then discuss the origin of defect tolerance in LHPs, examine the role of defects in various wide-bandgap PIMs, and discuss effective strategies to mitigate the deleterious role of defects in these materials. This is followed by an assessment of the application of PIMs in outdoor and indoor photovoltaics, photodetectors, and memristors, with a close look at the progress and performance bottlenecks in relation to the materials defects and trap-related recombination. Finally, we provide our insights on how to address the defect challenge and other device-limiting factors in PIMs.

2. Structure and Stability

Before diving into the intriguing optoelectronic properties of lead-free PIMs with wide-bandgap in relation to their defect chemistry and device applications, it is essential to begin with an overview of the composition, structure, and stability of the materials under consideration. While this section aims to provide a basic understanding, it is important to note that this review is by no means exhaustive. For a more in-depth analysis, we recommend referring to some excellent reviews that focus on specific families of lead-free materials, their structures, history, and more.[16–20] An important note for this section is that, in accordance with the standard perovskite notation, B will be used as a symbol for the central metal atom of these materials and should not be confused with the element boron.
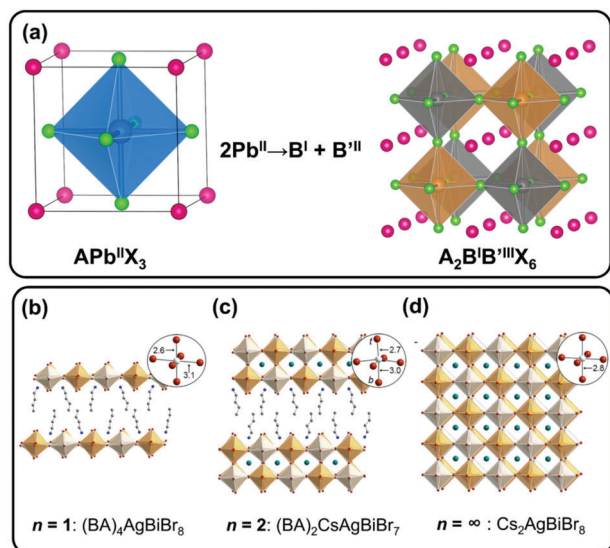
Figure 1. a) Schematic illustration of the cation-transmutation from the archetype APbX$_3$ 3D perovskite to a double perovskite (DP) or halide elpasolite.[31] The lower box represents the dimensional reduction of the Cs$_2$AgBiBr$_8$ halide elpasolite with the organic cation BA (C$_4$H$_{12}$N$^+$). 2D-halide elpasolites with b) $n = 1$, c) $n = 2$ and d) 3D-halide elpasolite. Panels (b–d) are reproduced with permission.[32] Copyright 2018, American Chemical Society.

2.1. Halide Elpasolites

Halide elpasolites, also commonly referred to as double perovskites (DPs), are a class of materials with a unique crystal structure that is based on the ABX$_3$ perovskite structure but contains two different cations at the B-site position, thus resulting in the general chemical formula of A$_2$BB'X$_6$, where A is a monovalent cation (e.g., Cs$^+$ or methylammonium, MA$^+$), B and B' are monovalent and trivalent cations respectively (e.g., Ag$^+$ and Bi^{3+}), and X is a halide (F$^-$, Cl$^-$, Br$^-$, and I$^-$). The crystal structure of halide elpasolites is cubic or pseudocubic, and each unit cell contains two interpenetrating cubic lattices, with the A cations occupying the cuboctahedral vacancies, and the B and B' cations occupying alternating octahedral sites in the other lattice (**Figure 1**a). This results in a highly ordered and symmetrical structure.[16]

Some halide elpasolites have shown good stability towards air and humid air, such as Cs$_2$AgBiCl$_6$, Cs$_2$AgBiBr$_6$, Cs$_2$AgSbCl$_6$, Cs$_2$AgInCl$_6$, Cs$_2$NaBiCl$_6$, and Cs$_2$NaInCl$_6$. For example, Cs$_2$AgBiBr$_6$, one of the most studied halide elpasolites, can be heated up to 430 °C with no visible phase transitions or decomposition processes. Despite its thermal stability, Cs$_2$AgBiBr$_6$ and other Ag-containing halide elpasolites show significant degradation under continuous light irradiation.[21] Interestingly, most of the experimentally confirmed halide elpasolites are formed with Cl as the halide. When trying to incorporate bromide anions, the more thermodynamically stable A$_3$B$^{III}_2$X$_9$ phase is predominantly formed instead (along with other phases). Even fewer halide elpasolites with iodides have been synthesized, for example, MA$_2$AgSbI$_6$,[22] Cs$_2$NaREI$_6$ (RE: Sc, Lu, Tm, and Er),[23] and Cs$_2$AgBiI$_6$.[24] The latter composition has been successfully obtained only in nanocrystal form, even though theoretical calculations predict its thermodynamic insta-

bility. This phenomenon of metastable structures becoming stable when synthesized under a colloidal approach also applies to chalcohalides, as will be seen in the next section. It is worth mentioning that some lesser-known members of this halide elpasolite family are highly hygroscopic or readily decompose in air, as in the case of luminescent Cs$_2$NaMBr$_6$ (M : Sc, Y, La)[25] and Cs$_2$LiBiCl$_6$,[26] respectively.

A 2D version of halide elpasolites can also be attained by introducing long organic cations and dications (ammonium or diammonium in nature) in between the inorganic layers (Figure 1b–d). In most ways, the dimensional reduction of halide elpasolites (with both structural and electronic dimensionality being reduced) is similar to the dimensional reduction of 3D perovskites to 2D perovskites.[27] Among other things, dimensional reduction increases its stability range and widens their bandgaps. For example, while most 3D-halide elpasolites are unstable with iodine, most 2D-halide elpasolites form with this halide. Moreover, some unstable halide elpasolites in ambient conditions (e.g., Cs$_2$AgInBr$_6$) have stable layered organic–inorganic analogs (PA$_4$AgBiBr$_8$, with PA = Propylammonium).[28,29] So far, only 2D elpasolites with one and two octahedra thick slabs have been reported ($n = 1$ and 2) with general formulas A$_4$BB'X$_8$ (A an organic monocation) and A$_2$CsBB'X$_7$, respectively, which means there could be an intrinsic instability for structures with n > 3.[30] The soft and dynamic nature of the organic cations also enables ferroelectricity in some 2D-halide elpasolites and a phase transition from an acentric state to a centrosymmetric phase is observed, usually at nearly room temperature.

2.2. Vacancy Ordered Halide Perovskites

Vacancy-ordered perovskites (VOHPs) can have either a 0D (0D-VOHP) or a 2D structure (2D-VOHP). The 0D-VOHPs can be further divided into two subgroups. The first can conceptually be derived from a halide ABX$_3$ perovskite where the divalent B metal is replaced by a tetravalent one (B^{IV}), causing the removal of half of the B cations to fulfill the charge neutrality and forming a checkerboard-type pattern of alternating BX$_6$ octahedra and vacancies (**Figure 2**). The 0D-VOHPs can also be described as antifluorites and usually have a face-centered cubic structure with a $Fm\bar{3}m$ space group and chemical formula A$_2$B^{IV}X$_6$. Alternatively, they can also be described as double halide perovskites where the B'-site is a vacancy, hence vacancy-ordered. The representative perovskite of the A$_2$B^{IV}X$_6$ group is Cs$_2$Sn^{IV}I$_6$, which is known to be more stable than CsSnI$_3$ toward air oxidation because of the more stable tetravalent Sn^{IV}. Although the decomposition rate of Cs$_2$SnI$_6$ when exposed to air is slower than CsSnI$_3$, it still decomposes into CsI after several weeks.[33] 0D-VOHPs, such as Cs$_2$PdBr$_6$, Cs$_2$TiX$_6$ (X: Cl, Br, and I), and Cs$_2$TeI$_6$, have a much higher tolerance to moisture and heat and can even withstand water at room temperature for 10 min without decomposition in the case of Cs$_2$PdBr$_6$.[34–36] This higher stability in comparison to the Pb-based perovskites is due to the higher degree of covalency between the tetravalent and the halide ions. However, this higher covalency is also responsible for the dominant defects forming deep states in the bandgap.[37] It is worth noting that several 0D-VOHPs have been successfully implemented in solar cells.[38]
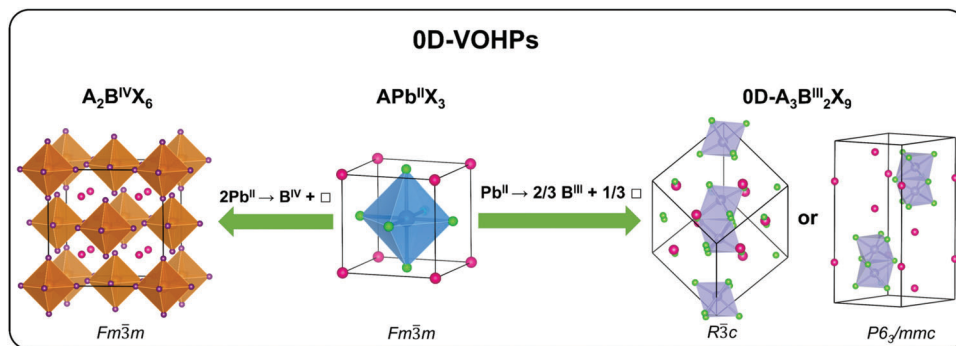
**ADVANCED
SCIENCE NEWS**

www.advancedsciencenews.com

**ADVANCED
FUNCTIONAL
MATERIALS**

www.afm-journal.de

Figure 2. Schematic illustration of the cation-transmutation from the archetype $APbX_3$ 3D perovskite to a vacancy-ordered perovskite (left) and 0D dimers $A_3B_2X_9$. When the Pb^{II} is replaced by a trivalent metal, due to the charge difference, 1/3 of the B-sites are left vacant ($B^{III}_{2/3}$) giving rise to the dimeric structure.

The next subgroup of 0D-VOHP is obtained by replacing B^{II} with a trivalent cation (B^{III}). The 0D structures with chemical formula $A_3B^{III}_2X_9$ correspond to face-sharing BX_6 octahedra occurring as $B_2X_9^{3-}$ dimers with the Cs atoms filling the hexagonal channels (Figure 2). They crystallize either in a rhombohedral (e.g., $Cs_3Tl_2Cl_9$) or a hexagonal space group (e.g., $Cs_3W_2Cl_9$). Some relevant materials in this group are $Cs_3Bi_2I_9$ and $MA_3Bi_2I_9$, which have been used as an absorber for solar cells and other applications. Further, $Cs_3Bi_2I_9$ has been shown to be very stable under ambient conditions[39] and is also stable under light illumination.[40] The stability of other 0D-VOHP with transition metals or rare earth in the B-site in this group has not been reported in the literature, but one can anticipate that it will vary depending mostly on the overall stability of the B^{III} metal and its decomposition products.

The 2D-VOHPs are the layered polymorphs of the $A_3B^{III}_2X_9$ perovskites. They are derived by replacing B^{II} in the 3D ABX_3 halide perovskite structure with a trivalent pnictogen cation (B: As, Sb, and Bi), provided the A cation is a small organic cation or an alkaline metal. The layered structure consists of slabs comprised of two layers of corner-sharing BX_9 octahedra ($n = 2$) alternating with a layer of vacancies, with the A cation occupying the voids between the octahedra (**Figure 3**) and usually crystallizing with a trigonal space group $P\bar{3}m1$. 2D-VOHPs with $n = 2$, such as $Cs_3Sb_2I_9$, degrade up to 400 °C and can withstand up to 88 days under exposure to atmospheric moisture.[41]

The slab thickness can be increased to three octahedra ($n = 3$) by incorporating a divalent transition metal (M^{II}: Mn, Fe, Cu, Cd, In) in the B^{III} sites and X = Cl, Br and I, to yield $A_4M^{II}M^{III}_2X_{12}$ perovskites (Figure 3).[18] To date, only one 2D-VOHP with fluoride as the halide has been reported, $K_4Fe^{II}Fe^{III}_2F_{12}$,[42] whereas there are several known with Cl or Br, and a few with I. 2D-VOHPs with $n = 3$ in bulk form can also withstand humid air (up to 50% relative humidity) and continuous illumination for
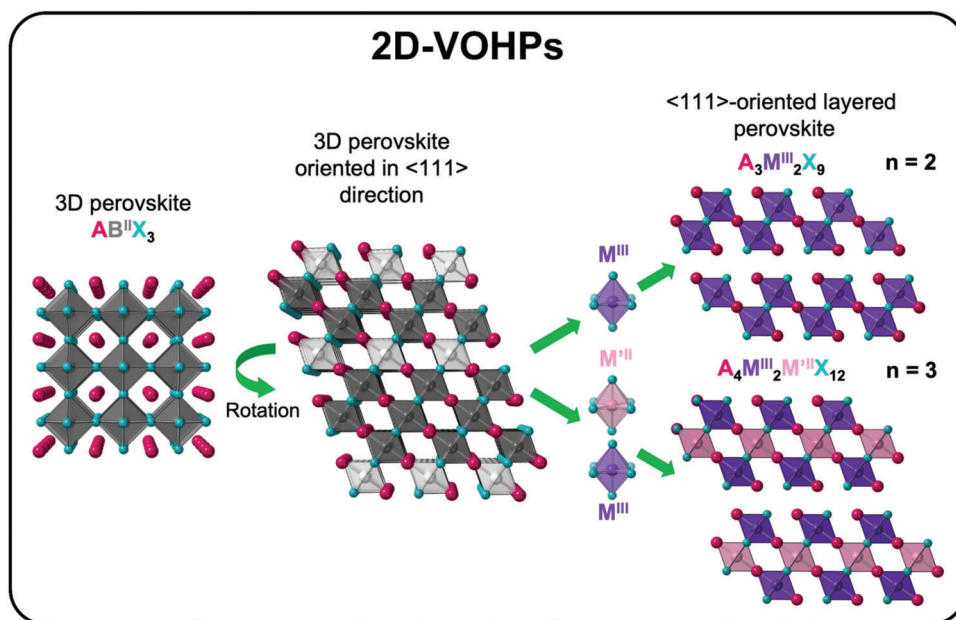

Figure 3. Schematic illustration of the cation-transmutation from the archetype $APbX_3$ 3D perovskite to a 2D-VOHP with $n = 2$ and $n = 3$. Reproduced with permission.[44] Copyright 2020, American Chemical Society.
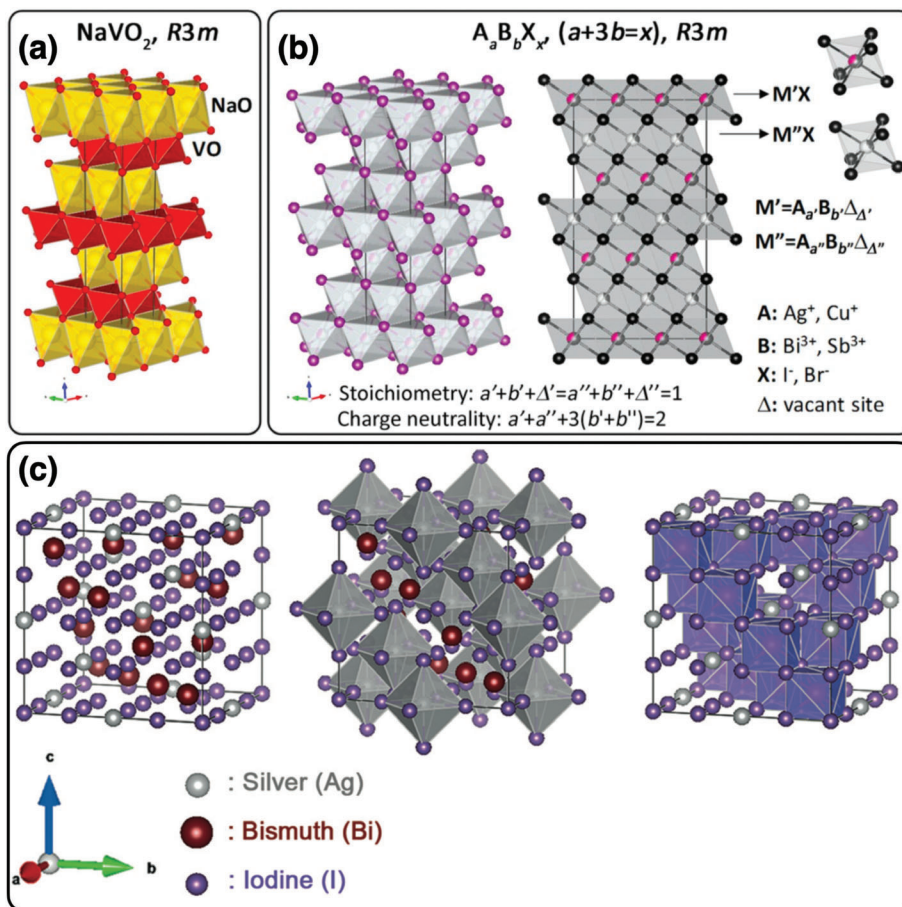
**ADVANCED
SCIENCE NEWS**

www.advancedsciencenews.com

**ADVANCED
FUNCTIONAL
MATERIALS**

www.afm-journal.de

Figure 4. Crystal structures of the a) $NaVO_2$ prototype oxide and b) $A_aB_bX_x$ halide rudorffites. Reproduced with the permission.[48] Copyright 2017, Wiley-VCH. Panel (c) shows different representations of the rudorffite $AgBi_2I_7$. Reproduced with the permission.[50] Copyright 2016, Wiley-VCH.

weeks (under simulated sun and UV light) without showing any sign of degradation. According to thermogravimetric analysis, the Sb perovskites are usually stable up to approximately 200 °C, while the Bi-based perovskites are stable up to 350 °C. In general, 2D-VOHPs present reasonable stability in highly polar solvents containing water, unlike the Pb-halide perovskites. Similarly, $Cs_4CuSb_2Sb_{12}$ has shown excellent stability under irradiation in humid conditions.[43]

2.3. Pnictogen-Based Metal Halides and Rudorffites

Pnictogen-based metal halides are a class of compounds that contain both a pnictogen (P, As, Sb, or Bi) and a halogen (F, Cl, Br, or I). They are often ternary compounds, comprised of a metal cation, a pnictogen, and a halogen, with a wide variety of stoichiometries to maintain the charge neutrality condition. While there are many known and potentially accessible pnictogen-based metal halides, for photovoltaic and optoelectronic purposes, a class of these materials gaining substantial attention are ternary Ag-Bi-I semiconductors. The general formula is $Ag_xBi_yI_{x+3y}$. The iodide sub-lattice maintains a cubic close-packed (ccp) structure, while both Ag^+ and Bi^{3+} occupy octahedral holes, with a range of octahedral motifs adopted. Ag-poor compounds (e.g., $AgBi_2I_7$)

adopt a 3D defect-spinel octahedral motif, with a cubic unit cell ($Fd\bar{3}m$ space group). $AgBiI_4$ has been found to adopt either a defect-spinel octahedral motif or a 2D $CdCl_2$-type structure ($R\bar{3}m$ space group), in which all octahedral holes in alternating layers are filled (i.e., all octahedral holes in the I ccp sub-lattice filled in layer 1, with no octahedral holes filled in layer 2). For Ag-rich compounds (e.g., Ag_2BiI_5 or Ag_3BiI_6), the extra Ag^+ cations fill the octahedral holes in layer 2 with partial occupancy, giving rise to a 3D $NaVO_2$-type structure.[45–47] Turkevych et al. proposed to call these $NaVO_2$-type Ag-Bi-I compounds "rudorffites",[48] because the structure of $NaVO_2$ was first reported by Walter Rüdorff and Hans Becker in 1954.[52] Turkevych et al. also proposed that all Ag-Bi-I stoichiometries could be explained by $NaVO_2$-type structures, with different fractions of Ag^+, Bi^{3+}, and vacancies occupying each layer of octahedral holes[48] (**Figure 4**). As a result, it has become very common in the burgeoning field to refer to all Ag-Bi-I and related compounds (including Cu-Bi-I materials) as rudorffites. We emphasize that this is not strictly speaking correct, since not all of these materials have been proven experimentally to adopt a $NaVO_2$-type structure, and we cannot therefore refer to all of these materials as rudorffites in the same way as we use the term "perovskite" by itself to strictly refer to compounds with the perovskite crystal structure. Furthermore, in Cu-Bi-I materials, Cu^+ does not occupy an octahedral hole in the same way

**ADVANCED
SCIENCE NEWS**

www.advancedsciencenews.com

**ADVANCED
FUNCTIONAL
MATERIALS**

www.afm-journal.de

as Ag^+, but rather occupies tetrahedral holes.[46] Thus, we cannot refer to Cu and Ag both being the A-site cation in a simple ABX_y general formula.

As will be discussed later in this review, pnictogen-based metal halides and rudorffites have received increasing attention in recent years due to their interesting electronic and optical properties and their subsequent applications in photovoltaics and beyond. Furthermore, initial reports have shown that several rudorffites have shown excellent thermal stability, which makes them very attractive as potential candidates for several devices.[19] However, despite early reports on thermal stability, there is very limited information about their stability under operational conditions, and the effect of heat, moisture, and illumination, or how ion migration within these materials might affect their operational stability.

Although the majority of efforts have been on Ag-Bi-I semiconductors, Cu-Bi-I materials have also been synthesized and proposed as photovoltaic materials, albeit with lower stability than their Ag analogs. To resolve this, Sansom et al. proposed to investigate the quaternary Cu-Ag-Bi-I compounds, in which Cu^+ occupies tetrahedral holes, while the larger Ag^+ and Bi^{3+} still occupy octahedral holes.[46,51] One of the materials realized is Cu_2AgBiI_6, which was found to be more stable than $CuBiI_4$.[51] This material has a $CdCl_2$-type structure where layers of edge-sharing disordered Ag^+ and Bi^{3+} octahedra alternate with a layer of vacant octahedral sites. Conceptually, Cu_2AgBiI_6 can be obtained by adding tetrahedral Cu^+ to $AgBiI_4$. In this scenario, vacancies are formed to maintain charge balance, reducing the octahedral occupancy of the Ag^+ and Bi^{3+} sites. Another promising material for photovoltaics is hexagonal $AgBiS_2$ (also known as matildite).[52] Although this material contains the chalcogenide S instead of a halide, $AgBiS_2$ can exhibit the $NaVO_2$ prototype oxide structure, where layers of edge-sharing Ag octahedra alternate with layers of Bi octahedra. Also, it has been found that because Ag^+ and Bi^{3+} have similar ionic radii, these two cations often occupy the same lattice site, giving rise to cation-disordered $AgBiS_2$ with a rocksalt structure.[53]

2.4. Metal Chalcohalides

Metal chalcohalides are a class of compounds that contain both a chalcogenide (S, Se, or Te) and a halide (Cl, Br, or I), as shown in **Figure 5**. These materials have a wide range of compositions, and the most common chemical formula is $B_wCh_yX_z$, where B is a metal, Ch is a chalcogenide, X is a halide, w and y are integers, and z is a fractional number that satisfies the charge neutrality condition. In this section, we will focus on ternary chalcohalides but quaternary and more exotic compositions that incorporate rare earth and/or alkaline metals have also been reported.[54] Chalcohalide materials have attracted significant attention in recent years due to their unique and tunable optical and electronic properties and remarkable stability. They have applications in a range of fields, including photovoltaics, light-emitting diodes, optical sensing, radiation detectors, batteries, and photocatalysis.[17]

The crystal structure of chalcohalide materials can vary depending on their composition. The most common ternary chalcohalides are the heavy pnictogen chalcohalides (B: Sb and Bi) with an orthorhombic crystal structure and a 1:1:1 stoichiome-

try ($w = y = z = 1$). These compounds form 1D chain-like structures of $BCh_3X_2 \bullet$ ($\bullet$ is a vacancy) edge-sharing pseudo-octahedra (except for AsSeI). The BiTeX chalcohalides form a layered 2D structure of $[BiTe]^+$, like the bismuth oxyhalides. The 1D or 2D structures lead to anisotropic electronic and optical properties that can be exploited for various applications, particularly, solar cells.[55] The structural characteristics of these compounds, such as the formation of chains or double chains, affect their growth and carrier transport properties and contribute to many potential applications. For instance, SbSI presents good stability and an isostructural material, $Sb_{0.67}Bi_{0.33}SI$ is a promising photovoltaic absorber with excellent device stability under exposure to light, moisture, and temperature of 85 °C.[56] The crystal structure of $Cu_2I_2Se_6$ has also been studied, revealing different coordination environments and polyhedral arrangements.[57] Furthermore, hybrid organic-inorganic metal chalcohalides, such as $MASbSI_2$ and $MA_3Bi_2I_{9-2x}S_x$, have also been reported and implemented in solar cells,[58] as discussed later.

3. Defect Chemistry of Wide-Bandgap Perovskite-Inspired Materials

As will be detailed in later sections, wide-bandgap (close to 2 eV) PIMs have many important applications in next-generation energy, communications, and computing applications. A critical factor affecting their performance is defects, which act as sites of non-radiative recombination. One of the key factors driving the exploration of PIMs is the identification of compounds that could replicate the defect tolerance of LHPs. In this section, we discuss evidence for and against defect tolerance in LHPs, whether it can be replicated in wide-bandgap PIMs, and the progress made in devising strategies to mitigate the role of defects in PIMs.

3.1. Defect Tolerance in Halide Perovskites and their Applicability to Wide-Bandgap Alternatives

3.1.1. What is Defect Tolerance?

There is a hierarchy of defects that impact on device performance, from 0D point defects, to 1D and 2D structural defects (e.g., grain boundaries and stacking faults), through to 3D macroscopic defects (e.g., voids). Macroscopic defects, and to a certain extent 1D and 2D structural defects, can be mitigated by optimizing the processing of the materials, e.g., by avoiding pinholes and increasing grain size. Discussions around defect tolerance have therefore focused on point defects, which include vacancies, antisites, and interstitials, as well as defect complexes, such as Schottky defects.[60–64] Such point defects can readily be simulated using modern computational techniques, and also evaluated experimentally, for example through deep-level transient spectroscopy (DLTS).

Defect tolerance is typically considered to refer to point defects not affecting the charge-carrier mobility or non-radiative recombination rate.[66,67] Based on the Shockley–Read–Hall model for one defect state within the bandgap of a semiconductor, a low non-radiative recombination rate can be retained despite a high defect density if the trap is shallow (i.e., within a few kT of one of
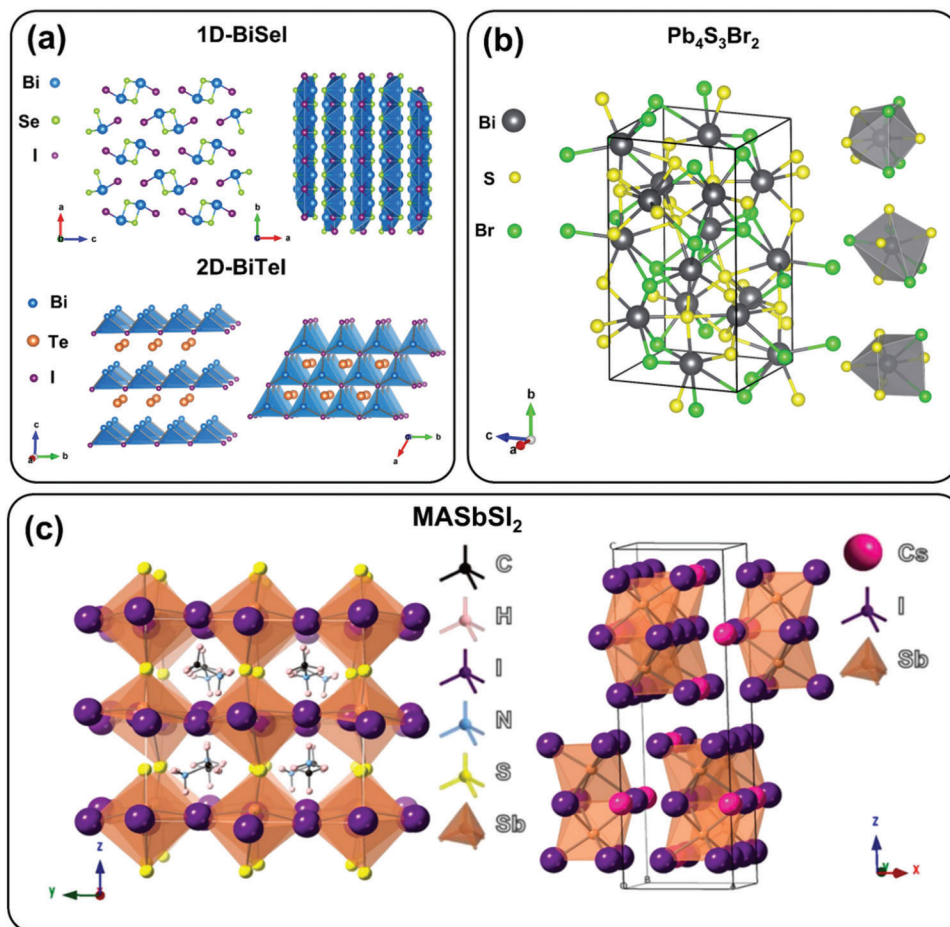
**ADVANCED
SCIENCE NEWS**

www.advancedsciencenews.com

**ADVANCED
FUNCTIONAL
MATERIALS**

www.afm-journal.de

Figure 5. Structures of a) heavy pnictogen chalcohalides with a 1: 1: 1 stoichiometry, b) Pb-based stable chalcohalide $Pb_4S_3Br_2$ [59] and the three different Pb-coordination polyhedral in the structure and, c) a hybrid organic-inorganic chalcohalide $MASbSI_2$. Reproduced with permission.[58] Copyright 2018, American Chemical Society.

the band-edges), and/or has a low capture cross-section,[66,68] as illustrated in **Figure 6**. However, we would add that this definition of defect tolerance should only refer to free charge-carriers or excitons. Bismuth-halide PIMs have been widely found to exhibit carrier localization, in which the wavefunction of the charge-carrier or exciton is constrained to within a unit cell owing to coupling with optical or acoustic phonons.[69–71] In this case, an increase in defect density does not affect the charge-carrier lifetime or mobility because these parameters are limited by the small polarons or self-trapped excitons.[72] But because the mobility is severely reduced, diffusion lengths are short,[70,72] whereas the implication of defect tolerance is that long diffusion lengths can be achieved to enable high charge-collection efficiency in diffusion-driven devices, such as photovoltaics.

3.1.2. Evidence for and Against Defect Tolerance in Lead-Halide Perovskites

Although defect tolerance is widely quoted as a principal reason behind the exceptional performance of lead-halide perovskites in photovoltaics, the evidence for this occurring in these materials

remains under debate. Defect tolerance was first proposed for solar absorbers over 20 years ago by Zunger and co-workers to explain the ability of $CuInSe_2$ to tolerate high concentrations (on the order of 1%) of native defects, which was based on copper vacancies and In_{Cu} anti-sites forming a benign defect pair.[61] In 2014 and 2015, defect tolerance resurfaced to explain computational work indicating $MAPbI_3$ to primarily form shallow transition levels for its lowest formation energy point defects[62,66] (Figure 6). The proposed explanation was that this was due to the unusual electronic structure (shown in Figure 6, right) that resulted in disperse band extrema, and therefore increased the likelihood of defect transition levels being shallow, especially cation vacancies. This effect was enhanced by spin-orbit coupling (SOC; which is high due to the presence of heavy Pb) that lowers the bandgap and further increases the chances of transition levels being close to a band-edge.[66] The advantage of this model is that it implies that defect tolerance is not unique to LHPs and may be found in other semiconductors, even in classes of materials that are not perovskites (e.g., BiOI, BiSI), provided that they can form qualitatively similar electronic structures at the band extrema. This has particularly placed emphasis on compounds containing cations that are heavy (high spin-orbit coupling) and have stable valence
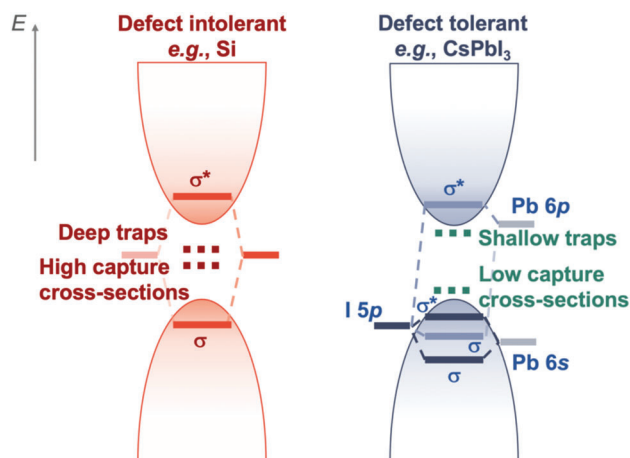
2307441 (7 of 52)

**ADVANCED
SCIENCE NEWS**

www.advancedsciencenews.com

**ADVANCED
FUNCTIONAL
MATERIALS**

www.afm-journal.de

Figure 6. Illustration of how defect tolerance can arise in LHPs, based on a simplified molecular orbital diagram of the band extrema. Defect intolerant materials (left) form deep traps that are close to mid-gap and have an approximately equal probability of capturing both electrons and holes. Along with high capture cross-sections, these deep recombination centers give rise to high rates of non-radiative recombination, and their density needs to be minimized as much as possible. Defect tolerant materials (right), on the other hand, primarily have shallow traps with low capture cross-sections, such that low rates of non-radiative recombination are maintained despite high defect densities. It is proposed that shallow traps are favored based on the unusual electronic structure formed by LHPs at the band-extrema (illustrated right), and low capture cross-sections achieved through high dielectric constants and low effective masses. Reproduced under the terms of the CC-BY license.[65] Copyright 2021, The Authors, published by Wiley-VCH.

s^2 electrons that can hybridize with anion orbitals to give a similar electronic structure as LHPs at the upper valence band and conduction band minimum (shown in Figure 6, right), especially compounds with Bi^{3+}, Sb^{3+}, Sn^{2+}, and In^+, which are termed "ns^2" compounds.[66] The advantage of these heavy metal cations is that they have high polarizability, which can lead to large dielectric constants that Coulombically screen charged defects and reduce the capture cross-sections of defects.[66,73,74]

However, it is clear that the electronic structure model (i.e., as illustrated in Figure 6, right) does not fully describe how defect tolerance arises, and there is still debate over whether the dominant point defects in LHPs do indeed have shallow transition levels.[67,75] Zhang, Van de Walle, and co-workers pointed out that the early defect calculations on $MAPbI_3$ were performed with a low level of theory using the Perdew-Burke-Ernzerhof (PBE) functional. This underestimates the bandgap, but does not account for spin-orbit coupling (which would lower the bandgap). As a result, these two errors cancelled out, and the calculated bandgap (1.5 eV) was close to the experimental value (1.58 eV).[62] However, in going to a higher level of theory, it was found that defects that appeared to be shallow using the PBE functional were in fact deep (e.g., I interstitials),[64,75] as shown in **Figure 7**a–c. Furthermore, Van de Walle and co-workers found that the high anharmonicity in LHPs, along with their strong electron-phonon coupling, results in a breakdown in the conventional wisdom that the capture coefficients of defects can be gauged simply by the relative position of the transition level to the band-edges[75]

(Figure 7d,e). To further complicate the picture, Kronik and co-workers found that the significant local dynamic disorder of $CsPbBr_3$ resulted in its Br vacancy transition level fluctuating by 1 eV on a picosecond timescale, whereas the fluctuation in GaAs is only 0.1 eV (**Figure 8**).[76] In such a dynamic local environment, It becomes difficult to classify defects as being shallow or deep, although Kronik and co-workers proposed that the frequent visits of deep defects to shallow regions allow trapped carriers to be released, and this would be consistent with defect tolerance.[76] In addition, De Angelis and co-workers found that although I interstitials form a deep trap, these are amphoteric, and hole traps (I_i^-) can readily be converted to electron traps (I_i^+) under mildly oxidizing conditions and become kinetically de-activated, making them benign.[64]

Experimentally, the density of defect states in LHPs has been found to range from 10^{10}–10^{12} cm^{-3} in single crystals to 10^{13}–10^{16} cm^{-3} in polycrystalline thin films, with occasional reports of up to 10^{17} cm^{-3}.[67,64] These values substantially exceed the defect densities found in single-crystal silicon (10^8 cm^{-3}), and yet the best polycrystalline perovskite solar cells have power conversion efficiencies approaching the record value for single-crystal silicon photovoltaics (26.1% and 26.8%, respectively).[2] For example, the recent α-$FAPbI_3$ perovskite solar cell reported by Seok and co-workers with a certified 25.7% PCE had a reported trap density of 9.37×10^{15} cm^{-3},[1] Careful passivation of interfaces and grain boundaries are required to achieve the highest PCEs in LHP photovoltaics, but the high PCEs achieved despite high trap densities would suggest that these defects in LHPs are not as harmful as in conventional semiconductors. Alivasatos and co-workers provided further experimental evidence consistent with defect tolerance in LHPs.[77] They intentionally introduced halide vacancies into $CsPbI_3$ nanocrystals by washing the nanocrystals in a low polarity solvent (toluene), in which the oleylammonium ligand is removed with a halide counterion. In doing so, they found that the PLQY remained close to unity for $CsPbI_3$ as the number of halide vacancies per nanocrystal increased from <25 to 350 (**Figure 9**a).[77] Further evidence consistent with defect tolerance was provided by Steirer et al., who showed that the Fermi level to valence band offset remained constant until the I/Pb ratio decreased below 2.5 through the removal of MAI (Figure 9c).[78] On the other hand, DLTS measurements have shown that deep traps can occur in $MAPbI_3$ (0.76 eV from the band-edge) with high density ($\approx 10^{15}$ cm^{-3}), but the capture cross-section was low (10^{-14} cm^2), and 18%-efficient solar cells could still be achieved. The low capture cross-section is consistent with expectations that the high dielectric constant in LHPs result in Coulombic screening of charged defects.[66,79]

Beyond defect tolerance, an alternative explanation put forward for the high performance of LHPs is self-healing, which refers to the autonomous repair of damage to LHPs without external factors.[67] Self-healing has been widely invoked to explain the high radiation hardness of LHPs, and the ability of photovoltaic devices to recover in performance in the dark (Figure 9d,e). It is expected that self-healing occurs as a result of halide ion migration (which is known to be prevalent in LHPs). But despite mounting experimental evidence for self-healing, simulating these effects is challenging.[67]
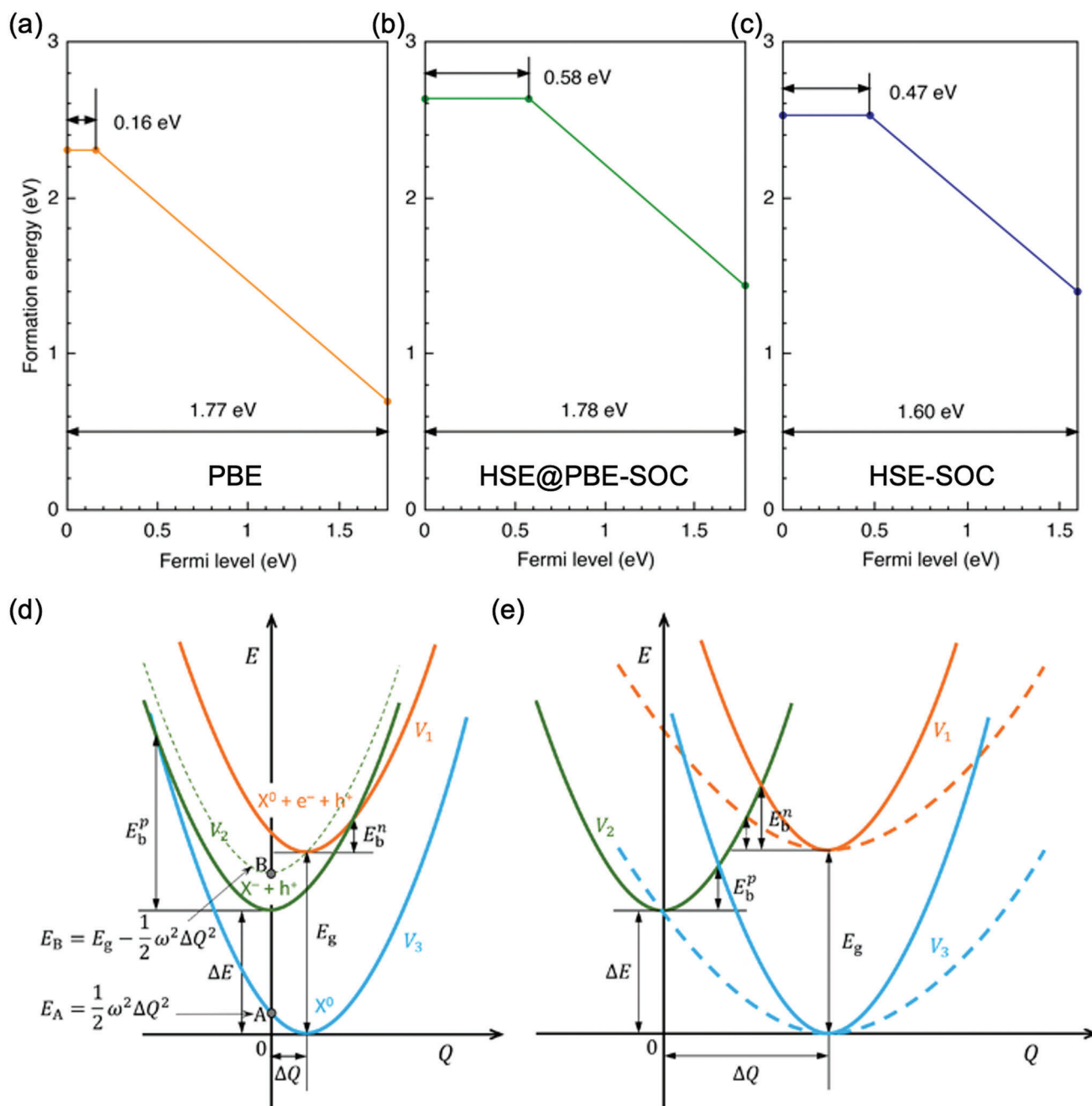
**ADVANCED
SCIENCE NEWS**

www.advancedsciencenews.com

**ADVANCED
FUNCTIONAL
MATERIALS**

www.afm-journal.de

Figure 7. Challenges of simulating the effects of defects in MAPbI$_3$. Defect formation energy of the hydrogen vacancy from the ammonium group in MA (V$_H$[N]) as a function of Fermi level calculated using a) the PBE functional, b) HSE-SOC calculations from defect configurations relaxed using PBE (HSE@PBE-SOC), and c) with both defect configuration relaxations and energies calculated using HSE-SOC. d) Typical configuration coordinate diagram for defect X transitioning from a neutral state (X^0, blue curve) to a negative charge state through electron capture (X$^-$, green curve), followed by transitioning back to a neutral state through hole capture (X^0, orange curve). e) Illustration of how increasing the average distortion associated with the neutral defect (ΔQ) affects the capture barriers (E_b). Reproduced with permission.[75] Copyright 2022, American Institute of Physics.

3.1.3. Defect Tolerance in Wide-Bandgap Perovskite-Inspired Materials

There has been a handful of computational and experimental evidence supporting defect tolerance in lead-free PIMs. Computational investigations into the vacancy and anti-site defects in BiOI (E_g of 1.93 eV) show that the most common of these defects have transition levels either resonant in the bands, or shallow within the bandgap[82] (**Figure 10**a). These defect calculations also showed BiOI to be a self-compensating system, with the Fermi level pinned close to mid-gap by the cross-over point between the lowest formation energy donor and acceptor
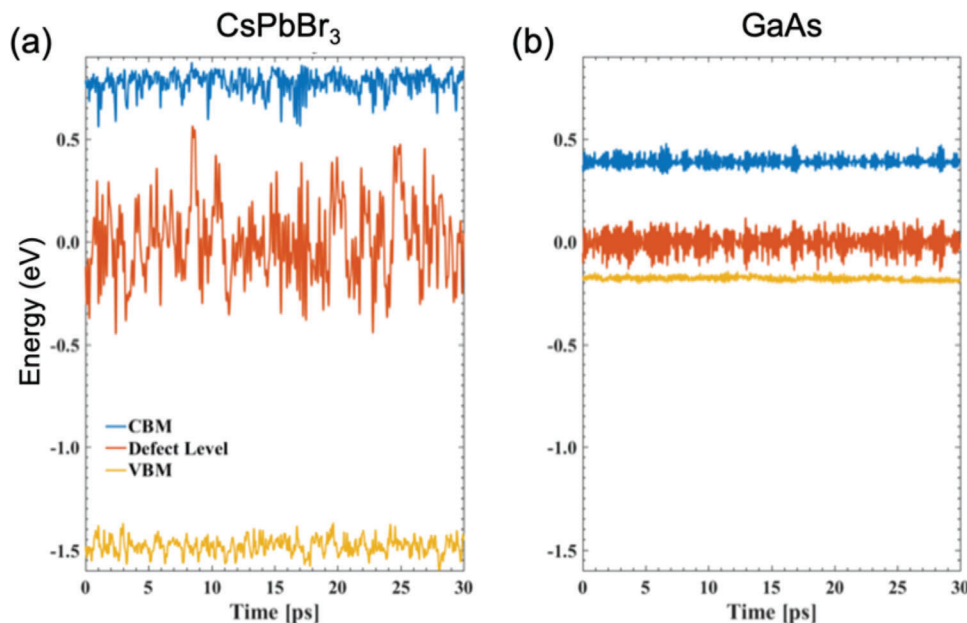
ADVANCED
SCIENCE NEWS
www.advancedsciencenews.com

ADVANCED
FUNCTIONAL
MATERIALS
www.afm-journal.de

Figure 8. Illustration of how local dynamic disorder influences the calculated eigenvalues for the valence band maximum (VBM), defect level, and conduction band minimum (CBM) for a) $CsPbBr_3$ (V_{Br}) and b) GaAs (As_{Ga}), which represent different extremes in the local dynamic disorder. Reproduced with permission.[76] Copyright 2019, American Chemical Society.
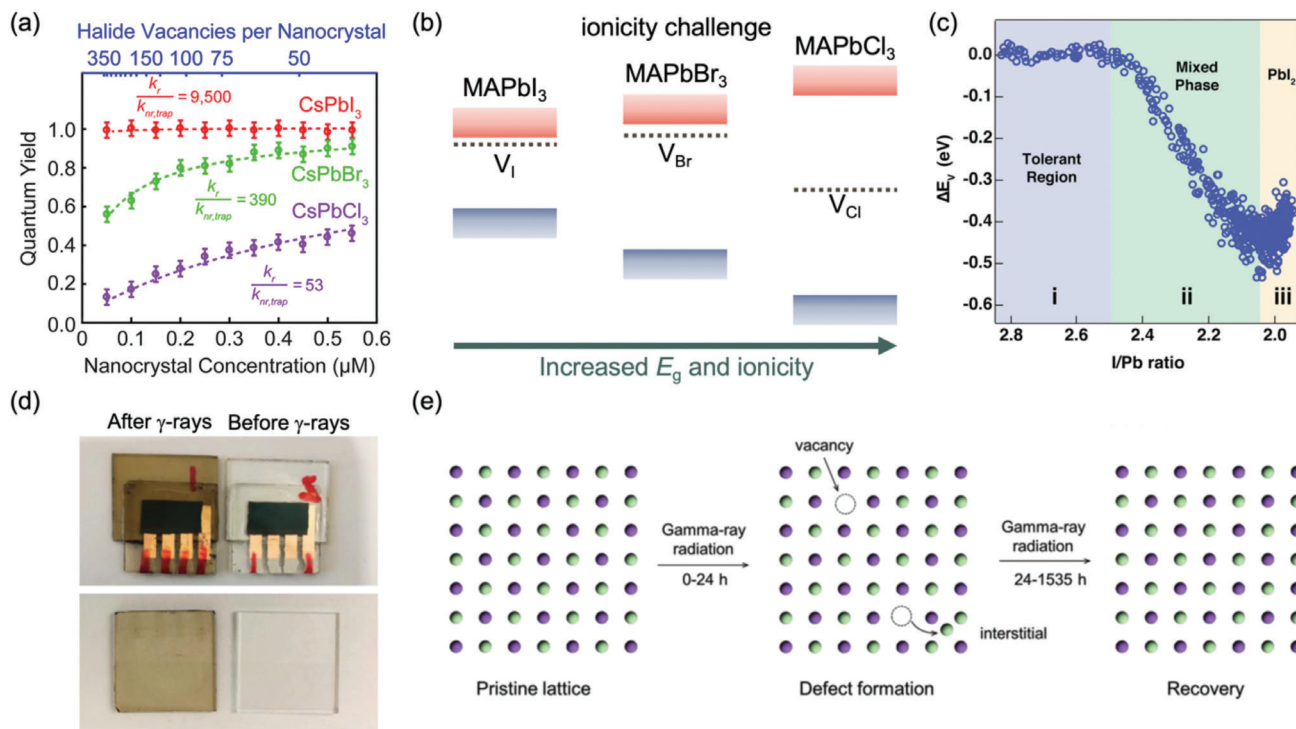

Figure 9. Experimental evidence for defect tolerance and self-healing in lead-halide perovskites. a) Variation in the PLQY for $CsPbI_3$, $CsPbBr_3$, and $CsPbCl_3$ as a function of halide vacancy per nanocrystal, with halide vacancies intentionally introduced through removal of labile ligands in non-polar solvents. Reproduced with permission.[77] Copyright 2018, American Chemical Society. b) Illustration of how the transition level of halide vacancies change with bandgap and the ionicity of the Pb-X bond. Reproduced under the terms of the CC-BY license.[80] Copyright 2022, The Authors, published by Springer Nature. $CsPbX_3$ compounds behave in a similar way.[77]5 c) Fermi level to valence band offset (ΔE_V) of $MAPbI_3$ as a function of reducing I/Pb ratios as MAI is progressively removed. Reproduced with permission.[78] Copyright 2016, American Chemical Society. d) Photographs of triple-cation perovskites (top) on indium tin oxide (ITO)-coated glass substrates (bottom) before and after exposure to 2.3 Mrad γ-ray after 1535 h. e) Proposed mechanism for self-healing in perovskites after damage from γ-ray exposure. Reproduced with permission.[81] Copyright 2018, Wiley-VCH.

ADVANCED
SCIENCE NEWS
www.advancedsciencenews.com

ADVANCED
FUNCTIONAL
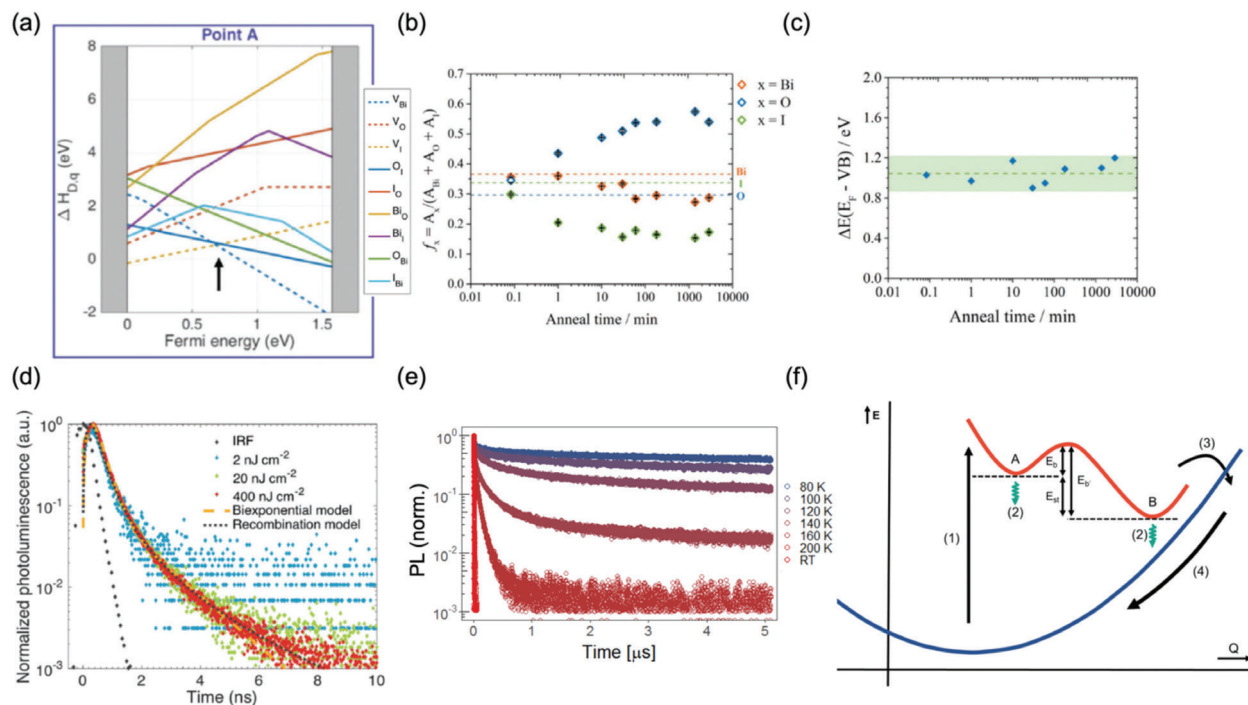**MATERIALS**
www.afm-journal.de

Figure 10. Defect properties and multi-phonon emission processes in BiOI. a) Defect diagram for BiOI under I-rich, Bi-poor growth conditions for vacancy and anti-site defects. b) Fraction of Bi, I or O in the surface of BiOI (measured by X-ray photoemission spectroscopy) after vacuum annealing at 100 °C for varying times, and c) the resulting Fermi level to valence band offset (ΔE_V). d) Time-resolved photoluminescence (TRPL) of BiOI thin films under different fluences at room temperature. The lifetime obtained by fitting a drift-diffusion recombination model was 2.7 ns. e) TRPL of BiOI single crystals from room temperature (RT) down to 80 K. f) Proposed configuration coordinate diagram to describe changes in the ground state (blue) and excited state (red) after photo-excitation and coupling to the two dominant A_{1g} longitudinal optical phonon modes induced through displacive excitation of coherent phonons. Steps are: 1) photoexcitation, 2) relaxation to local minima in the excited state potential energy surface and coupling to the ground state to give photoluminescence, 3) non-radiative coupling of charge-carriers to the ground state, and 4) non-radiative relaxation of the lattice to equilibrium. Reproduced under the terms of the CC-BY license.[82–84] Copyright 2017, The Authors, published by Wiley-VCH (a,d), Copyright 2020, The Authors, published by Wiley-VCH (b,c), and Copyright 2023, The Authors, published by Springer Nature (e,f).

defects.[82] This was confirmed through experiment, in which X-ray photoemission spectroscopy (XPS) measurements showed the Fermi level to be close to mid-gap,[82] and this was unchanged after percent-level changes to the stoichiometry of the surface of BiOI[83] (Figure 10b,c). The charge-carrier lifetime was also unchanged after these percent-level changes in the surface stoichiometry, but the maximum lifetime measured from BiOI thin films was only 2.7 ns (Figure 10d).[82] Recently, Jagt, Bravić et al. showed that electron-phonon coupling results in the formation of a non-radiative recombination channel in BiOI that is not related to defects, and still limits the room-temperature PL lifetime to only ≈2 ns, even in single crystals with < 10^{10} cm^{-3} defect density[84] (Figure 10e,f).

Going beyond ns^2 compounds, there is mixed computational evidence for defect tolerance in the vacancy-ordered double perovskite Cs_2SnI_6. Defect calculations by Maughan et al. suggested the iodine vacancy to be shallow (**Figure 11**a),[85] whereas calculations by Xiao et al. suggested the opposite, and that these defects have deep transition levels under both I-rich and I-poor conditions.[38] Under I-poor conditions, Xiao et al. also found that Sn_i also has deep transition levels.[38] Upon changing Sn^{4+} to Te^{4+}, the iodine vacancy transition level stays at the same energy relative to the valence band maximum, but the bandgap increases (from 1.36 eV for Cs_2SnI_6[86] to 1.5 eV for Cs_2TeI_6[87]), thus mak-

ing this a deep trap (Figure 11a).[85] Despite the expected defect intolerance of Cs_2TeI_6, charge-carrier lifetimes as long as 2.6 ns have been extracted from TRPL measurements.[87]

Finally, computational studies have also hinted at the interesting defect chemistry of $BaZrS_3$ (E_g ≈1.7 eV).[89] When Zr vacancies form, or when S-based point defects arise, the dangling S bonds are expected to form trimers and tetramers, thus cleaning up deep traps, and form benign defect states. For example, the Zr vacancy in $BaZrS_3$ was predicted to have a (0/+) transition level that is closer to the valence band than conduction band (Figure 11b), and the capture coefficient for electrons would therefore be low. This implies another route towards achieving defect tolerance, and is consistent with the room-temperature PL observed in $BaZrS_3$.[90] However, further work is needed to verify this proposed defect mitigation mechanism.

Overall, achieving defect tolerance, and even measurable room-temperature PL, is challenging in wide-bandgap PIMs. This is partly because a lower electron affinity (EA), or high ionization potential (IP) increases the likelihood of traps becoming deep, as evidenced in the earlier discussion on Cs_2SnI_6 and Cs_2TeI_6 (Figure 11a). Another example is the case of $CsPbX_3$, in which it was shown that the defect tolerance of $CsPbI_3$ is not preserved as the halide is changed for Br and Cl, and the bandgap increased. Alivasatos and co-workers found that while the PLQY of
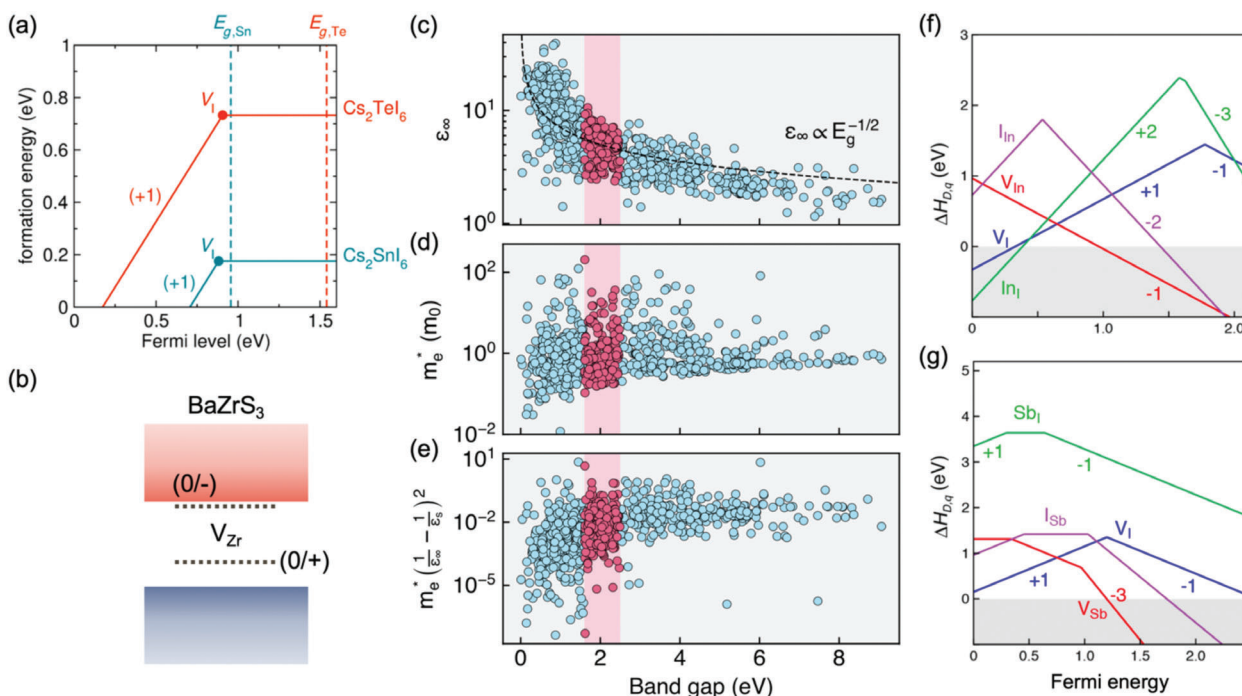
**ADVANCED
SCIENCE NEWS**

www.advancedsciencenews.com

**ADVANCED
FUNCTIONAL
MATERIALS**

www.afm-journal.de

Figure 11. a) Defect formation energy of V_I in Cs_2SnI_6 and Cs_2TeI_6. Reproduced under the terms of the CC-BY license.[85] Copyright 2016, The Authors, published by the American Chemical Society. b) Illustration of the (0/+) and (0/-) transition levels for V_{Zr} for $BaZrS_3$. Variation in the c) optical dielectric constant (ε_∞), d) electron effective mass (m_e^*), and e) polaron binding energy with bandgap. Parts (a) to (e) reproduced under the terms of the CC-BY license from Ref. [80] Copyright 2022, The Authors, published by Springer Nature. Defect diagrams for f) InI and g) SbI_3. Reproduced with permission.[88] Copyright 2018, American Chemical Society.

$CsPbI_3$ remained close to unity with the intentional introduction of halide vacancies, $CsPbBr_3$ had a lower PLQY that decreased slightly, while $CsPbCl_3$ had a strong dependence on halide vacancy concentration (Figure 9a).[77] In addition to a lower EA and higher IP, changing from iodide to chloride results in a reduction in the lattice parameter, and thus Pb dangling bonds hybridize more strongly when halide vacancies form, increasing the likelihood of deep traps forming[91] (Figure 9b; this illustration also applies to $CsPbX_3$). Unlike these wide-bandgap semiconductors, BiOI has a shallow iodide vacancy that is resonant within the conduction band because of the relatively large EA of 4.1 eV, as well as comparatively long Bi–I bonds, which would lead to a smaller overlap between Bi dangling bonds when I vacancies form (Figure 10a).[80,82]

Another challenge with wide-bandgap materials is that there tends to be a decrease in the polarizability, in which the optical dielectric constant varies inversely with the square root of the bandgap, which can lead to larger electrostatic interactions between charge-carriers and charged defect states (Figure 11c). In screening through compounds on the Materials Project database, it was also found that the effective mass overall tends to increase with bandgap (Figure 11d). This not only leads to lower mobilities, but also a higher capture cross-section, due to an increase in the factor by which the capture cross-section increases when a defect is charged rather than neutral (i.e., the Sommerfeld enhancement factor).

Beyond these challenges, computational studies have shown that unlike Pb, the 6s orbital plays a less prominent role in Bi-based PIMs, and the valence band density of states is often

dominated by other species, especially in ternary compounds. Thus, despite predictions hinting at the potential of Bi-based materials,[73] many of these compounds do not have an electronic structure at the band extrema that are qualitatively the same as that found in LHPs. Furthermore, how deep or shallow cation vacancies depend on the bonding-antibonding splitting in the molecular orbitals formed between the ns^2 cation and halide anion. A greater misalignment in the cation/anion orbital energy levels results in smaller bonding/antibonding orbital splitting, and therefore a greater likelihood of deep traps forming. For example, defect calculations suggest that while InI is tolerant to In vacancies (Figure 11f), SbI_3 (Figure 11g) and BiI_3 are not tolerant to ns^2 cation vacancies.[88] It is therefore important to develop deeper insights into how defect tolerance arises and identify a wider range of descriptors for defect tolerance, as well as gain deeper insight into the defect chemistry of wide-bandgap PIMs.

3.2. Defects in Wide-Bandgap Perovskite-Inspired Materials

3.2.1. Halide Elpasolites

$Cs_2AgBiBr_6$ is by far the most studied halide elpasolite. Unfortunately, this attention is not matched by the promise of the bulk properties of the material, and photovoltaic efficiencies are mostly <3%.[92] Defect calculations have shown that a wide range of deep traps exist in this material, including Ag_{Bi}, V_{Bi}, and Br_i, although V_{Ag} and V_{Br} have shallow transition levels[93] (**Figure 12a**). These calculations were made using PBE functionals without

**ADVANCED
SCIENCE NEWS**

www.advancedsciencenews.com

**ADVANCED
FUNCTIONAL
MATERIALS**

www.afm-journal.de

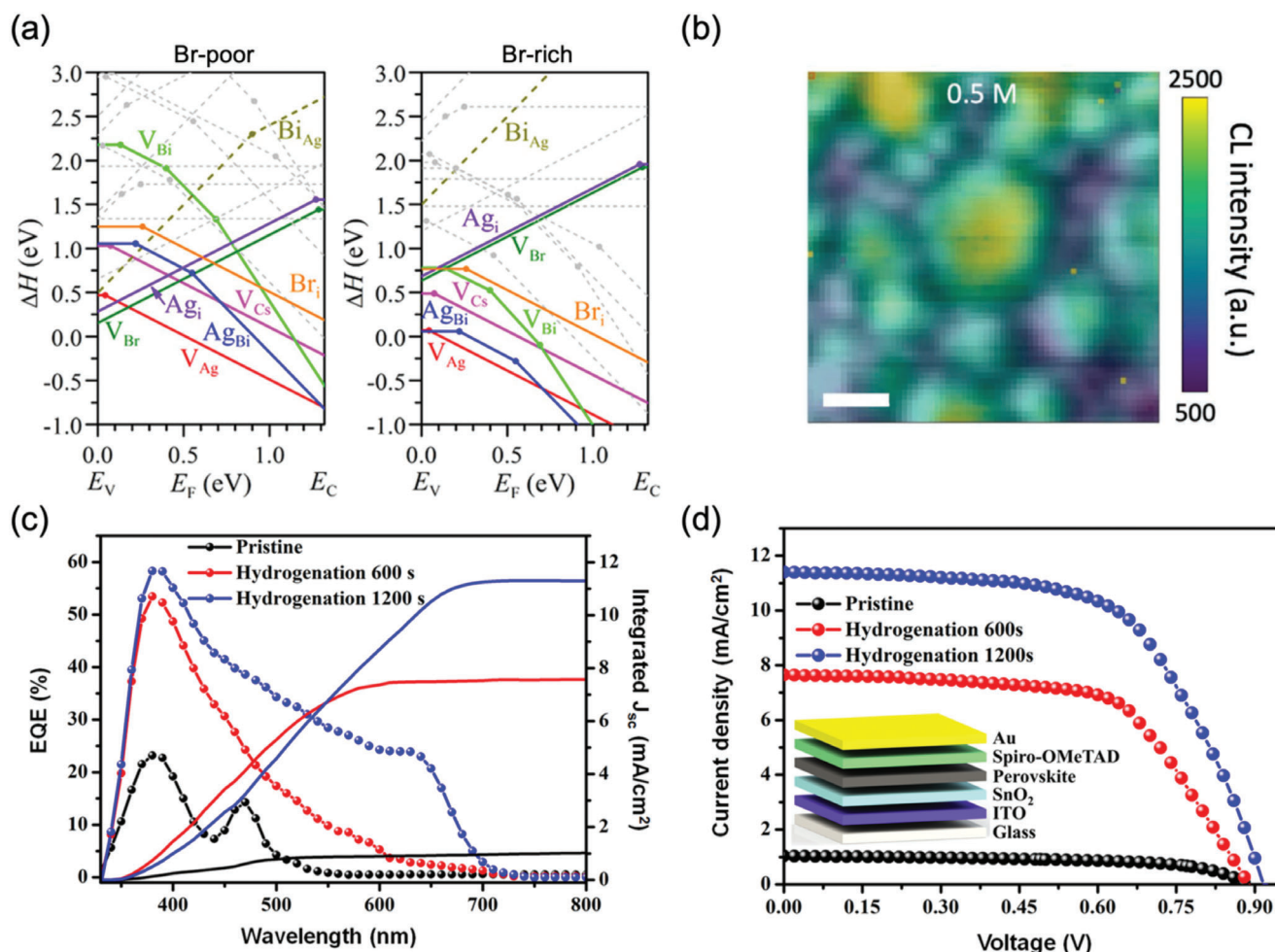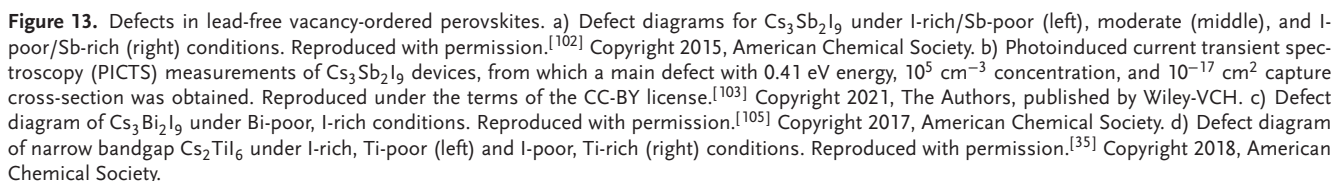**Figure 12.** Defects in $Cs_2AgBiBr_6$ halide elpasolite. a) Defect diagram of this complex material under Br-poor (left) and Br-rich (right) conditions. Reproduced with permission.[93] Copyright 2016, Wiley-VCH. b) Cathodoluminescence map (colored) superimposed over a secondary electron image (black and white), obtained using a scanning electron microscope. Scale bar 200 nm. Reproduced under the terms of the CC-BY license.[95] Copyright 2021, The Authors, published by Wiley-VCH. c) External quantum efficiency (EQE) curve and integrated short-circuit current density (J_{SC}), and d) current density versus voltage curves for photovoltaics made from $Cs_2AgBiBr_6$ treated under a hydrogen plasma from 0 s to 1200 s. Reproduced the terms of the CC-BY license.[96] Copyright 2022, The Authors, published by Springer Nature.

SOC, but when the transition levels for the dominant V_{Ag} and Ag_{Bi} defects were recalculated using hybrid functionals with SOC incorporated, the energy levels were almost the same. These calculations predict $Cs_2AgBiBr_6$ to have p-type conductivity,[93] and this was verified using X-ray photoemission spectroscopy measurements of the Fermi level to valence band offset,[94] as well as field-effect transistor measurements.[95]

Despite predictions that $Cs_2AgBiBr_6$ has a wide range of deep recombination centers that would limit performance, original reports of single crystals of this material found that the PL decay had a long tail with a time constant exceeding 660 ns, albeit this tail was reached after an order of magnitude decrease in PL intensity within the first couple of nanoseconds.[97] Transient absorption spectroscopy measurements indicate charge-carriers persist for over a microsecond after photoexcitation.[94] But again, short-time transient absorption spectroscopy measurements showed the original ground state bleach to decrease by a half within 2 ps after photo-excitation.[94] These observations prompt ques-

tions on the nature of excitations in $Cs_2AgBiBr_6$, and how such slow non-radiative decays could be achieved in the presence of a high density of non-radiative recombination centers. An increasing body of recent work suggests that these observations are due to carrier localization in $Cs_2AgBiBr_6$, which arises due to strong coupling between charge-carriers and acoustic phonons due to the high deformation potential and low electronic dimensionality in this material.[71,98] As a result, while excitations are long-lived, mobilities are substantially restrained, limiting diffusion lengths.[71,98] Indeed, analyses of polycrystalline thin film $Cs_2AgBiBr_6$ photovoltaics found that photovoltaic efficiencies were limited due to low electron diffusion lengths of only 30 nm, with mobilities <1 cm^2 V^{-1} s^{-1}.[99] It was believed in addition to self-trapping, trapping at surfaces and interfaces also played a role.[99] Cathodoluminescence mapping measurements of $Cs_2AgBiBr_6$ thin films have also shown grain boundaries to be sites of non-radiative recombination (Figure 12b), and that decreasing their density increased the lifetime found from transient

Figure 13. Defects in lead-free vacancy-ordered perovskites. a) Defect diagrams for $Cs_3Sb_2I_9$ under I-rich/Sb-poor (left), moderate (middle), and I-poor/Sb-rich (right) conditions. Reproduced with permission.[102] Copyright 2015, American Chemical Society. b) Photoinduced current transient spectroscopy (PICTS) measurements of $Cs_3Sb_2I_9$ devices, from which a main defect with 0.41 eV energy, 10^5 cm^{-3} concentration, and 10^{-17} cm^2 capture cross-section was obtained. Reproduced under the terms of the CC-BY license.[103] Copyright 2021, The Authors, published by Wiley-VCH. c) Defect diagram of $Cs_3Bi_2I_9$ under Bi-poor, I-rich conditions. Reproduced with permission.[105] Copyright 2017, American Chemical Society. d) Defect diagram of narrow bandgap Cs_2TiI_6 under I-rich, Ti-poor (left) and I-poor, Ti-rich (right) conditions. Reproduced with permission.[35] Copyright 2018, American Chemical Society.

absorption spectroscopy measurements.[95] Thus, in addition to intrinsic limitations in $Cs_2AgBiBr_6$ due to carrier localization, defects also play a role on charge-carrier transport, and it is important to mitigate their effects to improve performance.

Conversely, judiciously increasing the defect density in $Cs_2AgBiBr_6$ can lead to an improvement in PCE to 6.37%.[96] Zhang et al. found that doping $Cs_2AgBiBr_6$ with H (by treating spin-coated films with a H_2 plasma) lowered the IP and increased the absorption further in the red wavelength range, thus increasing long wavelength EQEs (Figure 12c), with J_{SC}s improving from ≈1 mA cm^{-2} (no H_2 plasma treatment) to 11.4 mA cm^{-2} (optimal H doping, estimated at 0.3 at.%), as shown in Figure 12d.[96,100]

3.2.2. Vacancy-Ordered Perovskites

A wide variety of vacancy-ordered double and triple perovskites have been investigated.[101] Among all materials considered, some of the more interesting are $Cs_3Sb_2I_9$, $Rb_3Sb_2I_9$, and $Cs_3Bi_2I_9$ vacancy-ordered triple perovskites, and Cs_2TiBr_6 vacancy-ordered double perovskites because these are the wide-bandgap PIMs that have achieved some of the most efficient photovoltaics in this family of materials.[101]

Defect calculations on $Cs_3Sb_2I_9$ showed that V_I, V_{Cs}, and I_i form deep transition levels, located ≈0.2 eV from the closest band-edges. Depending on the chemical potential, the formation energies can fall below 1 eV, and would be considered to be present in sufficient concentrations at room temperature to be significant (**Figure 13**a). These transition levels also only involve the charge state changing by unity, suggesting that capture cross-sections could also be significant.[102] Measurements of the defect states in $Cs_3Sb_2I_9$ by photoinduced current transient spectroscopy (PICTS) showed a state centered at 0.41 eV, albeit with a low-fitted capture cross-section of 5×10^{-17} cm^2 (Figure 13b).[103] Possibly the signatures of multiple defect states were obscured together. Indeed, cathodoluminescence measurements showed at least three sub-bandgap peaks that were broad and merged

**ADVANCED
SCIENCE NEWS**

www.advancedsciencenews.com

**ADVANCED
FUNCTIONAL
MATERIALS**

www.afm-journal.de

together, which may be due to multiple defects in the bandgap.[104] The worse defect tolerance of $Cs_3Sb_2I_9$ compared to LHPs is due to the more localized nature of Sb 5p states compared to Pb 6p, leading to stronger Sb 5p – I 5p antibonding orbitals and a lower EA than in LHPs, which would make donor defects deeper. The deeper acceptor defects are due to weaker Sb 6s – I 5p repulsion, with a lower antibonding state, and hence higher IP.[102] The more prominent role of defects in $Cs_3Sb_2I_9$ may account for its weaker PL compared to LHPs (along with the indirect nature of the bandgap).

$Rb_3Sb_2I_9$ similarly has a layered structure, comprised of corner-sharing SbI_6 octahedra. Cathodoluminescence measurements suggest the presence of deep defects in solution-processed thin films of this material, located at 1.41 and 1.63 eV (compared to an E_g of 2.24 eV). Furthermore, the Urbach energy was high in these samples (>85 meV), and the V_{OC} loss >1.5 V. Defects therefore play a severe role in $Rb_3Sb_2I_9$. PICTS measurements found a trap located 0.62 eV from the band-edge with a high capture cross-section of 6×10^{-14} cm^2, causing a severe effect on non-radiative recombination.[103]

Although $Cs_3Bi_2I_9$ photovoltaics have exceeded the performance of both $Cs_3Sb_2I_9$ and $Rb_3Sb_2I_9$,[101] deep traps are expected to be present based on defect calculations of this material.[101,105] In particular, the Cs_{Bi} and Cs_i defects are expected to have deep transition levels and low formation energies, and are thus expected to act as deleterious recombination centers (Figure 13c). Measurements of the PL decay of large $Cs_3Bi_2I_9$ nanocrystals (9 nm or larger, and therefore probably not quantum confined) gave lifetimes in the range of ≈1 ns to 5 ns,[106,107] and these may be limited by these recombination centers. On the other hand, the acceptor defect V_{Bi} is shallow above the VBM, while the donor defect V_I is very deep, to the extent that it may have a low capture coefficient for electrons. Other point defects have deep transition levels (e.g., Bi_i, Bi_{Cs}, Bi_i, I_i), but have high computed formation energies, and are therefore not expected to be present in sufficient quantities to be harmful. It is suggested that Cs-free analogs to $Cs_3Bi_2I_9$ may avoid harmful traps, since these are mostly from Cs-based point defects.[105] At the same time, in considering hybrid alternatives (e.g., $MA_3Bi_2I_9$), it is important to consider the effects of H vacancies from the alkylammonium cation, since these have been shown to be deleterious in hybrid halide perovskites.[75]

Cs_2TiBr_6 (E_g of 1.78 eV)[108] have reached similar photovoltaic efficiencies as $Cs_3Bi_2I_9$ (≈3%),[103] although the measured PL lifetimes have exceeded the vacancy-ordered triple perovskites described above, with values reaching 24 ns.[109] The V_{OC} loss is moderate, at approximately 0.45 V (maximum V_{OC} of 1.04 V[109]; radiative V_{OC} limit of 1.48 V).[110] The J_{SC} and fill factor losses are, however, more severe. J_{SC} values approaching 6 mA cm^{-2} have been reported, whereas the radiative limit in J_{SC} is 18 mA cm^{-2}. Further work is needed to understand how severe the role of defects are in Cs_2TiBr_6, and whether these limit the performance of this material, or whether the performance is instead limited by carrier localization. Defect calculations have been performed on the smaller-bandgap Cs_2TiI_6 (E_g of 1.02 eV), which have deep traps due to Cs_i, Ti_i, V_I and I_{Ti} (Figure 13d).[108] Given the discussion above, it is likely that these same traps occur in Cs_2TiBr_6, but at deeper levels. On the other hand, it may be possible to suppress deep recombination centers under certain growth conditions, and this requires further investigation.

3.2.3. Ag-Bi-I Semiconductors

Currently, investigations into the defect properties of Ag-Bi-I semiconductors are in their infancy.[48] The materials have bandgaps in the range of 1.7–1.9 eV, and photovoltaic efficiencies under 1-sun illumination have reached up to 4.3% (with Ag_3BiI_6),[48] increasing to 5.56% with the use of S additives in Ag_3BiI_6 because of reductions in bandgap to increase light absorption in the long wavelength range.[111] However, V_{OC}s have reached mostly in the 0.5–0.8 V range,[112] which are well below the radiative limit of 1.4–1.6 V for a 1.7–1.9 eV bandgap solar absorber.[110] Originally, there was speculation that non-radiative losses may arise from pinholes and shunt pathways in thin films, since it is challenging to achieve compact morphology in Ag-Bi-I rudorffites by solution processing.[48] However, intensive efforts to realize dense-morphology rudorffite films (e.g., through hot casting[113] or thermal evaporation)[114] have still yielded poor photovoltaic performance with 1-sun PCEs below 3%.[113,114] This leads to suggestions that $Ag_xBi_yI_{x+3y}$ semiconductors are not defect tolerant, and are limited by defects forming in the bulk and surface of these materials.

Defect calculations on $Ag_xBi_yI_{x+3y}$ are challenging to perform, due to cation disorder (where Ag^+ and Bi^{3+} occupy the same lattice site), and partial occupancies of some lattice sites. However, spectroscopic measurements have been performed on these materials with varying x/y ratios. Iyoda et al. performed time-resolved microwave conductance measurements on a series of Ag-Bi-I stoichiometries, and found that compounds with lower Bi content in the range of 14–50 mol.% had the best combination of mobility and lifetime.[100] This may be rationalized based on the ratio of vacancies in the structure of $Ag_xBi_yI_{x+3y}$ reducing for Ag-rich stoichiometries (**Figure 14**a),[48] and there may possibly be a lower concentration of detrimental traps in these compounds. Indeed, the most efficient Ag-Bi-I photovoltaics are based on Ag-rich Ag_3BiI_6 (see above). At the same time, it is important to avoid the formation of AgI phase impurities, which act as sites of high rates of non-radiative recombination.[112] Fitting transient absorption spectroscopy and terahertz spectroscopy measurements of $Ag_xBi_yI_{x+3y}$ compounds have yielded monomolecular rate constants (k_1) in the range of 10^8–10^9 s^{-1},[112,115] whereas the k_1 constant for $MAPbI_3$ from computations (hybrid functionals with SOC) and experiment are on the order of 10^7 s^{-1}.[75]

Attempts have been made to identify the dominant recombination centers in $Ag_xBi_yI_{x+3y}$ compounds through PICTS and Fourier-transform photocurrent spectroscopy (FTPS). PICTS measurements of $AgBiI_4$ identified two centers, located at 0.25 eV and 0.33 eV, and both with low capture cross-sections of 10^{-19} cm^2, indicating that they are comparatively benign[103] (Figure 14c). By contrast, FTPS measurements (shown in Figure 14b) identified a deep defect located at 0.6 eV from a band-edge of $AgBi_2I_7$.[112] The authors suggest that such deep traps are consistent with the high k_1 values and high V_{OC} loss, and could also be present in other rudorffite stoichiometries. Such deep traps may not have been identified in PICTS measurements
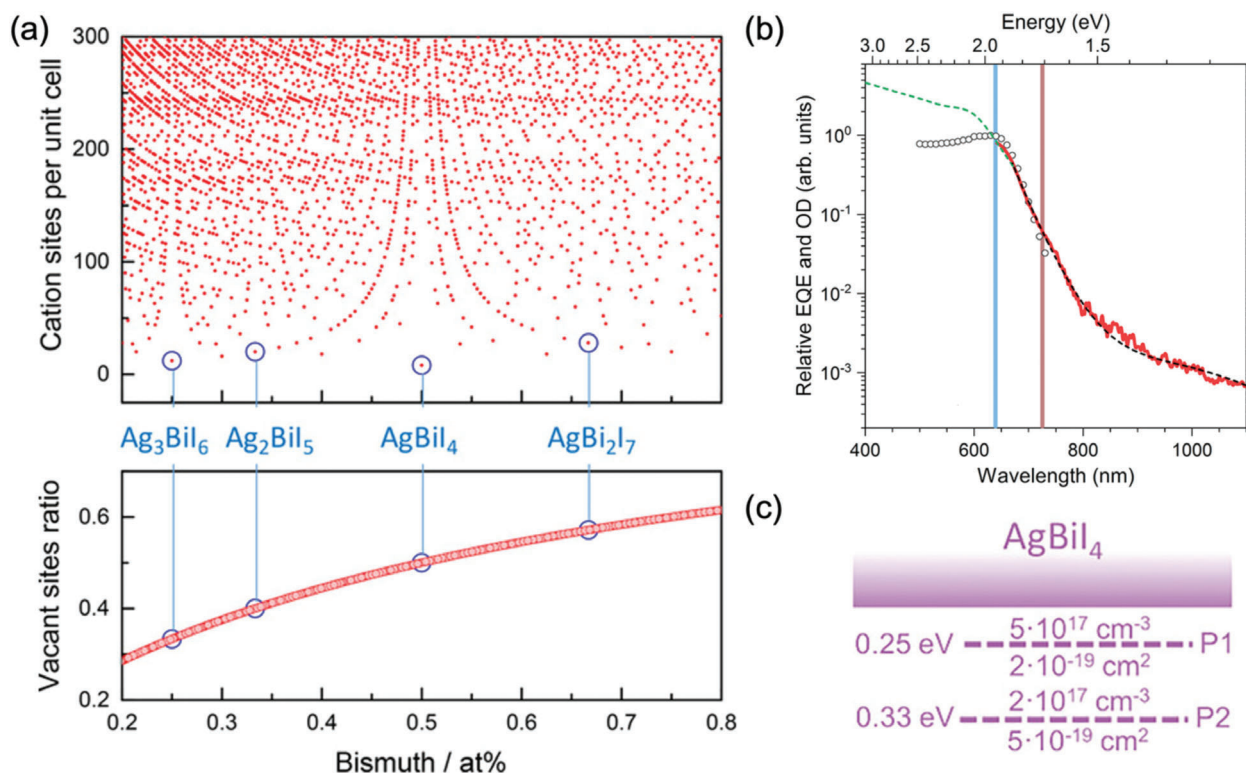
Figure 14. Defects in Ag-Bi-I semiconductors. a) Plot of $Ag_xBi_yI_{x+3y}$ compounds of different stoichiometries if they were all based on the $NaVO_2$-type structure, showing the cation sites per unit cell versus bismuth content (top), and the fraction of the cation sub-lattice that is occupied by vacancies (bottom). Reproduced with permission.[48] Copyright 2017, Wiley-VCH. b) Superposition of external quantum efficiency (EQE; black circles), steady-state absorption (dashed green line) and Fourier transform step-scan photocurrent spectroscopy (red line) measurements of $AgBi_2I_7$ films and devices. Reproduced with permission from Ref. [112] Copyright 2023, American Chemical Society. c) Summary of the main traps in $AgBiI_4$ determined from Photoinduced Current Transient Spectroscopy measurements. Reproduced under the terms of the CC-BY licence.[103] Copyright 2021, The Authors, published by Wiley-VCH.

because the signature from these deep traps may have been too weak to measure above the response from other components. In addition, the Urbach energy of $AgBi_2I_7$ was found to be 70 meV, and this was attributed to the presence of shallow traps, as well as due to carrier-phonon coupling effects.[112] Finally, we note that like $Cs_2AgBiBr_6$, $AgBiI_4$ was found to exhibit carrier localization, with a high fitted localization rate of 1–2 ps^{-1}.[115]

3.2.4. Chalcohalides

As discussed earlier in Section 3.1, BiOI has evidence from both computations and experiment of being able to tolerate common point defects, such as V_I and V_{Bi}. PICTS measurements on BiOI thin films showed there to be three states at 0.27, 0.53, and 0.54 eV from the band-edge, with capture cross-sections of 10^{-20}, 10^{-16}, and 10^{-15} cm^2, respectively. The concentrations of these states were ≈10^{16} cm^{-3}.[103] If these were recombination centers, the third defect (0.54 eV, 10^{-15} cm^2 capture cross-section) would be harmful. However, after intentionally introducing defects through vacuum annealing at 100 °C, it was found that the concentration of these defects did not significantly change from 10^{16} cm^{-3}, despite the surface stoichiometry changing over the percent level.[83] The origin of these states needs to still be

established. One possibility is that these states arise due to the local minima in the excited-state potential energy surface that occurs due to electron-phonon coupling in BiOI (illustrated in Figure 10f), from which charge-carriers can be thermally re-excited via a multi-phonon emission process, as with defects.[84]

Another chalcohalide PIM investigated is BiSI. Although this material has sizeable spin-orbit coupling and a noticeable contribution of the Bi 6s orbital to the upper valence band density of states,[116] it has only reached modest photovoltaic efficiencies of 1.3%.[117] Defect calculations performed by Ganose et al. on BiSI showed that a number of deep recombination centers exist with low formation energy, namely V_S, as well as S and Bi interstitials, and Bi_S and S_{Bi} anti-sites.[118] Overall, Bi-poor and S- and I-rich conditions were predicted to give rise to fewer detrimental defects, with higher formation energies for the dominant deep defects (S_{Bi} and V_S), but it will be important to adopt growth conditions to minimize the formation of sulfur vacancies,[118] such as by cooling down furnace-grown samples with a S overpressure. Ganose et al. also examined the case of BiSeI, but found that deep traps and high rates of non-radiative recombination would prevail under both p- and n-type growth conditions, due to a complementary set of defects with deep traps and low formation energies under each condition. It is suggested that moving towards moderate chemical potentials could mitigate these deep traps the
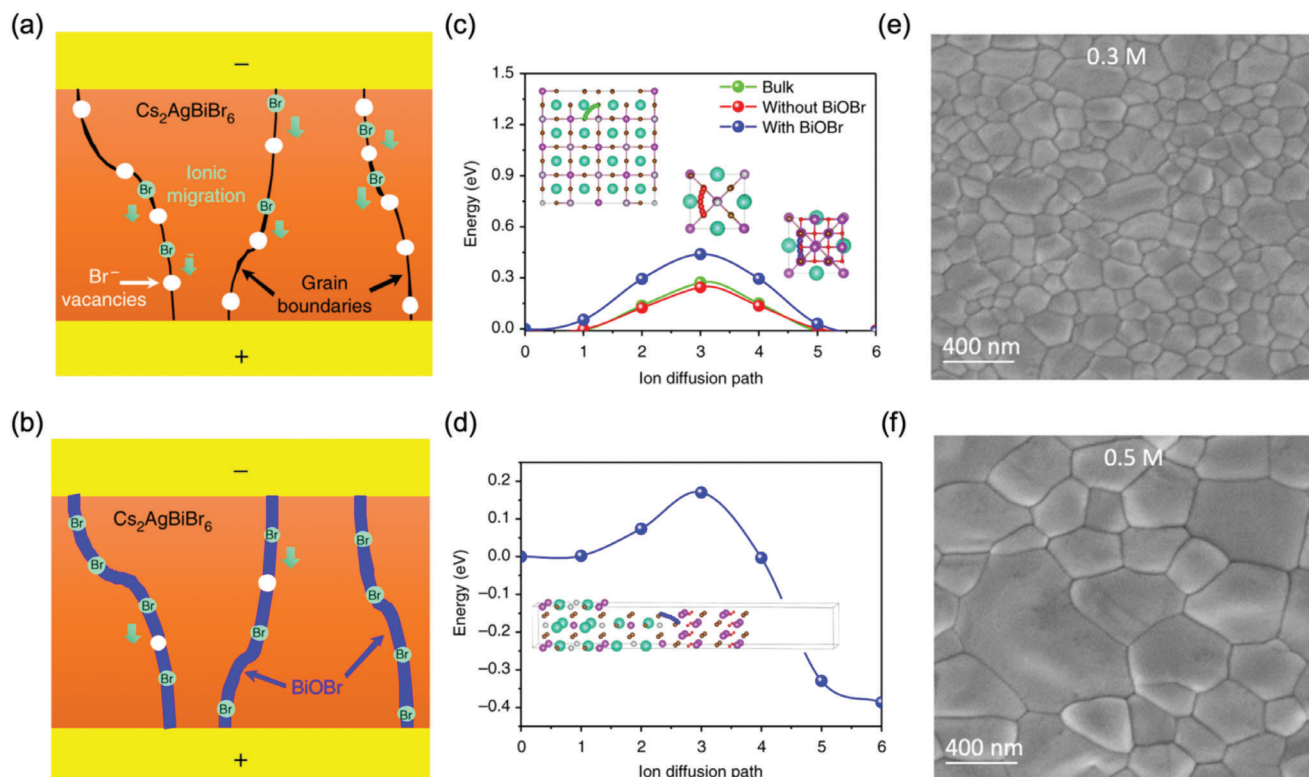
Figure 15. Strategies to mitigate the effects of defects in $Cs_2AgBiBr_6$. Illustration of the grains in $Cs_2AgBiBr_6$ pressed pellets a) without passivation and b) with BiOBr heteroepitaxial passivation. Calculated energy profile for V_{Br} migration c) in the bulk, compared to in-plane migration on the surface without and with BiOBr passivation, and d) in the out-of-plane direction. Parts (a)–(d) reproduced under the terms of the CC-BY license.[119] Copyright 2019, The Authors, published by Springer Nature. Scanning electron microscopy images of $Cs_2AgBiBr_6$ deposited from e) 0.3 mol L^{-1} (118 ± 4 nm thick) and f) 0.5 mol L^{-1} (242 ± 6 nm thick) precursor solutions. Parts (e) and (f) reproduced under the terms of the CC-BY license.[95] Copyright 2021, The Authors, published by Wiley-VCH.

most.[118] Overall, the more challenging defect chemistry of BiSeI may account for the sparsity of photovoltaic performance data for this material.

3.3. Effective Strategies for Mitigating the Role of Defects in Wide-Bandgap Perovskite-Inspired Materials

From the discussion made in Section 3.2 on the defect chemistry of wide-bandgap PIMs, it can be seen that tuning the chemical potentials during growth is expected to be an effective strategy to mitigate the concentration and effects of harmful defects. Apart from tuning growth conditions, passivation is a valuable strategy. Yang et al. improved the performance of $Cs_2AgBiBr_6$ through heteroepitaxial passivation with BiOBr.[119] This was achieved through isostatic pressing of CsBr, AgBr and excess $BiBr_3$ powders together and annealing in air at 350 °C to form $Cs_2AgBiBr_6$ with BiOBr covering the surface of the halide elpasolite, and perhaps also at grain boundaries (**Figure 15**a,b). The distance between Br atoms in the unit cell of BiOBr (3.915 Å) is close to the distance between Br atoms in $Cs_2AgBiBr_6$ (3.977 Å), allowing lattice-matched growth of the heteroepitaxial layer with few defects at the interface. BiOBr forms a Type II heterojunction with $Cs_2AgBiBr_6$, and that can thus enable passivation, whilst also enabling electron extraction. It was found that growing the

BiOBr layer increased the PL lifetime, and also increased the resistivity of $Cs_2AgBiBr_6$ from 10^9 Ω cm to 10^{10} Ω cm, along with an increased activation energy barrier to ion migration. All three effects can be explained by the passivation of V_{Br}. Simulations also confirmed that the diffusion barrier to Br^- migration on the surface of $Cs_2AgBiBr_6$ increased from 250 meV to 440 meV (in-plane; Figure 15c), or 560 meV (out-of-plane; Figure 15d) with BiOBr.[119]

Similarly, Sansom et al. found that $CuAgBiI_5$ substantially improved in PL intensity after storing in air for 90 min.[46] They attributed these observations to oxygen passivation of deep recombination centers. Consistent with this explanation, the PL lifetime increased after air exposure.[46] However, it is not known what oxygen-based species formed on the surface. In an earlier work on $MA_3Bi_2I_9$, it was found that after storing thin films of this material in air for 25 days, extra diffraction peaks attributable to Bi_2O_3 or BiOI appeared.[120] Possibly a related species forms on the surfaces of the $CuAgBiI_5$ after air exposure.

Another approach is to use ligands for passivation, as has been extensively explored in LHP nanocrystals.[65] Santra and co-workers developed the synthesis of layered $Cs_3Sb_2I_9$ nanocrystals by hot injection, and found oleylamine and octanone ligands on the surface. These passivating ligands improved the environmental stability of these materials, and the authors suggested that these ligands could also inhibit iodine diffusion.[41] The use of

2307441 (17 of 52)

**ADVANCED
SCIENCE NEWS**

www.advancedsciencenews.com

**ADVANCED
FUNCTIONAL
MATERIALS**

www.afm-journal.de

oleate and octylammonium halide ligands was also found to passivate surface defects in $Cs_3Bi_2Br_9$ nanocrystals, improving the PLQYs by over an order of magnitude to the range of 4.5–22%.[121]

Cl-doping is also effective for passivating defects in $MA_3Bi_2Br_9$ and $Cs_3Sb_2I_9$.[122,123] Tang and co-workers found that incorporating MACl and $BiCl_3$ into the precursors during the synthesis of $MA_3Bi_2Br_9$ by ligand-assisted re-precipitation, and concluded that Cl^- was incorporated into the lattice of the nanocrystals. Increasing the Cl content led to an increase in the PLQY (up to 54.1%) and PL lifetime, and this was attributed to Cl passivating surface defects on the nanocrystals.[122] For $Cs_3Sb_2I_9$, Paul et al. incorporated Cl into the 2D lattice by using $SbCl_3$ in the precursor, and up to 1/9 of the halide site was substituted for Cl.[123] There were minimal changes to the bandgap, but Cl incorporation led to the grain size doubling from 230 nm (no Cl) to 400 nm (1/9 Cl), and samples with 0.56/9 to 0.71/9 Cl had the slowest decay in the time-resolved microwave conductance transients.[123] This correlated with the greatest improvement in photovoltaic performance up to 2.0–2.2% PCE (from 1.4% with no Cl), and suggests that Cl incorporation passivated defects in $Cs_3Sb_2I_9$.[123]

Finally, grain boundaries often act as sites of non-radiative recombination, as found, for example from cathodoluminescence mapping measurements of $Cs_2AgBiBr_6$, in which grain boundaries were darker than the bulk.[95] As with other classes of thin film semiconductors, finding approaches to minimize the density of grain boundaries can reduce the overall defect density, as well as realize other benefits, such as improved mobilities (through reduced grain boundary scattering) and reducing the density of pathways for ion migration. The grain size of $Cs_2AgBiBr_6$ was increased by increasing the thickness of the films (since grain size is limited by film thickness[124]), as shown in Figure 15e,f, and in the case of $Cs_3Sb_2I_9$ was increased through Cl doping.[123] A wide range of other strategies have also been adopted (both for PIMs, and more generally for thin film semiconductors), including hot casting and post-synthetic vapor annealing.[113,124]

4. Optoelectronic Properties

4.1. Optical Properties

In this section, we briefly review the absorption, bandgap, and photoluminescence, which are crucial properties of PIMs (**Table 1**) dictating their performance in optoelectronics.

Halide elpasolites, such as $Cs_2AgBiBr_6$, show indirect bandgaps and absorption coefficients in the 10^2–10^4 cm^{-1} range at the band-edge, thus lower than those of LHPs (10^5 cm^{-1}).[94,125] The bandgap values of $Cs_2AgBiBr_6$ are in the 1.95–2.19 eV range (the bandgap of the Cl analog is 2.77 eV),[94] higher than for other PIMs.[94] Tunable bandgaps between 2.08 and 2.25 eV and bandgap bowing effect have been reported for $Cs_2Ag(Sb_xBi_{1-x})Br_6$.[126] $Cs_2AgBiBr_6$ has been characterized by a weak and broad self-trapped exciton (STE) emission (red-shifted from the absorption band edge) centered at ≈2 eV.[98] The limited charge carrier mobility of ≈0.5–1.0 cm^2 V^{-1} s^{-1} (≈12 cm^2 V^{-1} s^{-1} for single crystals) of $Cs_2AgBiBr_6$ has been attributed to the carrier self-trapping process,[71,98,127] which causes V_{OC} losses and performance drop of the corresponding photovoltaic devices despite an impressive charge carrier lifetime of 1.4 μs.[94] In addition, despite the 3D crystal structure, a very high exciton binding energy of 268 meV was reported for $Cs_2AgBiBr_6$,[128] which suppresses its high photovoltaic performance.

In the case of $Cs_3Sb_2I_9$, the 0D dimer is a photoinactive phase, while the 2D layered structure is a photoactive phase with an absorption coefficient of 10^5 cm^{-1}.[129] The 2D structure has a lower exciton binding energy than the 0D dimer.[130] The 2D $Cs_3Sb_2I_9$ exhibits direct and indirect bandgaps of 2.05 and 1.95 eV, respectively, suggesting its quasi-direct bandgap nature.[131] Strong carrier-phonon coupling has been found in $Cs_3Sb_2I_9$ (and other $A_3M_2I_9$, where A = Cs, Rb and M = Bi, Sb) as a result of a high Huang−Rhys parameter (S = 42.7), which leads to a weak and broad STE emission.[132] The nanosecond PL lifetime of $Cs_3Sb_2I_9$ films and single crystals[129,130,133,134] suggests a high density of trap states. By contrast, emission lifetimes of $A_3Bi_2I_9$ (A = Cs, MA) single crystals extend to the microsecond range, thus implemented in high-performance X-ray detectors.[135,136]

Cs_2TiBr_6 is a promising VOHP absorber leveraging an eco-friendly and earth-abundant element at the B site (i.e., Ti) with a quasi-direct bandgap of 1.8 eV and charge carrier diffusion lengths greater than 100 nm.[109] The PL and stability aspects of this material have been under debate.[137,138] By employing a colloidal hot-injection synthesis, Grandhi et al. obtained stable and nonemissive Cs_2TiBr_6 nanocrystals,[76] consistently with the findings from Euvrard et al.[137] Cs_2SnI_6 is a suitable candidate for photovoltaics and photodetector applications due to its bandgap of around 1.3–1.6 eV, the broadband absorption, the absorption coefficient of 10^5–10^6 cm^{-1}, and good charge carrier mobility (≈10–500 cm^2 V^{-1} s^{-1}).[139] Cs_2TeI_6 exhibits a bandgap of 1.5 eV an absorption coefficient of 10^5–10^6 cm^{-1}, but a low charge carrier lifetime of 2.6 ns.[87] This indirect bandgap material has not been extensively explored in photovoltaics.[87] Moreover, tellurium imparts mild toxicity to Cs_2TeI_6.

Various Ag-Bi-I semiconductors exhibit direct bandgaps in the 1.60–1.93 eV range and high absorption coefficients of 10^5–10^6 cm^{-1}.[140,45] However, $AgBiI_4$ and Ag_2BiI_5 were found to have high exciton binding energies of 260 and 150 meV, respectively. Ghosh et al. realized that fabrication conditions significantly impact the film quality and charge transport characteristics of Ag-Bi-I compounds.[113] Charge carrier lifetimes of $AgBiI_4$ and Ag_2BiI_5 were increased from 23 to 75 and 83 to 133 ns when the film processing procedure changed from spin-coating to dynamic hot casting.[113] A charge carrier mobility of ≈2.3 ± 0.3 cm^2 V^{-1} s^{-1} was achieved for the Ag_2BiI_5 films.[113] Furthermore, very weak to no photoluminescence and short PL lifetimes of a few nanoseconds of Ag-Bi-I compounds can be attributed to dominant high nonradiative recombination and symmetry-forbidden transitions.[48,113,141] On the other hand, quaternary Cu_2AgBiI_6 exhibits a direct bandgap with an absorption coefficient of 1×10^5 cm^{-1}, a low exciton binding energy of 25 meV, and a PL lifetime of 33 ns.[51] However, the charge carrier mobility in this case also is limited by the carrier self-trapping.[51]

In the context of lead-free perovskite materials, the incorporation of transition metals and chalcogen elements has been proposed to improve their properties through bandgap engineering.[6] The bandgaps of chalcohalide materials can be tuned from 0.7 to 3.0 eV by varying the composition of chalcogen and halogen elements.[7] Chalcohalides have layered or 1D ribbon-like structures and strong anisotropy in their optical and

**ADVANCED
SCIENCE NEWS**

www.advancedsciencenews.com

**ADVANCED
FUNCTIONAL
MATERIALS**

www.afm-journal.de

Table 1. Summary of the optical properties of various PIMs.

PIM composition	Bandgap [eV]/nature	Valence band [eV]	Conduction band [eV]	Emission maximum [eV]	Ref.
$Cs_3Bi_2I_9$	1.9/direct	−5.70	−3.40	1.93 (STE)	[132, 144]
$Rb_3Bi_2I_9$	2.10/direct	−6.00	−3.80	–	[144]
$K_3Bi_2I_9$	2.10/direct	−6.10	−3.90	–	[144]
$MA_3Bi_2I_9$	2.26/indirect	−5.95	−3.69	2.05	[145]
$FA_3Bi_2I_9$	2.19	–	–	1.98	[146]
$(NH_4)_3Bi_2I_9$	2.1	−5.70	−3.60	–	[147]
$CsBi_3I_{10}$	1.77/ direct	−5.90	4.15	1.77	[148–150]
$MABi_3I_{10}$	1.95	−6.10	4.15	–	[149]
$FABi_3I_{10}$	1.90	−6.00	4.10	–	[149]
$Cs_2AgBiBr_6$	2.39/indirect	−6.39	−4.00	2.42	[151]
Ag_3BiI_6	1.87	−5.51	−3.64	1.72	[48]
$AgBiI_4$	1.86/ indirect	−5.87	−4.01	–	[152]
$AgBi_2I_7$	1.83/direct	−6.00	−4.30	–	[153]
Ag_2BiI_5	1.90	−5.80	−4.10	–	[153]
Cs_2NaBiI_6	1.66	−5.82	−4.16	–	[154]
$BiOI$	1.93/indirect	−6.10	−4.20	1.77	[155, 156]
$ATBiI_4$	1.78	−4.90	−3.10	–	[157]
Cu_2AgBiI_6	1.91/direct	−5.25	−3.35	1.71 (STE)	[158–161]
$MA_3Sb_2I_7Cl_2$	2.13/indirect	–	–	–	[162]
$Cs_3Sb_2[Cl_xI_{9-x}]$	1.95/ near-direct	−5.36	−3.14	1.96	[155]
$Cs_{2.4}MA_{0.5}FA_{0.1}Sb_2I_{8.5}Cl_{0.5}$	2.1/direct	–	–	1.57 (STE)	[163]
$Cs_2AgSbBr_6$	2.18 / indirect	−5.63	−3.45	–	[164]
$MA_3Sb_2I_9$	2.14/ indirect	−5.50	−3.30	–	[165]
$MASbSI_2$	2.03/ indirect	−5.87	−3.84	2.53	[166]
$Cs_3Sb_2I_9$	2.05/ direct	−5.16	−3.11	1.91 (STE)	[129, 165, 167]
$Rb_3Sb_2I_9$	2.0	−5.54	−3.30	1.92	[132, 168]
Cs_2TiBr_6	1.8/indirect	−5.80	−4.00	1.76	[169,170]
$BiSI$	1.57/direct	−6.20	−4.60	1.56	[171]
$SbSI$	2.15	−5.50	−3.35	2.40	[172]
$Sb_{0.67}Bi_{0.33}SI$	1.62	−5.71	−4.09	–	[56]

charge-carrier transport properties. They offer defect-tolerant transport properties due to their high dielectric constants, low effective masses, and antibonding character of the valence band. BiOI possesses an indirect bandgap of ≈1.9 eV and absorption coefficients >10^4 cm^{-1},[82] whereas BiSI has a lower bandgap of 1.57 eV.[117] Both BiOI and BiSI are characterized by PL lifetimes of a few nanoseconds. While such a short lifetime in the case of BiSI was attributed to sulfur vacancies (deep traps),[117] the origin for the same is unclear in the case of Bi. On the other hand, the SbSI is an indirect bandgap material with a bandgap of 2.15 eV.[142] However, its large dielectric constant of 1.6×10^4 (measured at 292 K)[143] may suppress the influence of charged defects and improve its defect tolerance.

4.2. Charge-Carrier Transport in PIMs

Efficient charge transport is essential for obtaining high-performance PIM-based optoelectronic devices.[66,173–176] The charge transport properties, such as carrier mobility, conductivity, lifetime, and diffusion length, are highly dependent on the i) intrinsic (interstitials)[177,178] and extrinsic defects (for instance, halide vacancies and surface defects) induced in the film during the processing steps (see Section 3.1),[174,179,180] ii) disordered crystal structure,[175,177] iii) structural defects,[174,175] iv) charge carrier-phonon coupling,[181] and v) physical parameters[66] (dielectric constant and effective mass) of PIMs. The carrier mobility and conductivity values of a few PIM materials realized experimentally are summarized in **Table 2**. The discrepancies in these two parameters for a given PIM compositions may be attributed to various processing techniques, leading to different surface quality and defects in films.[158,182–184] The defects in the PIM films can be minimized by improving the crystallinity, and obtaining compact, dense, and larger grains with fewer boundaries,[158,179,185] in turn, enables a superior diffusion length, enhanced carrier lifetime, and high mobility desired for the efficient charge separation and transport in the PIM films.[158,179,182,185,186] Partially replacing I$^-$ with Cl$^-$

**ADVANCED
SCIENCE NEWS**

www.advancedsciencenews.com

**ADVANCED
FUNCTIONAL
MATERIALS**

www.afm-journal.de

Table 2. Charge transport properties of lead-free PIMs.

PIM	Process	Film thickness [nm]	σ [S cm^{-1}]	Electron/hole, n_e/n_h [cm^{-3}]	Mobility [cm^2 V^{-1} s^{-1}]	Ref.
Cs_2SnI_6	Co-evaporation of SnI_2, CsI and followed by annealing in I vapor at 50 °C	600	0.1099	2.0×10^{15}	509	[210]
Cs_2SnI_6	E beam evaporation of CsI film followed by annealing in $SnI_4 + I_2$ vapor	N/A	N/A	7.18×10^{14}	329	[211]
Cs_2SnI_6	Spin coating process	600–800		3.65×10^{19}	382	[212]
Cs_2SnI_6	Thermal evaporation of CsI films and followed by annealing in SnI_4 vapor	350	N/A	6×10^{16}	2.9	[33]
$Cs_3Bi_2I_9$ single crystals	Inverse temperature crystallization	N/A	N/A	N/A	4.57	[213]
$Cs_3Sb_2I_9$ microplate	CVD	N/A	N/A	4×10^{13}	33	[214]
$Cs_3Sb_2I_9$ –HCl films	Solution spin coating	N/A	N/A	N/A	6.81	[179]
$Rb_3Sb_2I_9$ films	Solution spin coating process	N/A	N/A	2.64×10^{13}	250	[104]
$Cs_2AgBiBr_6$ films	Solution spin coating	N/A	N/A	N/A	1.7	[215]
$Cs_2AgBiBr_6$ single crystals	Inverse temperature crystallization	N/A	N/A	N/A	11.81	[216]
$Cs_2AgBiBr_6$ films	Solution spin coating	N/A	N/A	N/A	0.99×10^{-3}	[189]
$Cs_2AgBiBr_6$:Na$^+$ films	Solution spin coating	N/A	N/A	N/A	1.45×10^{-3}	[189]
$Cs_2AgBiBr_6$:Ce^{3+} films	Solution spin coating	N/A	N/A	N/A	1.62×10^{-3}	[189]
$Cs_2AgBiBr_6$:Na$^+$,Ce^{3+} films	Solution spin coating	N/A	N/A	N/A	1.94×10^{-3}	[189]
$MA_3Bi_2I_9$ films	2T-CVD	N/A	N/A	N/A	0.22	[182]
$MA_3Bi_2I_9$ (MBI)) films	CVD	400 nm	N/A	N/A	0.03	[217]
$MA_3Bi_2I_6Cl_3$ (MBIC)) films	CVD	400 nm	N/A	N/A	0.162	[217]
$Cs_3Cu_2I_5$	Solution spin coating	N/A	N/A	N/A	0.036	[218]

in iodide PIMs can enhance the carrier lifetime and mobility with restrained recombination.[173,187,186] The metal ion doping[178,188,189] and polymer additive[190] strategies can offer pinhole-free films with larger grains and reduce the number of carrier trapping centers and grain boundaries, thereby enhancing carrier mobility in the PIM films.[190] The surface passivation by ionic liquids[191–193] and organic additives, such as 2,3,5,6-tetrafluoro-7,7,8,8-tetracyanoquinodimethane (F4-TCNQ),[194] and phenethylammonium iodide (PEAI),[195] effectively mitigate the trap formation in the PIM films, thus leading to improved carrier transport in their optoelectronic devices. The temperature-dependent electrical conductivity study is a powerful tool for elucidating influence of defects on charge transport in PIMs.[183,196–198] For instance, the temperature-dependent electrical conductivity trend of Cs_2SnI_6 shows two different slopes, implying that distant conduction mechanisms operate in the measured temperature range of 148–378 K.[183] The increase in conductivity above 273 K is speculated to be thermally activated defect states with optical bandgap.[183,199] The estimated activation energy ($\approx$110 meV) lies within the range of the theoretically calculated ΔH of V_I and Sn_i defects.[37,183] In a word, the increase in the electrical conductivity with temperature

is mainly attributed to the exponential rise in the number of free carriers, partially accelerated by internal trap-based excitation in the donor-like defect states (Sn_i and V_I) located below the conduction band of Cs_2SnI_6.[37,183,199] The thermal activation of intrinsic and extrinsic defects by increasing the temperature leads to the declined performance of other PIM-based optoelectronic devices (solar cells,[177,200] photodetectors,[183,191,201–204] memristors,[205–208] field-effect transistors (FETs),[209] and others).[183,209] In conclusion, a temperature-dependent electrical conductivity study helps understand the mechanism of charge transport properties and operational stability in the implemented PIM for optoelectronic devices.

In summary, although most of the PIMs discussed in this section possess high absorption coefficients and direct-to-near direct bandgaps, they display low PLQYs and short lifetimes, mainly arising from the dominant non-radiative recombination processes. In addition, the charge transport properties of PIMs are hindered by their low charge carrier mobilities, conductivities, and diffusion lengths. The intrinsic defects, the non-continuous film morphology with small grains or domains, and the ineffective surface passivation contribute to the poor charge transport properties of PIMs.

**ADVANCED
SCIENCE NEWS**

www.advancedsciencenews.com

**ADVANCED
FUNCTIONAL
MATERIALS**

www.afm-journal.de

Table 3. A summary of the record holding device efficiencies for each material system under AM 1.5G.

	PIM	Bandgap [eV]	PCE [%]	V_{OC} [V]	J_{SC} [mA cm^{-2}]	FF [%]	Ref.
Halide Elpasolites	$Cs_2AgBiBr_6$	1.64	6.37	0.92	11.40	60.93	[96]
	MA_2AgAgX_6	1.38	0.007	0.33	0.052	41.04	[244]
	Cu_2AgBiI_6	2.06	2.45	0.71	5.30	65	[239]
	$MA_3Sb_2I_{9-x}Cl_x$	2.05	3.34	0.70	7.38	65	[162]
Vacancy Ordered	$Cs_2SnI_4Br_2$	1.40	2.10	0.56	6.23	57	[251]
	Cs_2TiBr_6	1.82	3.30	1.02	5.69	56	[109]
(Cu-)Ag-Bi-I	$CuBiI_4$	1.81	1.1	0.38	7.18	28.67	[262]
	Ag_3BiI_6	1.83	4.3	0.63	10.7	64	[48]
	$Ag_3BiI_{5.92}S_{0.04}$	1.84	5.44	0.569	14.6	65.7	[111]
Chalcohalide	$MASbSI_2$	2.03	3.08	0.65	8.12	58.5	[277]
	$MA_3Bi_2I_{9-2x}S_x$	1.67	0.152	0.52	0.58	47.6	[278]
	$BiSI$	1.51	1.32	0.445	8.44	35.14	[117]
	$SbSI$	2.10	3.62	0.6	9.26	65.2	[280]
	$Sb_{0.67}Bi_{0.33}SI$	1.62	4.07	0.53	14.54	52.8	[56]
Chalcogenide	$AgBiS_2$	1.1	9.17	0.495	27.1	68.4	[53]

5. Photovoltaics

5.1. Solar Cells

Solar cells based on PIMs aim to branch out from the established ABX_3 metal halide paradigm, in the hope that new non-toxic materials can also achieve both the high photovoltaic performance and ease of device fabrication that have caused LHPs to be so successful. As discussed in the previous sections, PIMs span a wide range of structural and chemical diversity, resulting in a myriad of optoelectronic and photovoltaic properties, and caveats that must be considered when aiming to fabricate performant solar cell devices.[9]

In this section, we aim to summarize the key developments within solar cells based upon PIMs, such as halide elpasolites, vacancy-ordered perovskites, rudorfittes/pnictogen-based metal halides, chalcohalides, and chalcogenides (**Table 3**). State-of-the-art devices will be described and the current ongoing efforts (i.e., optimized device engineering, doping strategies, and simulation studies) to combat performance limitations will be discussed.

5.1.1. Halide Elpasolites

While many B^{3+} = Bi, Sb, In, Fe, and Tl-based halide elpasolites have been determined to possess promising photovoltaic properties, presently only a few materials have been used in solar cells, such as Cs_2AgBiX_6 and its doped derivatives, Cu_2AgBiI_6, $MA_2Au_2Br_6$, and $Cu_3Sb_2I_9$.[221,222] Of these, $Cs_2AgBiBr_6$ is considered the front runner, with reported PCE's rising from 2.43% to 6.37% in the last 6 years.[96,223] However, there are a number of intrinsic trade-offs that limit device performance. Indeed, $Cs_2AgBiBr_6$ possesses a wide indirect bandgap ≈1.95 eV[97] a modest absorption coefficient of 4×10^4 cm^{-1} above 2.5 eV,[94] and is defect intolerant.[224] Consequently, a lackluster J_{SC} (≈3.7 mA cm^{-2}) was observed in the first pure phase $Cs_2AgBiBr_6$ devices, and thus efforts in device engineering to improve charge extraction, or doping strategies to improve absorption via bandgap alteration, have become commonplace.[223]

In terms of device engineering, sensitizing the TiO_2 electron transport layer (ETL) has been shown to improve device performance, as it can enhance electron extraction, energy level alignment, reduce interfacial defects, and offer improved light harvesting. Indeed, a chlorophyll-derivative sensitized TiO_2 ETL reduced defects and suppressed interfacial charge recombination, resulting in improved J_{SC} of 4.09 mA cm^{-2}.[225] While a combined approach of sensitizing TiO_2 with photoactive D149, alongside adding MXene nanosheets to the $Cs_2AgBiBr_6$ active layer, yielded a J_{SC} of 8.85 mA cm^{-2}, PCE ≈4.47% under AM1.5 G.[226]

Despite modest improvements, engineering strategies alone cannot overcome the suboptimal bandgap and absorption of $Cs_2AgBiBr_6$, and so intrinsic modification of the perovskite active layer via doping/alloying has been investigated. Indeed, there are numerous reports of attempts utilizing A site materials (MA, Li, Na, K, and Rb) to modify film morphologies, slightly alter the bandgap, and reduce defects, B site metals (In, Sb, Tl, Sn, Cu) to alter bandgaps or introduce sub band states for increased absorption, and X site (I, Cl, S) modification to further tune the bandgap.[126,227–235] However, only few of these materials have currently been applied to functional solar cells, and their efficiencies still lag behind those achieved via engineering strategies. For example, an A-site Rb doped $(Cs_{1-x}Rb_x)_2AgBiBr_6$ yielded a marginally increased J_{SC}, FF, and PCE.[219] As a result, the PCE of the $Cs_2AgBiBr_6$ device was improved to 1.39% from 1.21% upon replacing 10% of Cs with Rb (**Figure 16**a).[219] Whereas alloying various percentages of B-site Sb^{3+} into $Cs_2Ag(Sb_xBi_{1-x})Br_6$ films, resulted in a reduced bandgap of 2.08 eV and PCE of 0.25% (2.22 eV, 0.19% undoped).[236] Alternatively, sulfide modification $Cs_2AgBiBr_{6-2x}S_x$ has also produced an enhanced PCE of 2.0% (undoped 1.4%), due to enhanced absorption and J_{SC}.[229]

The current state-of-the-art $Cs_2AgBiBr_6$ solar cell relies upon a novel method of plasma post-treatment, to dope hydrogen atoms into interstitial sites in the crystal lattice, resulting in a significant bandgap reduction from 2.18 eV to 1.67 eV, a stark color
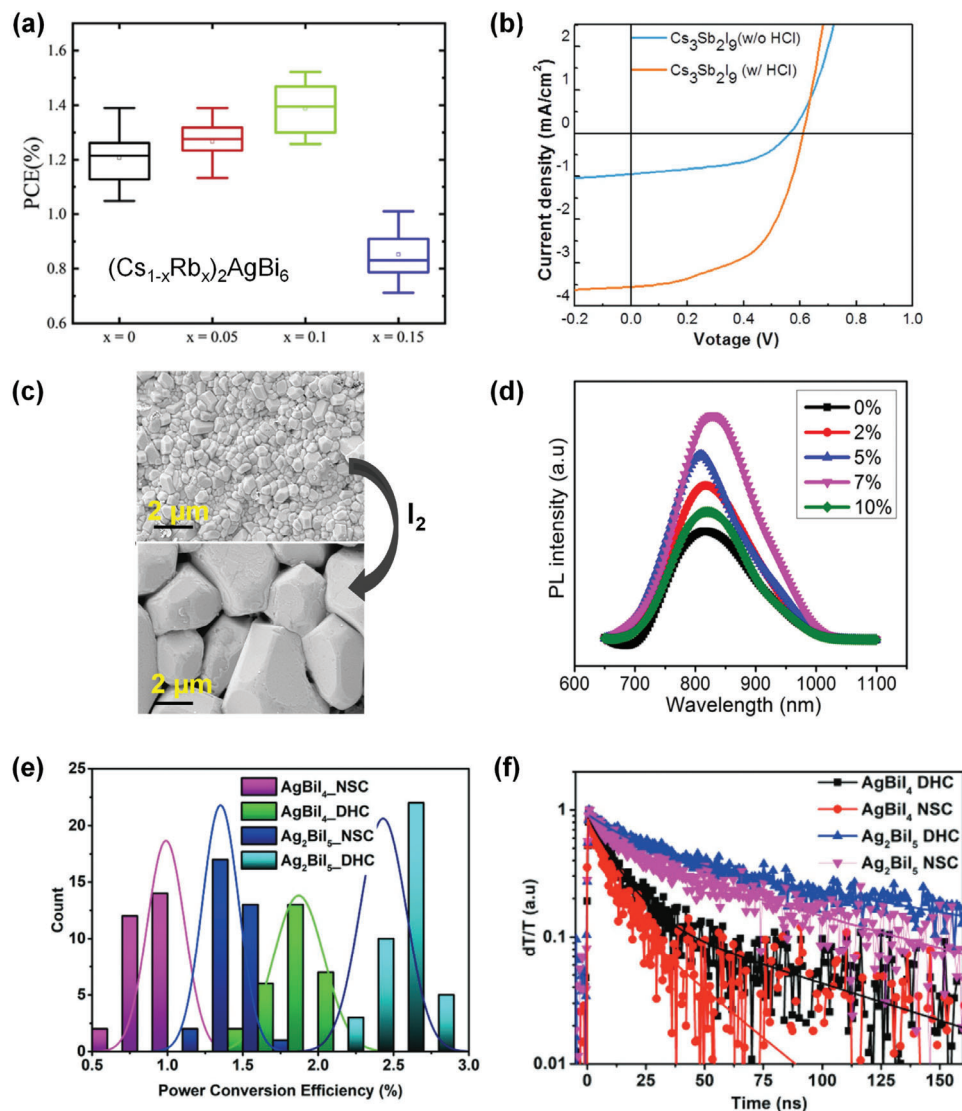
**ADVANCED
SCIENCE NEWS**

www.advancedsciencenews.com

**ADVANCED
FUNCTIONAL
MATERIALS**

www.afm-journal.de

Figure 16. a) PCE distribution of $(Cs_{1-x}Rb_x)_2AgBi_6$ solar cells (20 devices). Reproduced with permission.[219] Copyright 2019, Elsevier. b) J–V curves of $Cs_3Sb_2I_9$ solar cells with and without HCl treatment. Reproduced with permission.[129] Copyright 2019, Wiley-VCH. c) SEM images of Cs_2SnI_6 films fabricated with (bottom) and without (top) 7% I_2. d) PL spectra of Cs_2SnI_6 films prepared at 200 °C under varying I_2. Panels (c) and (d) are reproduced with permission.[220] Copyright 2021, Wiley-VCH. e) PCE distribution of $AgBiI_4$- and Ag_2BiI_5-based solar cells with conventional and dynamic spin-coating techniques applied for the absorber layers. f) Photobleach decay dynamics (collected at 590 or 605 nm) of Ag-Bi-I thin films fabricated with conventional and dynamic spin-coating techniques. Panels (e) and (f) are reproduced with permission.[113] Copyright 2018, Wiley-VCH.

transformation from yellow to black, and greater carrier mobilities and lifetimes. This collectively results in an AM1.5 G PCE of 6.37%,[96] a significant improvement that offers hope for future high-performance devices. A recent study numerically optimized hydrogenated $Cs_2AgBiBr_6$ devices with respect to various transport materials and their energetic alignments, absorber layer thicknesses and associated defect densities, and series and shunt resistances, to ascertain the combination that would yield the upmost performance: a $FTO/Nb_2O_5/Cs_2AgBiBr_6/CuI/Cu$ stack with ≈1.14 V V_{OC}, 22.4 mA cm^{-2} J_{SC}, 83.55% FF, and 21.28% PCE.[237] Such exciting prospects render hydrogenated $Cs_2AgBiBr_6$ a promising avenue for further research and device engineering studies. Furthermore, Tl-based halide elpasolites, namely $Cs_2AgTlCl_6$ and $Cs_2AgTlBr_6$, exhibit direct and tunable

bandgaps of 0.95 eV and 2.0 eV; they don't serve to fulfil the aim of low-toxicity PIMs as Tl is significantly more toxic than Pb.[222]

Alternatively, related silver-bismuth materials, such as Cu_2AgBiI_6 may have photovoltaic potential.[221,238–240] Cu_2AgBiI_6 possesses both octahedral and tetrahedral motifs.[51] This material has a high absorption coefficient of 1×10^{-5} cm^{-1}, and a reduced bandgap of 2.06 eV.[51] The highest performing Cu_2AgBiI_6 device used a hot casted active layer to improve film morphology and coverage, and exhibits a PCE of 2.45% in a FTO/c-TiO_2/m-$TiO_2/Cu_2AgBiI_6/Spiro$-OMeTAD/C device stack.[239]

Interestingly, the mono and trivalent B-sites in a double perovskite do not have to be occupied by two different elements, as two atoms of a single element with different oxidation states

**ADVANCED
SCIENCE NEWS**

www.advancedsciencenews.com

**ADVANCED
FUNCTIONAL
MATERIALS**

www.afm-journal.de

can be incorporated into a double perovskite lattice. For example, gold based ($A_2Au^+Au^{3+}X_6$) possesses direct bandgaps in the range of 1.2–1.4 eV, absorption coefficients up to 14×10^4 cm^{-1}, and high thermal stability.[241–243] However, despite the successful synthesis of several $A_2Au_2X_6$, (A = Cs, MA, Rb, X = Cl, Br, I) perovskites materials, only devices based upon MA_2AuBr_6 and MA_2AuI_6 have been manufactured.[241,243,244] These devices do demonstrate a photo-response, but unfortunately only a low performance, PCE $\approx$ 0.007%, $V_{OC} \approx$ 0.3 eV, is obtained due to a high prevalence of traps, with estimates placing the trap densities to be 3.35×10^{13} cm^{-3}.[222,244] Furthermore, these MA-based gold perovskite devices suffer from poor stability in the presence of moisture. Therefore, the conventional approach of swapping unstable MA for Cs to achieve an all-inorganic $Cs_2Au_2X_6$ (X = I, Br) perovskite has been investigated. Indeed, $Cs_2Au_2Br_6$ powders have been demonstrated to possess high stability in ambient conditions, in combination with a direct bandgap of 1.4 eV and low structural defects.[241] Additionally, $Cs_2Au_2I_6$ displays an improved bandgap of 1.31 eV, due to the introduction of an intermediate band between the conduction and valence band, resulting in simulated devices with PCE values of $\approx$20%.[243] Though presently these materials are yet to be translated into functional devices, as gold double perovskite devices are hindered by the difficulties encountered during synthesis and film processability, and more experimental efforts will be required before the potential of these materials can be fully assessed.

Similarly, $Cs_3Sb_2I_9$ has been proposed as an alternative perovskite photo-absorber, with the preferred 2D layered phase presenting a bandgap of 2.05 eV, and similar absorption coefficients to MAPbI$_3$.[102] Initial improvements have been made to the active layer in solution-processed devices through, vapor-assisted processes, HCl additives to reduce annealing temperature, and antisolvents to improve film morphology.[129,134] Figure 16b shows the improvement in the solar cell performance of $Cs_3Sb_2I_9$ by HCl treatment. Moreover, several investigations into suitable hole transport materials for $Cs_3Sb_2I_9$ devices have occurred, with the addition of P3HT as a hole transport layer reported to achieve record PCEs as high as 2.5% due to large V_{OC} and J_{SC} gains that result from the well-matched valence bands of $Cs_3Sb_2I_9$ and P3HT (−5.16 eV and −5.0 eV respectively).[133] Alternatively, investigations into active layer modification via halide and cation substitution have taken place.[245,246] $Cs_3Sb_2I_{9-x}Cl_x$ incorporates chloride to stabilize the 2D layered phase and tune the bandgap to 1.95 eV and has been reported to achieve device efficiencies of 2.22% under AM1.5G conditions. Presently $MA_3Sb_2I_{9-x}Cl_x$ possesses the highest PCE for any antimony-based perovskite to date, at 3.34%.[162]

5.1.2. Vacancy Ordered Perovskites

In lieu of a monovalent and trivalent B site substitution, it is possible to construct a perovskite framework using a $A_2B^{4+}\square X_6$ structure, where a single tetravalent metal and a vacancy are used. One motivation for the adoption of B^{4+} metals is that some common lead-free ABX$_3$ halide perovskites tend to readily oxidize to their B^{4+} state, i.e., Sn^{2+} rapidly becomes Sn^{4+}.[247] Therefore, tin-based vacancy-ordered perovskites of Cs_2SnI_6 have been explored

as a means of utilizing the stable Sn^{4+} in a PV active layer.[248] Reported to possess a bandgap of 1.25–1.62 eV, absorption coefficient $\approx$10^5 cm^{-1}, and excellent stabilities, Cs_2SnI_6 devices were first reported with a PCE of 1%,[248–250] which has since been further raised to 2.1%, via X-site halide modification to $Cs_2SnI_4Br_2$, and the mitigation of unreacted CsI impurities.[251] These limited efficiencies are likely due to high resistivity and the presence of defects, with large surface and bulk defect densities reported, mostly caused by Sn interstitials and iodine vacancies.[37,252] These iodine vacancies can however be mitigated through alteration in thin film processing such as iodine-rich environments, which have been shown to improve grain sizes, morphology, and PL intensity with an addition of 7% excess iodine (Figure 16c,d), but has yet to be applied to a device.[220] Interestingly Cs_2SnI_6 has also been utilized as an inorganic hole-transporting material in a solid-state dye sensitized solar cell, achieving a PCE of 7.6% PCE.[38] Here pristine Cs_2SnI_6 was reported to be an n-type semiconductor with an electron mobility of 310 cm^2 V^{-1} s^{-1}, however, upon SnI$_2$ doping, it will become p-type, with a hole mobility of 42 cm^2 V^{-1} s^{-1}, both with a carrier concentration of $\approx$1 $\times$ 10^{14} cm^{-3}.

To avoid the intrinsic setbacks encountered in Cs_2SnI_6 materials, a Ti^{4+} based perovskite: Cs_2TiBr_6 offers an alternative non-toxic, stable, and earth-abundant material system. Presently the only experimental device exhibits a bandgap of 1.8 eV, but still surpasses the performance of the lower bandgap Cs_2SnI_6, delivering an efficiency of 3.3%, with an impressive V_{OC} of 1.02 V.[109] This is achieved from a two-step vapor deposition process, resulting in an active layer with uniform and bright PL, and carrier lifetimes of $\approx$24 ns in a thin film (< 3.6 ns when adjacent to transport layers). However, the bandgap of Cs_2TiBr_6 is strongly affected by the method of synthesis, varying from 1.7 eV (indirect) to 2.3 eV (direct) for melt crystallization, solution, colloidal, and vapor deposition, with further variance for the chloride (1.82–3.4 eV) and iodide (1.02 eV) analogs, limiting the available methods of efficient device fabrication.[253] Therefore, presently no devices based upon solution processes have been reported. Furthermore, chlorobenzene can dissolve Cs_2TiBr_6 rendering Spiro-OMeTAD as an incompatible hole transport layer (HTL), and instead the device stack relies on P3HT as the HTL, which may benefit from further optimization in energy alignment and interfacial engineering for improved charge extraction. Consequently, a number of computational studies have designed device stacks with alternative transport layers (ETL: TiO$_2$, SnO$_2$, ZnO. HTL: Cu$_2$O, CuSCN, MoO$_3$), back contacts (Cu, Fe, Au, Ag, Nb, C), and active layer thicknesses (130–4330 nm), reporting various potential optimized efficiencies, up to 18.15%.[253,254] Alternatively, more theoretical studies have explored doping Cs_2TiBr_6 and Cs_2TiI_6 with other tetravalent metals such as Sn, Pb, or Zr, for example, $Cs_2Ti_{0.25}Sn_{0.75}Br_6$ exhibits a promising direct bandgap of 1.50 eV, corresponding to a theoretical efficiency of 22.13%.[255,256] However, functional devices based upon these simulation studies are yet to be reported.

Several other vacancy-ordered perovskites with appealing properties for solar cell applications have been reported, such as Cs_2PdBr_6, Cs_2TeI_6, and Rb_2SnI_6.[85,257–259] Even a mixed valence vacancy-ordered analog to double perovskites $A_4B^{3+}B^{5+}X_{12}$ that utilize a B-site trivalent and pentavalent metal to sum to the B^{4+} have been reported, such as $A_4Sb^{3+}Sb^{5+}X_{12}$, $A_4In^{3+}Sb^{5+}X_{12}$, and

**ADVANCED
SCIENCE NEWS**

www.advancedsciencenews.com

**ADVANCED
FUNCTIONAL
MATERIALS**

www.afm-journal.de

$A_4Bi^{3+}Sb^{5+}X_{12}$.[249,260,261] But none of these materials are yet to be implemented in functional devices.

Presently the literature for vacancy-ordered perovskite solar cells is dominated by theoretical and material-based studies and, therefore, while initial devices have demonstrated their potential, and many high-performing device stacks have been designed, further efforts in thin film deposition, and device engineering are required if such predicted device performances are to be realized.

5.1.3. Silver/Copper Pnictogen-Based halides

Maintaining the octahedral motif of perovskites, crystallized in an edge-sharing orientation, silver/copper pnictogen-based halides of the formula $A_aB_bX_x$ (A: Ag; B: Bi, Sb; X: I, Br) x = a+3b (as well as analogs containing Cu), have only recently demonstrated promise for photovoltaic applications.[48] Of these materials, Ag-Bi-I and Cu-Bi-I have been the subject of most attention for photovoltaic applications.

Unfortunately, Cu-Bi-I based materials have seen little photovoltaic progress, with the best reported device to date yielding a lackluster PCE of only 1.1%, with a low V_{OC} (0.38 V) and FF (29%), due to severe recombination.[262] However, Ag-Bi-I devices have reported PCEs rising from 1.22% to 5.44% in only a few years, and are thus more promising.[111,263] This is because Ag-Bi-I materials possess direct bandgaps within the range of 1.60–1.93 eV, good absorption coefficients of $\approx10^5$–10^6 cm^{-1}, and are compatible with multiple doping strategies.[140] While impressive, two main caveats prevent higher performances, first Ag-Bi-I materials are defect intolerant, with a tendency to form midband defects that result in short carrier lifetimes and significant charge carrier recombination.[48] Secondly, Ag-Bi-I films degrade in the presence of traditional hole transport layer (HTL) additives like Li-TFSI, t-BP, and acetonitrile, which has prevented the use of Spiro-OMeTAD in devices, limiting charge extraction.[264] Thus, optimization through device engineering, such as active layer deposition techniques that suppress defect formation, and alternative transport layers have been attempted.

Efforts to reduce defects via improvements in the film morphology of Ag-Bi-I active layers are numerous. AgI has poor solubility in DMSO and DMF, and so solvent engineering, such as the use of hot solvents or additives like aqueous HI, or Li-TFSI, have been shown to improve solubility and hence film morphology.[48,100,265,266] Antisolvents also are employed, such as chlorobenzene, toluene, diethyl-ether, chloroform, etc, and are shown to influence the charge generation efficiency, charge mobility, and carrier lifetime within Ag-Bi-I films.[100] Also, dynamic hot casting has been shown to promote pinhole-free, large-grained films with longer carrier lifetimes.[113] Ghosh et al. achieved a solar cell efficiency of $\approx2.5\%$ for dynamic hot-casted Ag-Bi-I (Figure 16e).[113] The dynamic hot casting method enhanced the carrier lifetimes of $AgBiI_4$ and Ag_2BiI_5 thin films from 23 and 83 ns to 75 and 133 ns, respectively (Figure 16f), which led to improved carrier transport in the corresponding photovoltaic devices.

Transport layer optimization within Ag-Bi-I devices has also been conducted. Indeed, utilizing a mesoporous TiO$_2$ ETL reduces the distance a charge carrier must diffuse to be extracted, and thus partly counteracts the short carrier lifetime of Ag-Bi-I.[140] While for HTLs, alternatives to Sprio-OMeTAD, such as polymer materials like PTAA, have been employed to effectively extract charge carriers.[48,113,267,268] Therefore, the present champion device based upon pure phase Ag-Bi-I achieved a PCE of 4.3% in a stack of FTO/c-m-TiO$_2$/Ag$_3$BiI$_6$/PTAA/Au, and is still significantly shy of the theoretical maximum PCE of 18%.[48] The observed low V_{OC} of 0.63 V indicates that voltage losses occur due to recombination, as indeed carrier lifetimes remain short ≈1 ns. Furthermore, organic ligand-based surface passivation strategies for Ag-Bi-I remain unexplored, and thus the use of a PTAA HTL may result in poor interfacial contact with the active layer, reflected in the relatively low FF of 64%. Perhaps some recent developments Spiro-OMeTAD doping strategies may offer a route for future Ag-Bi-I compatibility, as incompatible additives such as Li-TFSI, t-BP, and acetonitrile have been removed in lieu of pre-synthesized Spiro-OMeTAD$^{2\bullet+}$(TFSI$^-$)$_2$ radicals and a TBMP$^+$(TFSI$^-$) salt, with superior performance, and enhanced stability.[269]

Similar to perovskites, doping strategies can be employed to overcome intrinsic material drawbacks. Indeed, A-site cesium doping is shown to increase device FF and V_{OC}, via improvements in surface morphology while introducing Antimony at the B-site raises J_{SC} of devices due to modified bandgap and improved charge extraction.[270–272] X-site doping has also been conducted by either, halide substitution, which incorporates Bromide to tune the material bandgap, and optimize film quality, or sulfide modification to yield $Ag_aBi_bI_{a+3b-2x}S_x$.[111,273] Presently, sulfur-modified Ag-Bi-I materials hold the record for the highest efficiency of 5.44% from an FTO/c-m-TiO$_2$/Ag$_3$BiI$_{5.92}$S$_{0.04}$/PTAA/Au device stack. Sulfur anions were incorporated via a solution process, using a bismuth(III)tris(4-methylbenzodithioate) precursor additive in various materials ($AgBiI_4$, Ag_2BiI_5, Ag_3BiI_6, and $AgBi_2I_7$), resulting in increased absorption and bandgap contraction of ≈0.1 eV from an initial range of 1.84–1.89 eV, due to an upshift in the valence band. This means that small percentages of sulfur 1–4% result in an enhanced J_{SC}. But a reduction in V_{OC} and FF occurs due to interfacial issues caused by residual surface impurities likely from the organo-metal-sulfide additive used in film fabrication. Thus, alternative metal sulfide complexes or gas-assisted sulfurization processes may offer a way to incorporate higher sulfur percentages and preserve high film quality.

5.1.4. Metal Chalcohalides

Metal chalcohalides in a perovskite structure are also referred to as a split anion perovskite. Such materials aim to improve perovskite stability by introducing covalently bonded chalcogens, while also improving their optoelectronic properties.[17,274–276] Presently only a few chalcohalides have been reported as an active layer material and the reliability is a little ambiguous. Although a MASbSI$_2$-based solar cell with a device efficiency of 3.08% via a three-step process was reported, the composition of the absorbing layer has been debated; As the formation of MASbSI$_2$ is thermodynamically unfavorable under equilibrium conditions, the light-absorption layer could be a binary mix of Sb$_2$S$_3$ and MA$_3$Sb$_2$I$_9$.[58,277] Furthermore, MA$_3$Bi$_2$I$_{9-2x}$S$_x$ devices have also been reported, with a solid-state process yielding a PCE of 0.13%,

**ADVANCED
SCIENCE NEWS**

www.advancedsciencenews.com

**ADVANCED
FUNCTIONAL
MATERIALS**

www.afm-journal.de

but significant Bi_2S_3 phases remaining present in the final film, while another low-pressure vapor-assisted method yielded a pure phase material with a PCE of 0.152%.[278,279]

Alternative chalcohalide materials typically rely on the pnictogens of BiSI and SbSI which have achieved respective PCEs of 1.32% and 3.62%.[117,280] Presently BiSI (1.51 eV) development has been limited by the propensity to form 4 ternary and over 15 binary undesired phases during synthesis, leading to film impurities.[281] Only thermolysis procedures have succeeded in the fabrication of phase pure, yet flakey polycrystalline films, which are thus inhibited by bulk defects and short carrier lifetimes ≈1 ns.[117] Comparatively, SbSI (1.83 eV) is easy to synthesize, and uniform-phase pure films have been used in devices. Indeed, in addition to a solution phase synthesis, SbI vapor has also been demonstrated to uniformly modify thick Sb_2S_3 films, to obtain either SbSI (PCE = 3.62%), or layered Sb_2S_3-SbSI (PCE = 6.08%) devices. Furthermore, architecture plays an important role in charge extraction, indeed it is important to achieve intimate contact between the SbSI active layer and the HTL, for example a penetrative PCPDTBT layer beneath PEDOT:PSS, in combination with a m-TiO_2 ETL has been demonstrated to improve charge extraction before recombination can occur.[142]

Presently a mixture of antimony and bismuth, $Sb_{0.67}Bi_{0.33}SI$, prepared by treating Sb_2S_3 films with BiI via chemical bath deposition, possesses the highest PCE reported of all chalcohalides at 4.07%.[56] It purports a bandgap of 1.62 eV, midway between that of SbSI and BiSI, without suffering phase impurities and poor film quality found in BiSI-based devices. The device demonstrates improved J_{SC} relative to Bi-free SbSI devices, and high environmental stability. However again this film relies on a penetrative HTM of PCPDTBT/PEDOT:PSS to suppress recombination at the m-TiO_2 active layer interface, and efficiently extract electrons and holes. A quaternary chalcohalide, $Sn_2SbS_2I_3$, is a promising solar cell absorber with a bandgap of 1.41 eV, resulting in a PCE of 4.04%.[282] Unencapsulated $Sn_2SbS_2I_3$ devices demonstrated excellent stability in the air, under moisture and continuous light illumination.

Presently chalcohalide materials are limited by either the need for challenging non-equilibrium conditions to prevent phase segregation during synthesis, or complex architectures to inhibit rapid charge recombination. Through further theoretical and experimental research into thin film synthesis/deposition techniques, and compatible materials for planar device architectures, chalcohalides may experience further PV success.

5.1.5. Chalcogenides

It is possible for perovskite-inspired materials to explore beyond the halide motif, and investigate chalcogenides. These materials offer the potential for improved material stability, due to the covalently bonded nature of chalcogenide materials, and various promising optoelectronic properties. $AgBiS_2$ is one such stand out material that has achieved rapid progress, with PCEs rising from 0.53% to 9.17% in only 9 years.[53,283] These improvements have been achieved via synthesis, and device engineering strategies such as, enhanced absorption coefficients from in-

creased cation disorder, optimized nanocrystal passivation from organic ligands, and improved energy alignment with the selected HTL.[53,284]

An alternative class of promising chalcogenide materials are the chalcogenide perovskites, analogous to the naturally occurring perovskite namesake- $CaTiO_3$, oxygen is substituted for less electronegative chalcogens such as sulfur or selenium.[285] This reduces the wide-bandgap that oxide perovskites are known for, improving photovoltaic viability.[286,287] A mix of simulation and material synthesis studies have determined $BaZrS_3$ as a frontrunning photovoltaic material, with a moderate bandgap of ≈1.7–1.9 eV, high absorption coefficient ≈10^5 cm^{-1}, defect tolerance, dopability (6% Ti^{4+} shifts the bandgap to 1.4 eV), high carrier mobilities, and extreme thermal and moisture stability.[89,90,288–291]

Crucially however, functional solar devices are yet to be fabricated, as the high temperature sulfurization steps that are required to synthesize these chalcogenide perovskites are destructive to the underlying transport layers and substrates in a device stack.[292] Therefore, attempts to reduce these fabrication temperatures are of the upmost importance. Indeed, PLD methods have reported a reduction from 1100 °C to 500 °C, while a number of breakthroughs in ligand-based solution synthesis have also obtained coarse films as low as 500 °C, and colloids at just 330 °C.[293–299] Presently, further research into film deposition techniques, or thermally resistant transport layers, are required before a functional chalcogenide perovskite solar cell may be realized.

5.2. Indoor Photovoltaics (IPVs)

There is a rapid rise in the demand for self-powered, indoor-located Internet of Things (IoT) nodes, with an estimated installation of billions of wireless sensors in the next ten years.[300] Indoor photovoltaics (IPVs) would be promising for supplying reliable power and enabling uninterrupted communication in the IoT ecosystem due to their ability to harvest indoor light (artificial illumination from white light-emitting diodes (WLEDs), compact fluorescent light (CFL), and halogen bulbs as shown in **Figure 17**a). Hydrogenated amorphous silicon (a-Si:H) is the industrial standard for IPVs, with indoor PCE (PCE(i)) values of 4–9%.[300–301] The spectral range (≈400−800 nm) of different indoor light sources differs from that of 1-Sun, allowing the absorbers with bandgaps in the 1.8−2.0 eV range ideal for IPVs. Peng et al. introduced indoor spectroscopically limited maximum efficiency (i-SLME) method and estimated that a maximum theoretical PCE(i) (radiative limit) of ≈60% can be achieved for absorbers with bandgaps around 1.9 eV under WLED and FL illuminations (Figure 17b).[302] The i-SLME assumes negligible non-radiative recombination and considers the absorption coefficient, bandgap nature (direct or indirect), and fixed thickness (500 nm) for the absorber layer. LHPs are the finest candidates for IPVs in terms of efficiency compared to the other emerging IPV technologies, such as dye-sensitized and organic PVs, with record PCE(i) of ≈40% and a corresponding V_{OC} greater than 1 V arising majorly from their defect-tolerant nature.[303–305] By contrast, high concentration of defects and the related non-radiative recombination in wide-bandgap (E_g = 1.8−2.0 eV), air-stable antimony (III) (Sb^{3+})- and bismuth (III) (Bi^{3+})-based PIMs has led to
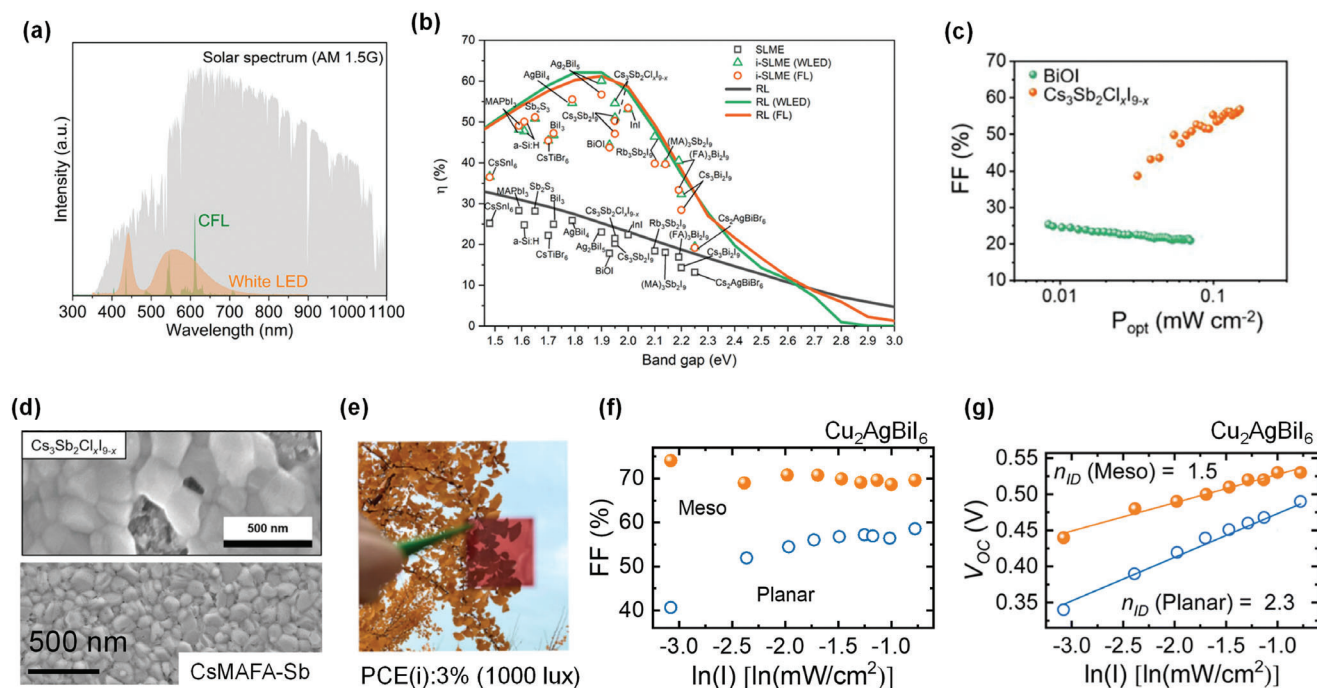
Figure 17. a) 1-Sun spectrum and emission spectra of CFL (color temperature: 3000 K) and WLED (color temperature: 5000 K). Reproduced with permission.[303] Copyright 2022, American Chemical Society. b) SLME, *i*-SLME, and radiative limits of the photovoltaic efficiencies of various Bi/Sb-PIMs under 1-Sun (AM 1.5G) and indoor (FL and WLED) illuminations. Both MAPbI$_3$ and a-Si:H are involved for the comparison. c) Variation of FF with indoor light intensity for the Sb-PIM and BiOI. b,c) The SEM image (top) in d) are reproduced under the terms of the CC-BY licence.[302] Copyright 2020, The Authors, published by Wiley-VCH. d) SEM images of Cs$_3$Sb$_2$Cl$_x$I$_{9-x}$ (top) and CsMAFA-Sb (bottom). The SEM image at the bottom is reproduced under the terms of the CC-BY licence.[163] Copyright 2022, The Authors, published by Wiley-VCH. e) Transparent Ag$_2$BiI$_5$ absorber layer that delivered a PCE(i) of 3% under 1000 lux WLED illumination. Reproduced with permission.[309] Copyright 2023, American Chemical Society. Variation of f) FF and g) with WLED light intensity for mesoscopic and planar Cu$_2$AgBiI$_6$ photovoltaic devices. Reported under the terms of a Creative Commons Attribution 3.0 Unported Licence.[221] Copyright 2023, The Royal Society of Chemistry.

modest PCE(i)s (**Table 4**) despite their suitability for IPVs from the bandgap point of view.[300,302]

5.2.1. Sb-Based PIMs

Peng et al. conducted the first-ever investigation in 2021 on the indoor performance of Cs$_3$Sb$_2$Cl$_x$I$_{9-x}$ PIM, which possesses an optimal bandgap of ≈1.9 eV. They found that the PCE of the fully inorganic Sb-PIM increased from 1% (under 1-Sun) to 5% under WLED and FL illuminations.[302] The authors demonstrated that Cs$_3$Sb$_2$Cl$_x$I$_{9-x}$ IPV devices could deliver sufficient power required for printed thin-film transistor (TFT) circuits.[302] The indoor PCE (PCE(i)) of the freshly made Cs$_3$Sb$_2$Cl$_x$I$_{9-x}$ cells was around 2%, which rose to the reported 5% during the five months of storage in an N$_2$-filled atmosphere. The corresponding V_{OC} of 0.49 V suggests the devices incurred huge V_{OC} losses; an absorber with a bandgap of 1.9–2.0 eV can achieve V_{OC} as high as ≈1.4 eV under 1000 lux, as predicted by Ho et al.[306] The indoor light intensity dependencies (10–200 μW cm^{-2}) of V_{OC}, J_{SC}, and FF were conducted to understand the major IPV device performance degradation pathways of Cs$_3$Sb$_2$Cl$_x$I$_{9-x}$. The semi-log plot of V_{OC} vs light intensity results in a slope of n$_{ID}$k$_B$T/q, where n$_{ID}$ is the idicality factor and k$_B$, T, and q are Boltzmann's constant (= 1.38 × 10^{-23} J K^{-1}), temperature (= 293 K), and elementary charge (= 1.6 × 10^{-19} J), respectively. The n$_{ID}$ value of ≈2

for the Cs$_3$Sb$_2$Cl$_x$I$_{9-x}$ IPV devices suggested that the majority of the photoexcited carriers undergo Shockley-Read-Hall (SRH)-type trap-assisted recombination via mid-gap states in the absorber layer,[306] consistent with the PL QY of 0.1% (i.e., ≈99.9% of recombination is non-radiative). The FF of the devices significantly reduced at lower light intensities (Figure 17c), and J_{SC} exhibited a linear trend with the light intensity, which further verified the predominant mid-gap state-mediated defect-assisted recombination.[264,307] It was anticipated that the discontinuous morphology and the pin-holes in the Cs$_3$Sb$_2$Cl$_x$I$_{9-x}$ layers (Figure 17d) created shunt pathways and contributed to many recombination centers in the device.[302]

A triple cation Sb-PIM, CsMAFA-Sb (elemental composition: Cs$_{2.4}$MA$_{0.5}$FA$_{0.1}$Sb$_2$I$_{8.5}$Cl$_{0.5}$), obtained by cation mixing involving Cs, methylammonium (MA), and formamidinium (FA) cations in the A-site delivered an improved PCE(i) of 6.37% at 1000 lux illumination,[310] placing it within the PCE(i) range of amorphous silicon.[300,301] In contrast to Cs$_3$Sb$_2$Cl$_x$I$_{9-x}$,[302] 2D CsMAFA-Sb demonstrated dense and uniform film morphology with a grain size of ≈250 nm (Figure 17d). This led to low dark current, reduced defect density, and non-radiative recombination in CsMAFA-Sb devices compared to corresponding double-cation counterparts (CsMA- and CsFA-Sb), and possibly even Cs$_3$Sb$_2$Cl$_x$I$_{9-x}$. This reveals the importance of mixing inorganic and organic cations in the A-site to reduce recombination losses and improve charge carrier extraction (peak EQE = 77%), which

**ADVANCED
SCIENCE NEWS**

www.advancedsciencenews.com

**ADVANCED
FUNCTIONAL
MATERIALS**

www.afm-journal.de

Table 4. Performance of state-of-the-art PIM-based IPVs at 1000 lux illumination.

Active layer (PIM)	Bandgap (eV)/type	Device structure	Light source	PCE(i) [%]	FF	J_{sc} [µA cm^{-2}]	V_{oc} [V]	Ref.
$Cs_3Sb_2[Cl_xI_{9-x}]$	1.95/ near-direct	FTO/TiO$_2$/m-TiO$_2$ (Cs$_3$Sb$_2$Cl$_x$I$_{9-x)}$/Poly-TPD/Au	WLED	4.4	0.40	76	0.47	[302]
			FL	4.9	0.42	82	0.49	
BiOI	1.93/ indirect	ITO/NiO$_x$/BiOI/ZnO/Cr/Ag	WLED	4.0	0.38	56	0.60	[302]
			FL	4.4	0.40	62	0.60	
AgBiI$_4$	1.8/ direct	FTO/c-TiO$_2$/AgBiI$_4$/spiro-OMeTAD/Au	WLED	5.17	0.56	5.7	0.55	[308]
Ag$_2$BiI$_5$	1.89/ direct	ITO/SnO$_2$−SnO$_x$/ABI/PTAA/Au	WLED	5.02	0.48	39.1	0.70	[309]
ATBiI$_4$ (AT = 2-aminothiazolium)	1.78	FTO/c-TiO$_2$/ATBiI$_4$/PTAA/Ag	WLED	0.52	0.50	4.35	0.71	[157]
Cs$_{2.4}$MA$_{0.5}$FA$_{0.1}$Sb$_2$I$_{8.5}$Cl$_{0.5}$	2.1 /direct	FTO/c-TiO$_2$/ Cs$_{2.4}$MA$_{0.5}$FA$_{0.1}$Sb$_2$I$_{8.5}$Cl$_{0.5}$/P3HT/Au	WLED	6.37	0.61	106.7	0.55	[163]
Cu$_2$AgBiI$_6$ +HI	1.94 /direct	FTO/c-TiO$_2$/ Cu$_2$AgBiI$_6$+HI/Spiro-OMeTAD/Au	WLED	4.7	0.65	80	0.60	[238]
Cu$_2$AgBiI$_6$	1.91 /direct	FTO/c-TiO$_2$/m-TiO$_2$/ Cu$_2$AgBiI$_6$/Spiro-OMeTAD/Au	WLED	5.52	0.67	72	0.53	[221]

enhanced the IPV device performance of an Sb-PIM. The maximum V_{OC} of 0.6 V obtained from CsMAFA-Sb devices was higher than that was achieved for fully inorganic Sb-PIM (V_{OC} = 0.49 V). The decrease in V_{OC} under indoor light was estimated using the following relation:[311]

$$\Delta V_{OC} = \frac{n_{ID}k_B\ T}{q}\ \ln \frac{I_{1-Sun}}{I_{WLED}} \qquad (1)$$

In the case of only radiative recombination (n_{ID} = 1), V_{OC} loss (ΔV_{OC}) at 1000 lux was estimated using the above expression to be 0.14 V at 1000 lux, which was lower than the value (0.20 V) obtained experimentally because of dominant non-radiative recombination in CsMAFA-Sb ($n_{ID} \approx 2$). However, a reduction in V_{OC} in the 0.12−0.24 V range occurs for many IPV technologies, including LHPs.[303] Furthermore, transient absorption-based study on charge carrier dynamics at the device interfaces indicated in CsMAFA-Sb, the hole transfer process dominates the interfacial charge recombination process,[163] as also observed in LHPs.[312] A moderate charge carrier mobility of CsMAFA-Sb of ≈12 cm^2 V^{-1} s^{-1}, comparable to other PIMs such as halide elpasolites, silver iodobismuthates, and Cu$_2$AgBiI$_6$, could be improved by optimizing the fabrication conditions.[163] Another IPV study on Sb-PIM involved Cs$_3$Sb$_2$I$_9$/ITIC heterostructure-based photovoltaic cells, which delivered a PCE(i) of 9.2% at 1000 lux.[313] It should be noted here that the organic photovoltaic devices based on ITIC delivered a PCE(i) of 15–18% (1000 lux).[314] Thus, the demonstrated PCE(i) of 9.2% of Cs$_3$Sb$_2$I$_9$/ITIC IPVs does not indicate an improvement in the performance of the Sb-PIM.

5.2.2. Bi-Based PIMs

Bismuth oxyiodide (BiOI) is one of the wide-bandgap PIMs that is characterized by shallow traps and high defect tolerance.[80,82] Nevertheless, only a modest PCE(i) of ≈4% (increased from 2.4% to 4% in 5 months in an N$_2$ environment) and a corresponding V_{OC} of 0.6 V was demonstrated for BiOI under 1000

lux fluorescent light.[302] A notable observation about this system is its increasing FF trend with decreasing indoor light intensities (Figure 17c), indicating its aptness for low-light intensity applications.[302] However, a low absorption coefficient of 10^4 cm^{-1} limits the i-SLME PCE(i) value of BiOI to 44%.[302] The IPV performance of another Bi-based PIM family, Ag-Bi-I materials, was first studied by Turkevych et al., who reported a PCE(i) of 5.17% and V_{OC} of 0.55 V at 1000 lux for AgBiI$_4$-based photovoltaic cells.[315] The corresponding output power of 1.76 µW cm^{-2} might be only sufficient to power low-power wireless data transmitters that consume energy as low as 1 µJ per bit.[316] Arivazhagan et al. achieved a high V_{OC} of 0.71 V at 1000 lux by replacing Ag$^+$ in AgBiI$_4$ with a 2-aminothiazolium cation. The high built-in potential and reduced interfacial charge accumulation were attributed to the enhancement in the V_{OC} but the corresponding PCE(i) was limited to 0.54%.[157] On the other hand, very recently, Guerrero et al. demonstrated a V_{OC} of 0.7 V and a PCE(i) of 5% (and 3% for a semitransparent cell) at 1000 lux for Ag$_2$BiI$_5$ IPVs (Figure 17e).[309] In this study, the authors realized the importance of low bimolecular (influences J_{SC}) and trap-assisted (affects V_{OC}) recombination in achieving improved performance for the Ag$_2$BiI$_5$-based photovoltaic devices. The PCE of the AgBiI$_4$ and Ag$_2$BiI$_5$ devices cells was only around 1–2% under 1-Sun illumination,[309,308] whereas Ag$_3$BiI$_6$ demonstrated higher PCE values of 5–6% under 1-Sun,[111] which may guarantee PCE(i) values greater than the existing 5%. Only one report exists on IPVs based on halide elpasolites. Cs$_2$AgBiBr$_6$/D149 indoline dye-based (with or without Ti$_3$C$_2$T$_x$ MXene) IPV cells demonstrated PCE(i) ≈7% at 1000 lux.[226] However, this system also falls into the same category as the Cs$_3$Sb$_2$I$_9$/ITIC heterostructure[313] because the indoline dye also contributes to the observed photocurrent of the cells.[226] Thus, Cs$_2$AgBiBr$_6$ may have yet unrealized potential for IPVs.

The quaternary Cu$_2$AgBiI$_6$ with a bandgap of ≈1.9–2.0 eV has been explored for IPVs, owing to the excellent match between its absorption (or EQE) profile and WLED emission spectrum.[221,238] Grandhi et al. demonstrated a PCE(i)

of 4.7% and V_{OC} of 0.6 V Cu_2AgBiI_6 devices in their planar architecture through an enhanced microstructure of the Cu_2AgBiI_6 absorber layer by hydroiodic acid (HI) additive.[238] Despite the additive engineering, the morphology of the Cu_2AgBiI_6 layer remained moderate, with a large room for improvement. Pai et al. showed an improved morphology and surface coverage of the Cu_2AgBiI_6 film on mesoporous TiO_2 by modifying processing conditions.[239] In addition, mesoporous ETL in the mesoscopic PIM-based devices allows enhanced charge extraction and suppresses the $J–V$ hysteresis, unlike the case of their planar counterparts.[51,162,221,239,195] Mesoscopic Cu_2AgBiI_6 devices delivered an improved PCE(i) of 5.52% under 1000 lux WLED illumination.[221] Furthermore, the typical illuminance levels in indoor environments are 200–700 lux.[318] High shunt resistance is desirable to prevent the leakage of photogenerated current under low illumination conditions,[319] as observed in the case of Cu_2AgBiI_6[221] (and CsMAFA-Sb[163]), which ensured a minimal loss in FF upon decreasing the light intensity (Figure 17f). As a result, mesoscopic Cu_2AgBiI_6 devices delivered a PCE(i) of 4.64% at 200 lux and a V_{OC} of 0.38 V at 50 lux.[221] The mesoscopic devices registered a lower n_{ID} value of 1.5 compared to the Cu_2AgBiI_6 planar devices (n_{ID} = 2.3), suggesting a decreased trap-assisted (SRH-type) recombination under open-circuit conditions (Figure 17g). The same conclusion was deduced for the short-circuit conditions from the log-log plots of J_{SC} versus light intensity.[221] The reduced non-radiative recombination combined with the superior charge extraction by the mesoscopic architecture was attributed to the stable performance of the Cu_2AgBiI_6 devices at varying indoor light intensities. The estimated (see Equation (1)) V_{OC} loss (ΔV_{OC}) of 0.14 V of the best Cu_2AgBiI_6-based devices under radiative recombination assumption closely matched the corresponding experimental value of 0.13 V. Although the minimized V_{OC} loss of Bi/Sb-PIMs due to intensity reduction by two orders of magnitude (from 1-Sun to WLED) is commendable,[221,309,310] the actual V_{OC} value approached only ≈0.6–0.7 V. This, in turn, implies a large room to enhance the V_{OC} and advance the PCE(i) of Cu_2AgBiI_6-based (and other PIM-based) IPV devices towards their theoretical limit.

5.3. Photovoltaic Performance of Bi/Sb-PIMs versus Theoretical Limits

Cucco et al. predicted the spectroscopic limited maximum efficiency (SLME) limits to the solar cell performance of Bi-based PIMs, namely $Cs_2AgBiBr_6$, $AgBiI_4$, and Ag_3BiI_6 (**Figure 18**a,b).[320] $Cs_2AgBiBr_6$ experimentally delivered ≈40% (3.11%[225]) of the PCE with respect to its SLME value of ≈7%. This low SLME is a consequence of its indirect bandgap nature of the material that was considered in the SLME calculations.[321] On the other hand, the direct bandgap nature of hypothetical absorbers, namely $Cs_2TlBiCl_6$ and $Cs_2TlBiBr_6$ can deliver PCEs in the 16–18% range.[322] Furthermore, Ag_3BiI_6 solar cells achieved PCE of ≈4%,[111] which is only 26% of its SLME, because the experimental J_{SC} and V_{OC} reached only 60% and 43% of their corresponding SLME values.[320] Rondiya et al. compared the solar cell performance of several Bi-PIMs, including BiSI, to their radiative limits.[69] The PCEs of all these PIMs were found to be ≤ 25% the

theoretical limit due to the corresponding J_{SC} and V_{OC} values being below 75% and 50% of their radiative limits, respectively.[69] BiSI also exhibited low PCEs, i.e., less than 50% of its theoretical limit, due to low FF (poor thin film morphology) and strong J_{SC} and V_{OC} losses.[323]

Ag-Bi-I-based IPV devices delivered V_{OC} of 0.55–0.70 V and maximum J_{SC} of 40 μA cm^{-2} (at 1000 lux WLED illumination),[309,308] which correspond to only ≈40–50% and ≈30% of their i-SLME values, respectively (Figure 18c).[302] Sb-based PIM IPV devices also demonstrated ≈40–45% V_{OC} losses in the i-SLME limit.[302] These huge J_{SC} losses and V_{OC} deficits up to a few hundred meVs mainly occur due to carrier–phonon coupling, high Urbach energies, and trap densities and lead to lower PCEs (under both 1-Sun and indoor illuminations) for Sb/Bi-PIMs compared to their theoretical limits.[69,99,181,302,320]

5.4. Urbach Energy and V_{OC} Losses

In LHPs, the sub-bandgap features of the absorption spectra typically consist of 1) a region related to deep trap states with amplitudes several orders of magnitude lower than the absorption onset, and 2) the exponential tail region, where the absorbance decreases exponentially with decreasing energy (E), given by the following relation:[324] $\alpha \ (E, \ T) \propto \frac{E - E_0(T)}{E_U \ (T)}$ where α, T, and E_0 represent the absorption coefficient, temperature, and bandgap onset energy, respectively. E_U denotes the steepness of the absorption onset and is known as Urbach energy, which energy typically increases with the temperature due to carrier-phonon coupling.[324] Photothermal deflection spectroscopy (PDS) has been employed to obtain the absorption coefficient (α) spectra, in turn, extracting E_U values.[125,325] Ultrasensitive EQE measurements (sensitivities in the range of 10^{-10}) were recently proposed to differentiate between the exponentially decaying Urbach tails and the sub-bandgap features contributed by deep trap states, in turn, determining the E_U values accurately within an uncertainty of 1 meV (**Figure 19**a).[324,326] Another advantage of the EQE-based measurements is the negligible influence of the strongly bound excitons on the extracted E_U values. Furthermore, unlike conventional semiconductors, the disorder in LHPs changes from static to dynamic as temperature increases, accompanied by an increase in the mobility of photogenerated charge carriers, which can reach deep trapping centers.[327] The static disorder (the temperature-independent contribution to the Urbach energy) in LHPs has been found to be solely dominated by zero-point phonon energy rather than defect-induced structural disorder.[324] The remarkably lower static disorder values of LHPs in the 3.3–5.1 meV range, as determined by Zeiske et al.,[324] are comparable to or lower than those of crystalline Si and GaN semiconductors.

Higher E_U values typically lead to high dark currents and hence high V_{OC} losses.[69,325] The lower E_U (≈15 meV)[125] values of high-quality LHP thin films compared to thermal energy at room temperature (≈25 meV) minimize the V_{OC} losses and ensure excellent electronic properties. In addition to expressing the degree of energetic disorder, Urbach energy indicates the electronic quality (charge carrier lifetime, mobility, and diffusion lengths) of thin films of solar absorbers.[324,328] In their study on the correlation between Urbach energy and V_{OC} deficit, Subedi et al.
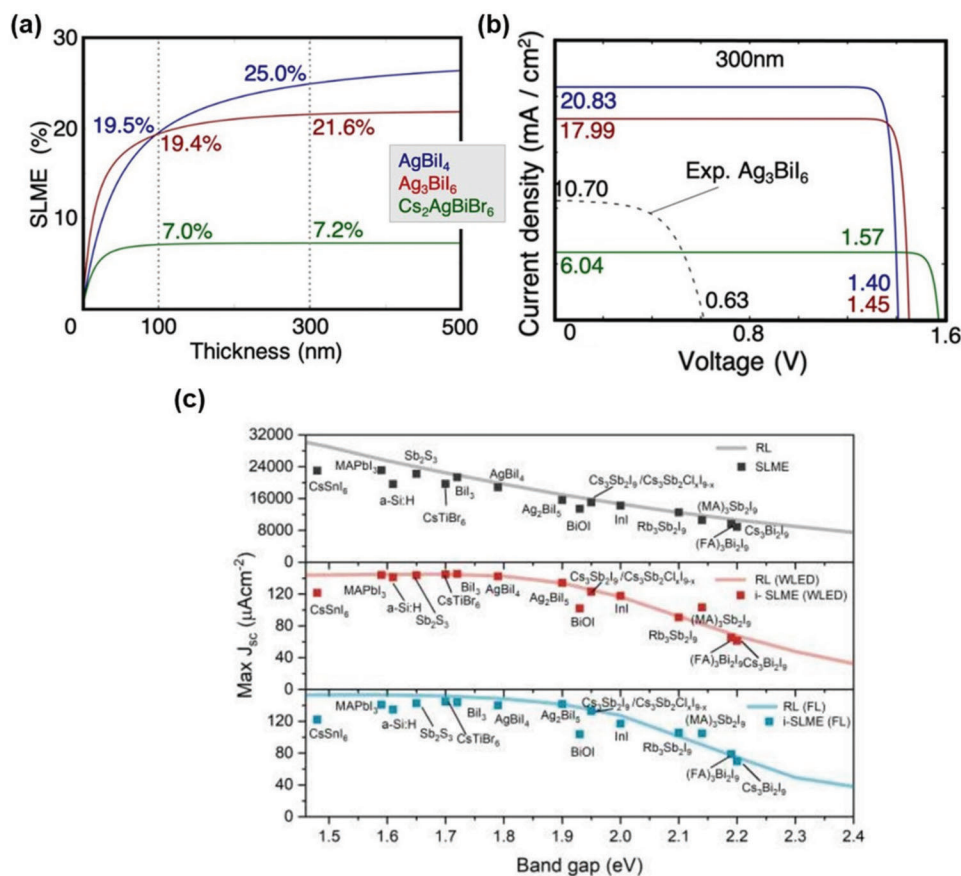
**ADVANCED
SCIENCE NEWS**

www.advancedsciencenews.com

**ADVANCED
FUNCTIONAL
MATERIALS**

www.afm-journal.de

Figure 18. a) SLME for $Cs_2AgBiBr_6$, $AgBiI_4$, and Ag_3BiI_6 as a function of the thin-film thickness. b) SLME calculated J–V curves for 300 nm absorber layer thickness. The dashed curve represents the experimental J–V curve of a Ag_3BiI_6 solar cell.[48] Panels (a) and (b) are reproduced with permission.[320] Copyright 2022, Wiley-VCH. c) Calculated J_{SC} in the SLME and i-SLME (for FL and WLED light sources) limits for various Bi/Sb-PIMs. Reproduced under the terms of the CC-BY licence.[302] Copyright 2020, The Authors, published by Wiley-VCH.

observed the E_U values in the 18–65 meV range for various mixed anion-cation perovskite compositions, which possess comparable bandgaps.[325] The authors attributed this large variation in E_U to the difference in the optoelectronic quality of the perovskite films (such as grain size, grain boundary passivation, and continuity of the grains). The E_U values of PIMs are typically higher (in the range or greater than 60 meV) than LHPs due to high structural disorder, high concentration of defects, and suboptimal film morphologies.[104,112] We note that the information regarding the energetic disorder of the Bi/Sb-PIMs has not been extensively reported in the literature. Hebig and coworkers showed that the Urbach tail energies of Cs, MA, and FA-based Bi/Sb-PIMs lie in the 57–69 meV, and these tail states served as non-radiative recombination channels and contributed towards V_{OC} losses of these PIM-based solar cells.[329] Bi-based PIMs such as $Cs_3Bi_2I_9$ (X = Cl, Br, I) demonstrate a high structural disorder compared to LHPs, as verified by the high Urbach energies ≈60–95 meV of single crystals of $Cs_3Bi_2X_9$ (X = Cl, Br, I).[330] A large amount of vacancies for the mobile ions (i.e., high structural disorder) in the crystals of $Cs_3Bi_2X_9$ introduce many sub-bandgap states in their band structure (Figure 19b). Lower structural disorder of the 2D (layered) form (E_U = 134 meV) of $Cs_3Sb_2I_9$ compared to the 0D (dimer) one (E_U = 162 meV) was verified by its lower Ur-

bach energy value,[134] which might contribute to the lower trap density in the 2D $Cs_3Sb_2I_9$ than the 0D one.[129] Single crystals of $Cs_2AgBiCl_6$ and $Cs_2AgBiBr_6$ demonstrated a high level of energy disorder with the corresponding E_U values of 95 and 170 meV,[94] attributed to the Ag_{Bi} antisite defects or Ag vacancies (shallow acceptors).[93] On the other hand, Bi vacancies (as well as bromide interstitials) contribute to deep traps in $Cs_2AgBiBr_6$,[93] and hence synthesis under Br-poor conditions may maximize its photovoltaic performance. A following study on a thin film sample of $Cs_2AgBiBr_6$ revealed a lower Urbach energy of 70 meV, which is still a large value to cause additional non-radiative trapping of the photoexcited carriers and hamper the V_{OC}.[99] Sb alloying into the Bi sites of $Cs_2AgBiBr_6$ has been proposed as an efficient approach for reducing its bandgap with anticipation of improved solar cell performance. In addition to lowering the bandgap, Sb incorporation resulted in the elevation of sub-bandgap absorption (hence high Urbach energy; see Figure 19c) and, importantly, it introduced a defect state at 1.55 eV, i.e., 0.7 eV below the bandgap of $Cs_2AgBiBr_6$. The authors accounted for the V_{OC} deficit of 0.7 V in the Sb-alloyed $Cs_2AgBiBr_6$ solar cells to the non-radiative relaxation of the photoexcited carriers into this additional defect state.[92] The authors further performed post-annealing of the Sb-alloyed $Cs_2AgBiBr_6$ samples to mitigate the sub-bandgap state
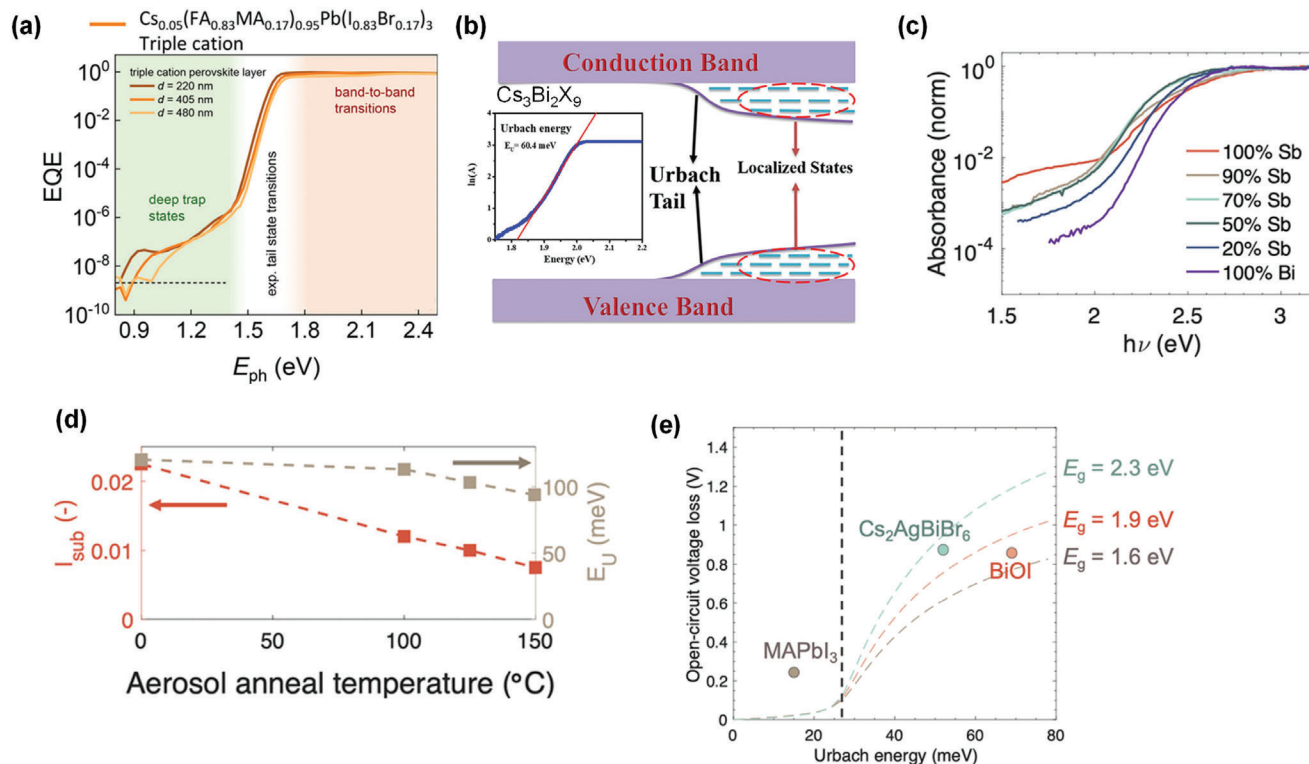
Figure 19. a) EQE spectra of LHP solar cells with different absorber layer thicknesses. The horizontal dashed line denotes the EQE noise floor. Reproduced with permission from Ref. [324] Copyright 2022, American Chemical Society. b) Reproduced with permission.[330] Copyright 2020, American Chemical Society. c) Absorption spectra of $Cs_2AgSb_xBi_{1-x}Br_6$. d) Variation of integrated sub-bandgap state intensity (I_{sub}) and Urbach energy (E_U) of the absorption edge with Aerosol annealing temperature. Panels (c) and (d) are reproduced under the terms of the CC-BY license.[92] Copyright 2022, The Authors, published by Wiley-VCH. e) V_{OC} deficit versus reported Urbach energy compared against the theoretical V_{OC} loss for different bandgaps (E_g), considering the non-radiative losses are primarily due to the Urbach energy. Reproduced under the terms of the CC-BY license.[69] Copyright 2021, AIP publishing.

formation as well as lower the strain. As shown in Figure 19d, the Urbach energy decreased from 120 to 94 meV because of annealing at 150 °C. In addition, the integrated sub-bandgap state intensity gradually decreased with the annealing temperature.[92] By contrast, Sb alloying caused a reasonable reduction in the energetic distribution of sub-bandgap trap states in Cu_2AgBiI_6. This contributed to the positive influence of Sb incorporation on the photovoltaic performance of Cu_2AgBiI_6.[317] Furthermore, the known energy disorder in the BiOI absorber with the corresponding E_U values of 70–90 meV leads to V_{OC} losses due to recombination from the band tail states.[82] Rondiya et al. obtained the correlation between the V_{OC} loss and the published Urbach energy values in the case of $Cs_2AgBiBr_6$ and BiOI.[69] It is evident from Figure 19e that the V_{OC} deficit in the solar cells of these two Bi-PIMs is majorly due to their high Urbach energies. A high degree of structural disorder has been noticed in metal chalcohalides, such as $Sn_2SbS_2I_3$ (E_g = 1.41 eV), with a very high E_U value of ≈464 meV.[282] High trap density in this material led to a low V_{OC} of 0.44 V due to large V_{OC} losses.

Future efforts may improve the microstructure and other thin film properties of these materials to mitigate the Urbach tail state-induced V_{OC} deficit in the corresponding optoelectronic devices. Alternatively, improved cation order has been proposed to reduce the Urbach energy and hence defect concentration in $Cs_2AgBiBr_6$.[331] A lowered cation disorder can also

hinder STE formation and improve charge carrier transport in $Cs_2AgBiBr_6$.[331] Engineering the cation disorder has played a significant role in achieving a substantially enhanced PCE of ≈9.2% for $AgBiS_2$ nanocrystal-based solar cells.[53] An increased homogeneity of cation disorder lowered the Urbach energy from 173 to 26 meV and contributed towards reducing the V_{OC} deficit of the $AgBiS_2$ devices by 80 meV. Finally, it's interesting to note that the high defect-tolerant potential photovoltaic absorbers like $BaZrS_3$ exhibit E_U values comparable to the room temperature thermal energy of 25 meV (22–28 meV).[332]

6. Self-Powered Photodetectors

The development of operationally stable and flexible self-powered photodetectors (SPPDs) with a multifunctional design will benefit daily life and society's well-being in the future.[188,217,333–335] The flexible SPPDs that can be twisted, bent, stretched, folded, and operated at zero bias have unique applications in wearable electronics,[334–336] encrypted communication,[337] sensory skins, smartphones, implantable biomedical devices,[335] and healthcare,[338] which cannot be achieved with the existing technology on rigid substrates.[335] The SPPDs have been fabricated with *n-i-p* or *p-i-n* based photovoltaic devices,[338,339] heterojunction,[191,203,340] Schottky junction,[40,341,342] asymmetric metal electrodes based devices,[201,343] and

photodetectors with externally intergraded powered generators[344–347] (nanogenerator (triboelectric, or piezoelectric), and pyro-phototronic). This section deals with the use of lead-free PIMs as photoactive layers for SPPDs. The photodetection properties (PDPs), such as photoresponsivity (R_{ph}), specific detectivity (D_{ph}), linear dynamic range (LDR), external quantum efficiency (EQE), noise equivalent power (NEP), photoresponse (t_r)/decay time (t_d), and mechanical flexibility, are the figure of merits of flexible SPPDs.[348] The effects of intrinsic defects and defects induced during the processing of PIM photoactive layers on PDPs of SPPDs are discussed here. The defects and trap states in the PIM layer act as carrier recombination centers, leading to high dark current (I_d), low photocurrent (I_{ph}), and inferior performance of SPPDs.[174,349–351] Several protocols, such as 1) precursor compensation treatment,[350] 2) bulk heterojunction,[337,351] 3) metal ions doping,[188,352] 4) surface treatment with organic salts (PEAI),[195] 5) solvent additive as ionic liquids (ILs)[191] and pyridine,[195] 6) interface defects passivation with PMMA[353] were reported for reducing defects trap density, intrinsic and surface defects, interface defects, thus implying the enhancement in the PDPs of SPPDs.

Huang et al. reported the precursor-compensation treatment (PCT) of spin-coated Cs_2SnI_6 (CSI) films resulting in a pinhole-free and pure phase photoactive layer for SPPDs (FTO/TiO$_2$/PCT-CSI or controlled CSI/Spiro-OMeTAD/Au, *n-i-p* device structure).[350] A higher photocurrent gain (151) was achieved for PCT-CSI-based SPPDs than controlled devices (81). Furthermore, improved PDPs, with R_{ph} of 1.07 (0.0059) mA W^{-1}, D_{ph} of 6.03×10^{10} (2.94×10^{10}) Jones, and t_r/t_d of 0.59 s/1.90 s (2.68 s/4.20 s), were reported for PCT-CSI (controlled CSI) based SPPDs.[350] The inferior PDPs of the controlled CSI-based SPPDs were attributable to incomplete surface coverage (presence of voids), nonuniform surface morphology, I-deficient chemical composition, and low carrier mobility (1.93 cm^2 V^{-1} s^{-1}).[350] The voids on the CSI surface act as surface defects, in turn acting as charge trapping centers/recombination centers. These lead to high dark current (leakage current), low photocurrent, and poor charge transport properties in SPPDs.[183,350] The 98% retention of D_{ph} value over 28 days in ambient air (relative humidity (RH) = 20–30% at room temperature (RT)) indicates the good environmental stability of PCT-CSI-based SPPDs.[350] The superior stability of devices owing to uniform surface coverage, dense and compact surface morphology, and I-rich chemical composition can prevent the formation of intrinsic defects.[350] In contrast, the fast degradation of D_{ph} (retention of 78%) values of controlled CSI devices during the same period (28 days) was ascribed to the acceleration of ion migration (iodine vacancies (V_I)) in the device.[183,349,350] The power-dependent *I-V* (**Figure 20**a) and *I-t* (Figure 20b) characteristics of $CsCu_2I_3$ heterojunction-based SPPDs (In/n-GaN/CsCu$_2$I$_3$/p-CuI/Au) provide information on the possible intrinsic defects in the $CsCu_2I_3$ and interface defects at heterojunctions.[354] A gradual increment in photocurrent (I_{ph}) was observed with the increase in light (365 nm) illumination from 0.01 to 8.88 mW cm^{-2} (Figure 20c).[354] The photocurrent and light intensity relationship is as follows: $I_{Ph} = \alpha P^\beta$ $I_{Ph} = I_l$-I_d is the photocurrent, α is a constant, and P is the light intensity. The β is constant varied from 0–1, which helps in understanding the photoconductive mechanism in the SPPDs.[354] According to the Rose–Bube theory, a lower β value (0.44) indicates

higher recombination of photogenerated charge carriers via trap centers within the optical bandgap of the $CsCu_2I_3$.[354,355] A lower β value also suggests complex electron-hole generation, trapping, and recombination processes involved in the heterojunction device.[354,355] The R_{ph}, D_{ph}, and EQE were gradually reduced with the increase in light intensity, demonstrating the higher carrier recombination possibility under high light intensity.[354] The maximum PDPs include light current (I_l)/dark current (I_d) ratio of 9.78×10^4, R_{ph} of 71.7 mA W^{-1}, D_{ph} of 3.3×10^{12} Jones, LDR of 99.8 dB, EQE of 26.1% were reported for $CsCu_2I_3$ heterojunction-based SPPDs.[354] The power-dependent *I-t* characteristics of SPPDs reveal that the faster t_r/t_d (160 ms/160 ms) was observed at lower light intensity (<0.56 mW cm^{-2}) (Figure 20b).[354] In comparison, a slower t_r (8.8 s) was noticed at higher light intensity (8.88 mW cm^{-2}), which might result from carrier trapping/releasing due to defects at CuI/CsCu$_2$I$_3$/GaN heterojunction interface.[354] The interfacial defects at the heterojunction interface in the SPPDs can be passivated by an ultra-thin PMMA layer or Al$_2$O$_3$ layer.[353,356]

Generally, a high processing temperature (>200 °C) is necessary to obtain a PIM photoactive layer with high crystallinity and low trap density for high-performance SPPDs.[340] However, the high concentration of the defects in the PIM layers processed at low temperatures negatively impacts the PDPs of flexible SPPDs. Defect mitigation routes like metal ions doping (Mn$^+$, Rb$^+$, Li$^+$, and others),[191,340] ionic liquids (ILs),[191] and surface treatment with organic salts (PEAI),[195] thiophene-2-carbohydrazide (TAH)[357] and phenyl-ethyl ammonium (PEA$^+$)[333]) have been employed. For instance, the effect of alkali metal ions (Li$^+$, Na$^+$, K$^+$, and Rb$^+$) doping on surface morphology and PDPs were studied on $Cs_2AgBiBr_6$ (CABB)-based SPPDs (PEN or glass/ITO/SnO$_2$/CABB/Ag) implemented on rigid and flexible substrates.[188,352] The compact, pinhole-free, and smooth surface morphology was reported for Rb-doped CABB ($Rb_{0.1}Cs_{1.9}AgBiBr_6$) films compared to undoped and other alkali dopant-based CABB films.[188] The I_l/I_d ratio of the Rb-doped CABB-based SPPDs was ≈70 000, demonstrating ≈3 orders of magnitude enhancement compared to the undoped CABB devices.[188] In addition, the highest R_{ph} of 0.23 A W^{-1}, D_{ph} of 1.6×10^{13} Jones, LDR of ≈177.8 dB, and t_r/t_d of 1.6 µs/1.6 µs were achieved for Rb-doped CABB SPPDs on a rigid substrate.[188] The higher performance of Rb-doped CABB devices might be due to dense, compact, uniform surface morphology, lower defect density, and superior carrier transport properties leading to lower dark current ($I_d = 1.3 \times 10^{-11}$ A, which is ≈2 orders of magnitude lower).[188] The Rb-doped CABB device has shown a negligible decay in I_{ph} value even after 20 days in the air (RT and RH of 30%), unlike the other devices, demonstrating the stability and reliability of the devices.[188] Furthermore, the flexible SPPDs were implemented on polyethylene naphthalate (PEN) substrate with CABB and Rb-doped CABB as photoactive layers.[188] The I_l/I_d ratio of CABB and Rb-doped CABB-based devices was 1.2 and 4.8.[188] The lower temperature annealing of the photoactive layers (CABB or Rb CABB) leads to a higher dark current (10^{-6}A) and high defect density, implying a lower I_l/I_d ratio of devices.[188] The dark current was suppressed in the presence of a hole transport layer (P3HT) in SPPDs (PEN/ITO/SnO$_2$/CABB or Rb CABB /P3HT/Ag, n-i-p device structure).[188] The maximum I_l/I_d ratio of 400, R_{ph} of 0.26 A W^{-1},
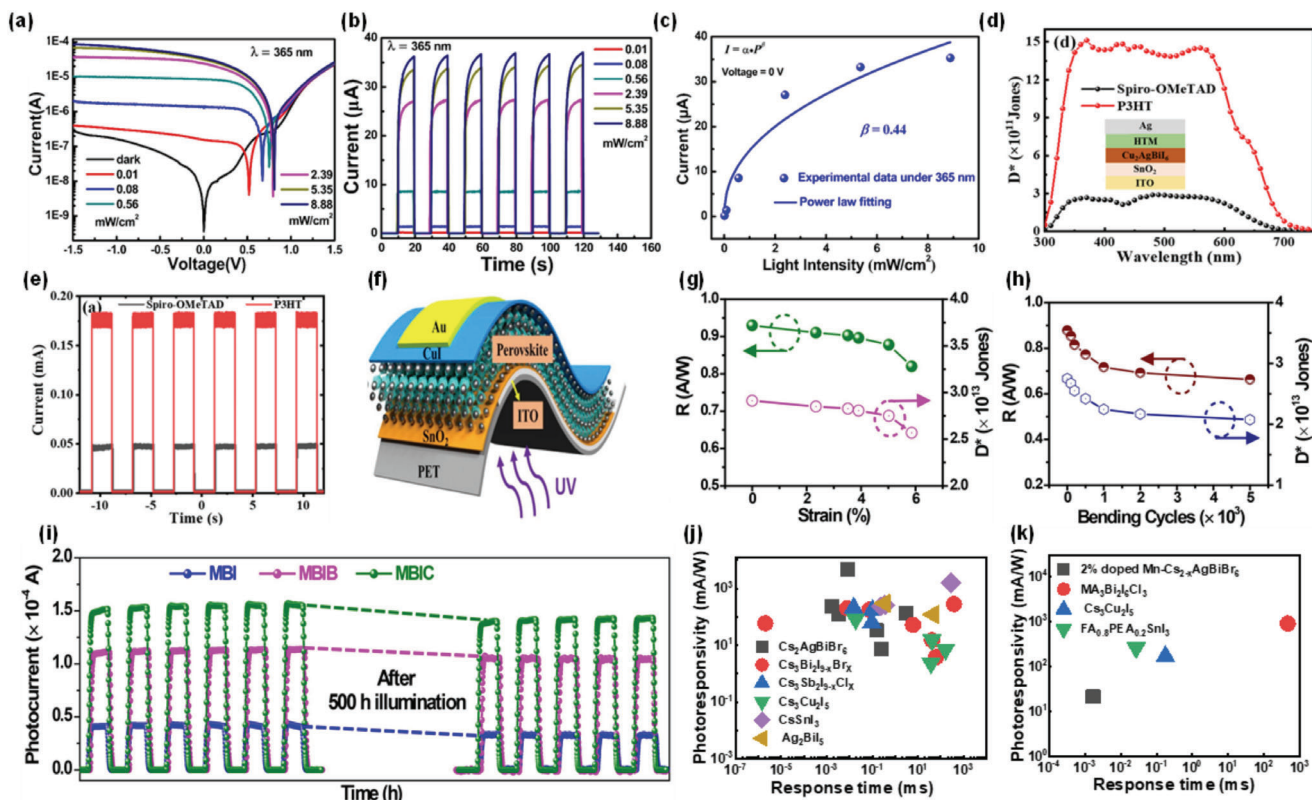
ADVANCED
SCIENCE NEWS

www.advancedsciencenews.com

ADVANCED
FUNCTIONAL
MATERIALS

www.afm-journal.de

Figure 20. Power-dependent a) *I-V*, b) *I-t* characteristics, and c) photocurrent (I_{ph}) of $CsCu_2I_3$ heterojunction-based self-powered photodetectors (In/n-GaN/CsCu$_2$I$_3$/p-CuI/Au) under the illumination of 365 nm light sources. Panels (a)–(c) are reproduced with permission.[354] Copyright 2022, Elsevier. d) Photodetectivity spectrum of the Cu_2AgBiI_6-based photodetector. e) Effect of hole transport layers on specific detectivity Cu_2AgBiI_6-based SPPDs. Panels (a)–(c) are reproduced with permission.[195] Copyright 2022, American Chemical Society. f) Schematic diagram of $MA_3Bi_2I_6Cl_3$ (MBIC)) based flexible SPPDs. g) Responsivity (R_{ph}) and specific detectivity (D_{ph}) of MBIC-based SPPDs as a function of bending strains (or different radii) under the illumination of 382 nm. h) R_{ph} and D_{ph} of MBIC-based SPPDs for 5000 bending cycles at strain of 5% under the illumination of 382 nm. i) The long-term stability of three different photodetectors measured under continuous UV light (382 nm) illumination for 500 h with an intensity of 1.0 mW cm^{-2}. Panels (f)–(i) are reproduced with permission.[217] Copyright 2023, Elsevier. Progress in the Responsivity (R_{ph}) and photoresponse time of different SPPDs on j) rigid and k) flexible substrates. Panels (j) and (k) are constructed using the information provided in Table 5.

D_{ph} of 3.2×10^{11} Jones, and LDR of ≈152 dB of flexible Rb-doped CABB-based SPPDs with HTL layer under weak light illumination of 3.6 µWcm^{-2}.[188]

Zhang et al. reported that pyridine is an effective solvent additive for fabricating dense, pin-hole free, and continuous Cu_2AgBiI_6 photoactive layer (Figure 20e).[195] The delocalized π electrons in pyridine are responsible for the complete dissolution of the precursor salts in a polar solvent at room temperature, and aid in the uniform Cu_2AgBiI_6 film formation at a low temperature of 150 °C.[195] In addition, a PEAI treatment was employed to suppress the nonradiative recombination by passivating the bulk and surface defects of Cu_2AgBiI_6 film.[195] The PEAI-treated Cu_2AgBiI_6 films possess hydrophobic surfaces, which improved the stability of Cu_2AgBiI_6-based SPPDs against ambient moisture.[195] The Cu_2AgBiI_6-based SP-PDs (ITO/SnO$_2$/ Cu_2AgBiI_6/HTL/Ag) were fabricated with two HTLs, namely, Spiro-OMeTAD and P3HT (Figure 20e).[195] The higher photocurrent and faster t_r/t_d = 1.11 ms/3.32 ms was reported for P3HT-based SPPDs than Spiro-OMeTAD-based devices (t_r/t_d = 1.17 ms/3.66 ms) (Figure 20e). The broadband R_{ph} (≈0.085 A W^{-1}) and D_{ph} of ≈10^{12} Jones were noticed in the wavelength range from 350 to 600 nm for Cu_2AgBiI_6-based SPPDs

(Figure 20e).[195] The selection of a suitable HTL layer is critical for proper band alignment and suppressing the dark current for obtaining high-performance SPPDs.[195]

Shuang et al. addressed the effect of the DMF content in DMSO solvent and the spin coating speed on film quality (in terms of dense, compact, and large grain size with a uniform surface) with minimized defects (trap-state density) upon controlling the pinholes in CABB film, which can reduce the dark current and enhance the photocurrent (I_{ph}) of CABB-based SPPDs.[191] Furthermore, high-quality CABB films were fabricated at a lower temperature (150 °C) by adding 1-Butyl-2,3-dimethylimidazolium chloride IL as a solvent additive to the optimal $Cs_2AgBiBr_6$ perovskite precursor solution.[191] The TRPL analysis revealed the longest carrier lifetime for CABB films prepared with IL and annealed at 150 °C, which displayed excellent crystal quality and minimum non-radiative recombination, in turn being potentially suitable for constructing the high-performance SPPDs.[191] Furthermore, the highest I_l/I_d ratio was reported for CABB films prepared with optical 2.5 mL IL.[191] The optimal IL (2.5 mL)-based CABB films-based SPPDs were implemented on rigid and flexible substrates. The PDPs such as I_l/I_d ratio of 1.66×10^4 (0.5×10^4), R_{ph} of 0.075 (0.031)A W^{-1},

ADVANCED
SCIENCE NEWS

www.advancedsciencenews.com

ADVANCED
FUNCTIONAL
MATERIALS

www.afm-journal.de

D_{ph} of 1.87×10^{12} (8.04×10^{11}) Jones, t_r/t_d of ≈0.24/0.29 ms, LDR of 100 dB for rigid (flexible) substrate-based SPPDs under the illumination of 473 nm laser,[191] respectively. The stable device performance after 25 days stored at room temperature in the air with an RH of 50% ± 10%, as well as holding of 75% of I_{ph} at 333 K for 6 h, indicates that IL passivated defects in fabricated CABB film, in turn, enhanced the environmental and thermal stability of SPPDs.[191] The 85% hold of I_{ph} after 5000 bending cycles with a radius of 6.4 mm demonstrates that flexible CABB-based SPPDs have potential in flexible wearable devices.[191] Apart from the processing parameters and intrinsic defects, the structural dimensionality and chemical composition of the PIM photoactive layer influence the PDPs of SPPDs.[217,355] Mei et al. addressed the effects of the structural dimensionality of Sb-based PIMs ($Cs_3Sb_2X_9$) and 2D $Rb_3Sb_2I_9$ (2D-RSI)) based photoactive layers for SPPDs (FTO/TiO$_2$/PIM/Poly-TPD/Au, n-i-p device structure).[355] The highest and broad PDPs, with R_{ph} of 205 (174) mA W^{-1}, D_{ph} of 6.1×10^{12} (3.5×10^{12}) Jones, LDR of 193 (175) dB, t_r of 15μs (101μs) and EQE of 54.8% (50%), were obtained for 2D-$Cs_3Sb_2I_{9-x}Cl_x$ (2D-RSI) based SPPDs compared to 0D $Cs_3Sb_2I_9$ based devices (62 mA W^{-1}, 4.3×10^{12} Jones, 51.3 dB, 94μs, and 25%),[355] respectively. The larger PDPs might be due to higher mobility, longer carrier lifetimes, and decreased STE formation in 2D-$Cs_3Sb_2I_{9-x}Cl_x$ (2D RSI).[355] The 87% and 47% retention of I_{ph} for 2D and 0D PIM-based SPPDs without encapsulation for 600 h confirm the superior stability of 2D PIM layers-based devices over their 0D counterpart.[355]

Vuong et al. investigated the effect of the chemical composition tuning of methylammonium bismuth iodide (($MA_3Bi_2I_9$ (MBI)), ($MA_3Bi_2I_6Br_3$ (MBIB)) and $MA_3Bi_2I_6Cl_3$ (MBIC)) based photoactive layers for flexible SPPDs (Figure 20f).[217] The highest PDPs, such I_l/I_d ratio of ≈10³, R_{ph} of 0.92 A W^{-1}, D_{ph} of ≈2.9 × 10¹³ Jones, EQE of 30.2%, faster photoresponse (t_r/t_d = 0.46 /0.41 s) for MBIC based flexible SPPDs, under the illumination of 382 nm light source (0.04 mW cm^{-2}), compared to other devices (**Table 5**).[217] The better figures of merit were attributed to high crystallinity, compact, dense, smooth surface morphology with improved interconnection between the grains, higher carrier mobility, and lower trap density of MBIC films.[217] The 95% retention of R_{ph} and D_{ph} values were reported for bending strain up to 5% (bending radius of 3.7 mm) for MBIC-based flexible SPPDs (Figure 20g), and the PDPs parameters were degraded for higher bending strain (6%).[217] The devices upheld 85% of the initial R_{ph} and D_{ph} values after 5000 bending cycles at 5% strain (Figure 20h), demonstrating the excellent mechanical stability of the MBIC-based SPPDs.[217] The decrement in PDPs parameters at higher strain (6%) was accredited to the crack formation of the surface of the perovskites and a top-gold electrode after 1000 bending cycles.[217] The >94% retention of I_{ph} value, even after an exposure time of 500 h in the air (RH ≥ 75% at RT), demonstrates the excellent photostability of MBIB and MBIC-based SPPDs (Figure 20i).[217] In contrast, the I_{ph} value of the MBI devices decreased to 15% same exposure conditions. The MBIB and MBIC-based SPPDs displayed superior photostability ascribed to the suppression of iodine vacancies through halide substitution in MBI films.[217] These devices exhibited excellent robustness against mechanical stress and long-term photostability, promising suitability in next-generation flexible, foldable, and low-cost flexible SPPDs.[217]

The recent progress in PDPs of SPPDs with various PIMs, such as bismuth-based (Ag_2BiI_5,[204] Cu_2AgBiI_6,[195] $Cs_2AgBiBr_6$,[188,352,191] $CsBi_3I_{10}$,[202] $Cs_3Bi_2I_9$,[341] and others), antimony-based[355] ($Cs_3Sb_2I_{9-x}Cl_x$ and 2D $Rb_3Sb_2I_9$), Cs_2SnI_6[350] and Cu-based ($Cs_3Cu_2I_5$)[334] and their heterojunctions with Si (p- or n-type) is shown in Figure 20j,k and summarized in Table 5. The SPPDs based on $Cs_2AgBiBr_6$,[201,203,343] $CsBi_3I_{10}$,[202] Ag_2BiI_5,[204] $Cs_3Bi_2I_9$,[40,341,358,359] Cs_2SnI_6[350] and $Cs_3Cu_2I_5$,[334,360,361] retained >85-95% of I_{ph} values under environmental storage (more than 30 days in the air at room temperature and under RH of 30–50%), thermal treatment (up to >60 °C) and light exposure (continuous illumination for >5 h) (Table 5). The degradation of I_{ph} in SPPDs might be ascribed to ion migration due to the deficiency of halides, nonradiative sites in the devices, and degradation of the metal/perovskite interface, which increases dark current with environmental storage over time.[40,201–204,334,341,343,349,358,359,360–363] Furthermore, the I_{ph} decreased in SPPDs at high temperatures owing to thermally activated free carriers from halide vacancies (V_I, V_{Br}, and V_{Cl}) and interstitial defects (for example, Sn_i) in the PIM photoactive layers.[40,201–204,334,341,343,349,358,359,360,361]

7. Memristors

Developing operationally stable, flexible memristors with multi functionalities, such as ultra-low power, electro-forming free, self-compliance, and multi-bit, will benefit next-generation high-density data storage,[367,205] computation,[214,368] encryption,[368] healthcare,[367] wearable electronics,[367] hardware security[369] (physical unclonable functions (PUFs) and true random number generators (TRNGs)[370]), and IOT device applications.[367,369] The memristor comprises of a simple device architecture configured with a bottom electrode-resistive switching (RS) layer–top electrode (**Figure 21**a). This review focuses on lead-free perovskite-inspired RS layers for rigid and flexible memristors. The device schematic of the $A_3Bi_2I_9$ (A = Rb, Cs) PIM RS layer-based memristor (Au/$A_3Bi_2I_9$/Pt) on a rigid SiO$_2$ substrate is shown in Figure 21a.[371] Generally, the electro-forming (EF) process is required to trigger RS characteristics in the PIM (for example, $A_3Bi_2I_9$) RS layer-based memristors due to their initial high resistance state (HRS) values (Figure 21b).[371] The EF was performed with constant current compliance (CC = 1 mA) to prevent the permanent breakdown of devices.[371] The EF voltage of $Cs_3Bi_2I_9$ and $Rb_3Bi_2I_9$ based devices was 1.3 and 1.5 V, respectively. After electro-forming, the device switches from HRS to a low resistance state (LRS) (Figure 21c).[371] The EF voltage is always higher than the memristor operating voltage (V_{set}//V_{reset}) (Figure 21b,c).[371] The RS properties RSPs, such as operating voltage (set (V_{set}) /reset voltage (V_{reset})), R_{On}/R_{Off} ratio, and endurance, retention, switching speed, stability, and mechanical flexibility are the figure of merits of flexible memristors.[367,369] It is well known that the migration of ions (for instance, iodine vacancy (V_I) and iodine ions (I^-)) inside the PIM RS layer is responsible for the RS characteristics of memristor devices (Figure 21b).[372,373] These defects (halide vacancies and their ions) adversely affect RS performance, specifically the higher operating voltage range.[369,372,374] Therefore, controlling defects migration in the RS layer during RS operation is essential for reliable RS performance.[369] The role of defects in the PIM

**ADVANCED
SCIENCE NEWS**

www.advancedsciencenews.com

**ADVANCED
FUNCTIONAL
MATERIALS**

www.afm-journal.de

Table 5. Comparison of PDPs of lead-free PIM-based self-powered photodetectors.

Device structure/Operating) wavelength (nm)	R_{ph} [mA W^{-1}]	D_{ph} (×10^{10}) [Jones]	t_r/t_d [ms]	ON/Off ratio /EQE	Stability (retain of PDPs)	Ref.
Au/Cs$_2$AgBiBr$_6$/Ag, 400 nm Asymmetric electrode-based devices	4880	1220	0.008/0.0088	>10^3/20%	I_l/I_d ratio >10^2 stable over 180 days	[343]
Ag/Cs$_2$AgBiBr$_6$/ITO, 375 nm Asymmetric electrode-based devices		11.9	0.0061/0.028s	6.6 × 10^3	50 days in air, 85% retention of I_{ph} at 358K and 263K for 1 h, relative humidity (85%)	[201]
FTO/Cs$_3$Bi$_2$I$_9$/Ag, Schottky device Broadband (450–950 nm)	3.8	160	62.74/90.25	1.4 × 10^4	95% retention of I_{ph} after 90 days	[341]
FTO/Al$_2$O$_3$/Cs$_3$Bi$_2$I$_9$/Au 405 nm, Schottky device	100	N/A	N/A	3.85 × 10^3	30 days in air	[40]
Ag/FTO/Cs$_3$Bi$_2$I$_9$/C 405 nm, Schottky device	0.005	0.059	1.52s/2.29s	10^2		[342]
FTO/TiO$_2$ / Cs$_2$SnI$_6$/ SpiroOMeTAD/Au white light, n-i-p photovoltaic devices	1.07	2.94	0.59/1.90s	151	98% of D_{ph} after 28 days	[350]
FTO/TiO$_2$/ 2D-Rb$_3$Sb$_2$I$_9$ /poly-TPD/Au Broadband (350–600 nm), n-i-p photovoltaic devices	174	430	0.101	N/A	87% I_{ph} over 600 h under light	[355]
FTO/TiO$_2$/ 0D-Cs$_3$Sb$_2$I$_9$ /poly-TPD/Au Broadband (350–600 nm), n-i-p photovoltaic devices	62	350	0.094	N/A	47% I_{ph} over 600 h under light	[355]
FTO/TiO$_2$/2D-Cs$_3$Sb$_2$I$_{9-x}$Cl$_x$/poly-TPD/Au, Broadband (350–600 nm), n-i-p photovoltaic devices	205	610	0.015	N/A	87% I_{ph} over 600 h under light	[355]
ITO/SnO$_2$/Cs$_3$Bi$_2$I$_9$-SC /PTAA /Au /ITO, 405 nm, n-i-p photovoltaic devices	52.06	219	6 /6.8	5700	90% I_{ph} over 75 days and 76% I_{ph} after 18.5h	[358]
ITO/PEDOT:PSS/Cs$_3$Bi$_2$I$_{9-x}$ Br$_x$/ /C60/BCP/Ag, Broad band (300–600 nm) p-i-n photovoltaic devices	15	46	40.7/27.1	4.1 × 10^4	96% of I_{ph} over 100 days	[359]
ITO/SnOx/MA$_3$Bi$_2$I$_9$/Spiro-OMeTAD/Au 382 nm, 528 nm n-i-p photovoltaic devices	280	880	380/450		>95% of I_{ph} over 100 days	[182]
FTO/TiO$_2$/ Ag$_2$BiI$_5$ / SpiroOMeTAD /Ag, Broad band (350–700 nm), n-i-p photovoltaic devices	120	20	45 to 175	27%		[264]
In–Ga/p-Si/PMMA/Cs$_3$Cu$_2$I$_5$ MCs/Au, 298 nm, Heterostructured-based devices	15.2	81	41.43/47.84	4.14 × 10^3	95% retention of stable over 8 h under light @293K and 60 days in the air.	[353]
In–Ga/p-Si NWs/Cs$_3$Cu$_2$I$_5$ NCs/Au, Broadband (265–1000 nm), Heterostructured-based devices	83.6	21	0.018.2	3.72 × 10^3	95% retention of stable over 10 h under light @293K and 300 days in the air.	[364]
Au/n-Si /Cs$_3$Cu$_2$I$_5$ film/LiF/Al, 330 nm Heterojunctions	7.1	26	160/160	2.15 × 10^3	N/A	[360]
SiO$_2$/Ag/Si/ CsBi$_3$I$_{10}$/Au Broadband (256–980 nm), Heterojunctions	178.7	4.99	0.073/0.036	≈1 × 10^4/27.2%	Stable over 3 months	[365]
quartz In/GaN/ CsCu$_2$I$_3$/ CuI/Au, 365 nm Heterojunctions	71.7	330	8.8/0.32s	9.7 × 10^4/26.1%	N/A	[354]

(Continued)

Table 5. (Continued).

Device structure/Operating) wavelength (nm)	R_{ph} [mA W^{-1}]	D_{ph} ($\times 10^{10}$) [Jones]	t_r/t_d [ms]	ON/Off ratio /EQE	Stability (retain of PDPs)	Ref.
Ti-Au/β-Ga$_2$O$_3$/Cs$_3$Cu$_2$I$_5$/Au, 265 nm Heterojunctions	2.33	0.024	37/45	5.1×10^4	60 days stable in air, I_{ph} stable over 12 h under light	[360]
ITO/ SnO$_2$/CsBi$_3$I$_{10}$/Au Broadband (360–800 nm) Heterojunction based devices	200	1800	0.0078/0.0088	2.33×10^5/30%	73 days in the air, 93% retention of I_{ph} value for 333K for 4h	[202]
ITO/ Cs$_3$Bi$_2$Br$_9$ SC//Cs$_3$BiBr$_6$ SC/Au 360 nm, Bulk Heterojunction	59.4	120	200 ns/1.09 μs	1.88×10^4	Stable even after 30 days	[337]
Sapphire/In/GaN/Cs$_2$AgBiBr$_6$/NiO/Au Heterojunction based devices	2.09–33	2.07–32.7	0.151/0.215	10^3	N/A	[340]
ITO/SnO$_2$/Cs$_2$AgBiBr$_6$/Au (350–480 nm), Heterojunction	110–130	2.1–2.4	3	38.5%	180 days in air, thermally stable upto 358K	[203]
FTO/SnO$_2$/Cs$_2$AgBiBr$_6$/C, 473 nm (145 mW cm^{-2}), Heterojunction	7.5	187	0.24/0.29	1.66×10^4	25 days in air, 75% retention of I_{ph} value for 333K for 6h	[191]
FTO/SnO$_2$/2%Mn-Cs$_{2-x}$AgBiBr$_6$/Ag, 405 nm (0.45 mW cm^{-2}), Heterojunction	120.8	34.5	0.0034/0.002	2.7×10^4	80% retention of I_{ph} after 23 days	[352]
FTO/SnO$_2$/Cs$_{1.9}$Rb$_{0.1}$AgBiBr$_6$/Ag, 405 nm (0.45 mW cm^{-2}), Heterojunction	230	1600	0.0016/0.0016	7.00×10^4	20 days stable in air	[188]
FTO/TiO$_2$/ (CH$_3$NH$_3$)$_3$Bi$_2$I$_9$ (MBI)/graphite, Heterojunction	80	0.08	0.79/0.36s		N/A	[366]
ITO/SnO$_2$/ Ag$_2$BiI$_5$/Au (365- 440)nm, Heterojunction	300	530	0.34/0.26		25 days in air, 91% retention of I_{ph} upto 373K	[204]
Flexible devices						
PEN/ITO/SnO$_2$/Rb$_{0.1}$Cs$_{1.9}$AgBiBr$_6$/ P3HT/ Ag, 405 nm, Heterojunction	260	32	N/A		N/A	[188]
FTO/SnO$_2$/2%Mn-Cs$_{2-x}$AgBiBr$_6$/Ag, 405 nm (1.8 mW cm^{-2}), Heterojunction	21.6	2.46	0.0017/0.0018	1.60×10^3	90% retention of I_{ph} after 700 bending cycles	[352]
PET/ITO/SnO$_2$/Cs$_2$AgBiBr$_6$/ C 473 nm (14.5 mW cm^{-2})	31	80.4	N/A	$\approx 0.5 \times 10^4$	85% retention of I_{ph} after 5000 bending cycles	[191]
PET/ITO/SnO$_2$/MA$_3$Bi$_2$I$_6$Cl$_3$ (MBIC)/ CuI/ Au, 382 nm (0.04 mW cm^{-2}) n-i-p photovoltaic devices	920	2900	460/410		95% of I_{ph} over 500 h, No changes of R_{Ph} and D_{ph} over 1000 cycles at low strain	[217]
PET/ITO/SnO$_2$/MA$_3$Bi$_2$I$_6$Br$_3$ (MBIB) / CuI/ Au, 382 nm (0.04 mW cm^{-2}) n-i-p photovoltaic devices	630	2000	N/A		95% of I_{ph} over 500 h after light illumination	[217]
PET/ITO/SnO$_2$/MA$_3$Bi$_2$I$_9$Br$_3$ (MBI) / CuI/ Au, 382 nm (0.04 mW cm^{-2}) n-i-p photovoltaic devices	300	900	N/A		85% of I_{ph} over 500 h after light illumination	[217]
PET/ITO/PEDOT:PSS/Cs$_3$Cu$_2$I$_5$/Au, 275 nm (480.3 μW cm^{-2}) Heterojunction	170.3	1000	0.177/0.195	$\approx 5.7 \times 10^3$/76.8%	Decay of 11.7% and 20.0% of R and D after 12 months	[334]
PEN/ITO/PEDOT:PSS/FA$_{0.8}$PEA$_{0.2}$SnI$_3$ /PCBM/BCP/Ag, 630 nm (480.3 μW cm^{-2}) p-i-n photovoltaic devices	262	230	0.027/0.02	70	R-value does not change even after 10 000 bendings	[333]

**ADVANCED
SCIENCE NEWS**

www.advancedsciencenews.com

**ADVANCED
FUNCTIONAL
MATERIALS**

www.afm-journal.de
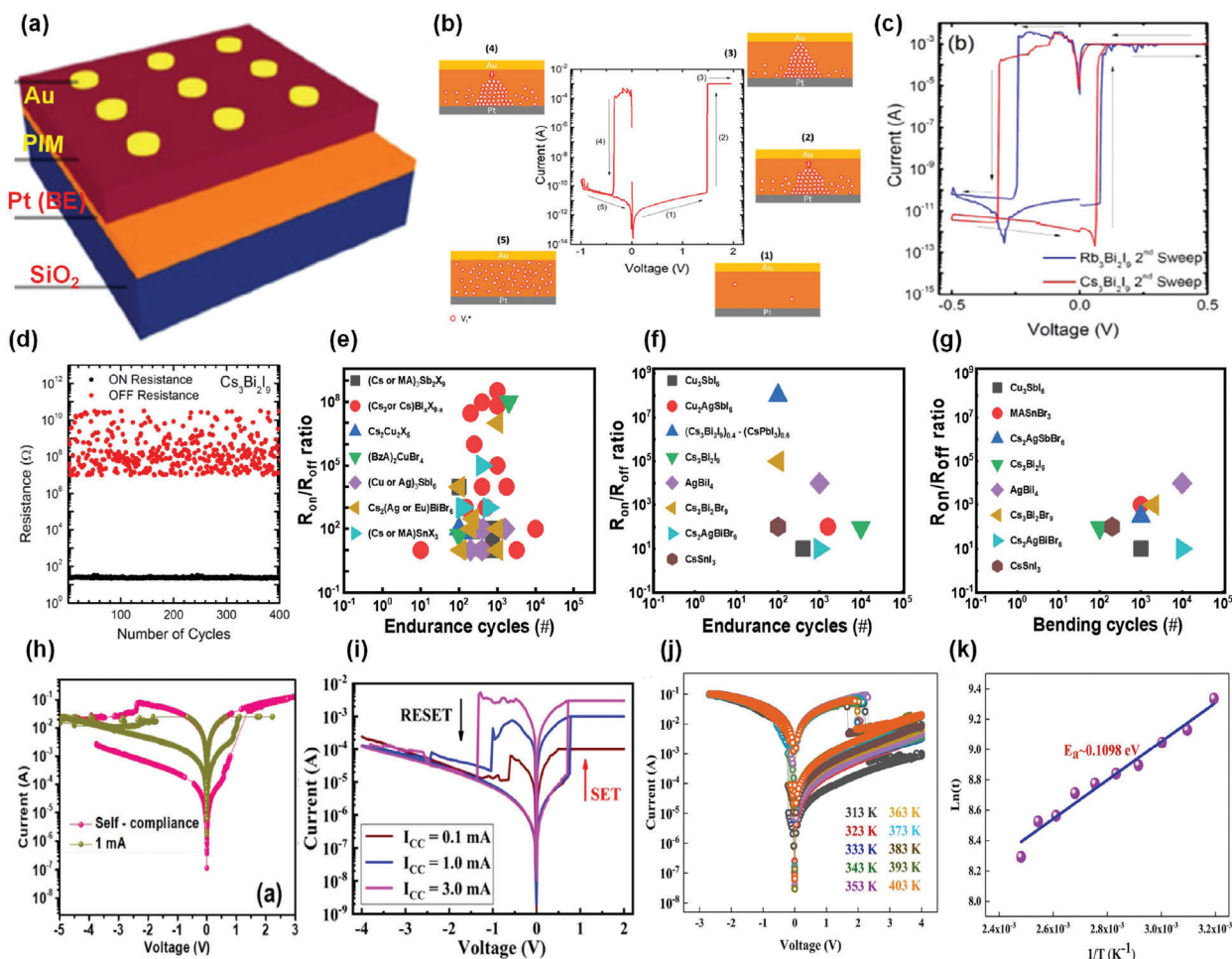
Figure 21. a) Schematic diagram of $A_3Bi_2I_9$ layer-based memristor ($Au/A_3Bi_2I_9$/Pt, A = Cs, Rb) on rigid SiO_2 substrate. b) Different steps in resistive switching of $Rb_3Bi_2I_9$-based memristors: 1) Pristine state, 2) electro-forming process, 3) low resistance state (LRS) after forming, 4) rupturing process, and 5) high resistance state (HRS). c) I-V bipolar resistive switching (BRS) characteristics of $A_3Bi_2I_9$ layer-based memristors after electro-forming. d) Endurance performances of $Au/Cs_3Bi_2I_9$/Pt devices at V_{set} = 0.5 V. Panels (a)–(d) are reproduced with permission.[404] Copyright 2018, American Chemical Society. e) Progress in lead-free PIM RS layers-based memristors on rigid substrates: R_{on}/R_{off} ratio versus endurance cycles. Progress in lead-free PIM RS layers-based memristors on flexible substrates: f) R_{on}/R_{off} ratio versus endurance cycles and g) R_{on}/R_{off} ratio versus bending cycles. Panels (e)–(g) are constructed using the information provided in Table 6. h) I-V BRS characteristics of $MAPbI_3$ layer-based memristors with current compliance (CC) and self-compliance mode. Reproduced with the permission.[435] Copyright 2022, American Chemical Society. i) I–V BRS characteristics of Cu_2AgSbI_6 layer-based memristors with current compliance (CC): Multiple LRS state (Multi-bit). Reproduced with permission.[411] Copyright 2022, American Chemical Society. j) I–V BRS characteristics of Al/Cs_2NaBiI_6/ITO device with different temperatures. k) Plot of ln(t) versus the inverse of the measured temperatures. Panels (j) and (k) are reproduced with permission.[412] Copyright 2022, Elsevier.

RS layers for electro-forming free, self-compliance, multi-bit characteristics of memristor devices are discussed in the following subsections. In addition, the effect of dimensionally, chemical composition, and morphology of the PIM RS layer on the R_{On}/R_{Off} ratio, operating voltage (V_{set}/V_{reset}), and stability (endurance and retention) of memristor devices are also highlighted.

7.1. Effect of Physical Characteristics of PIM RS Layer on Memristor Performance

The RS properties and reliability of memristors strongly depend on the physical characteristics of the PIM RS layer, such as the thickness,[375–377] morphology,[206,378–380] chemical composition (halides),[381–383] dimensionality,[207,379,383] and defects.[372,373,384] The surface quality[371,385] and surface roughness,[371,386] grain size,[205,385–387] and density of grain boundaries[205,385,388] in the polycrystalline PIM RS layer play a pivotal role in the reliable RS properties of memristor devices.[380,385,386] For instance, the effect of $A_3Bi_2I_9$ (A = Rb, Cs) PIM RS layer surface roughness on the reliability of memristor ($Au/A_3Bi_2I_9$/Pt) devices was studied.[371] The fabricated memristor displayed bipolar resistive switching (BRS) with an ultralow V_{set}/V_{reset} (0.09 V/−0.24 V), R_{On}/R_{Off} ratio (>10^7) (Figure 21c), retention properties (10^3 s), and low endurance cycles (200 for $Rb_3Bi_2I_9$ and 400 for $Cs_3Bi_2I_9$) (Figure 21d).[371] The inferior endurance of these devices is related to the surface quality (or surface roughness) of the RS layer,

which is associated with the electric field distributions within the device.[206,369,371] The non-uniform electric field distributions within the device, because of the higher surface roughness of the RS layer, leads to the multifilament formation, thus lowering the endurance properties of the devices.[371,369,207] The fluctuation in the HRS state (Figure 21d) might be due to the formation of multiple filaments or incomplete rupturing filaments during the reset process of the device.[206,369,371] The iodine vacancy (V_I) based valance change mechanism (VCM) is responsible for RS characteristics in $A_3Bi_2I_9$ based memristors.[371] The ions (V_I and I^-) can easily migrate via the grain boundary regions compared to bulk because of their lower energy than the bulk region, thus leading to the ultralow V_{set}/V_{reset} of the memristor.[371,389,390] The pinhole-free, compact, low surface roughness, and uniform morphology of $Cs_3Sb_2X_9$ (X = I, Br, and Cl), $Cs_3Bi_2I_6Cl_3$, $Cs_3Bi_2Br_9$, $BA_2CsAgBiBr_7$, $MA_3Bi_2I_9$, Cu_2AgSbI_6, $(C_6H_5CH_2NH_3)_2CuBr_4$, dual-phase (($(Cs_3Bi_2I_9)_{0.4}$-$(CsPbI_3)_{0.6}$, $AgBi_2I_7$-$CsBi_2I_9$)) RS layers lead to reliable RS properties (>500 endurance cycles, R_{On}/R_{Off} > 10^2 and retention>10^3 s) of rigid substrate based memristors (Figure 21e and **Table 6**).

The dimensionality of the PIM RS layer highly influences the RS properties of memristors.[207,379,383] Likewise, lower V_{set}/V_{reset} (0.22 V/−0.45 V) and higher R_{On}/R_{Off} ratio (10^4) were reported for lower dimensional (0D-$Cs_3Bi_2I_9$) device as compared to 1D $Cs_3Bi_2Cl_9$ (10^2, 0.44/−0.97 V) and 2D-$Cs_3Bi_2Br_9$ devices (10, 0.67/−1.21),[383] respectively. The higher R_{On}/R_{Off} ratio is due to a large HRS resistance value of the 0D-$Cs_3Bi_2I_9$ device.[383] The free carrier density and migration rate of halide vacancies (V_I, V_{Br}, and V_{Cl}) control the resistance of the HRS state of the memristor.[383] The migration rate of halide vacancies can change with the reduction of dimensionality of metal halide perovskite because of the variation of activation energy (E_A) values.[383] The lower E_A indicates the easy migration rate of halide vacancies due to a smaller electric field.[383] The estimated E_A values based on DFT calculation for 0D ($Cs_3Bi_2I_9$), 1D (1D-$Cs_3Bi_2Cl_9$), and 2D (2D-$Cs_3Bi_2Br_9$) are 0.29, 0.59, and 0.98 eV, respectively, indicating the decrease of E_A with increasing the dimensionality. The higher E_A values denote the more difficult migration of V_I in the device, leading to the highest resistance of HRS value in 0D $Cs_3Bi_2I_9$.[383] The memristor properties can be tuned by chemical composition via changing the halides from I, Br, to Cl in PIM-based RS layers.[381–383] For example, the $Cs_3Sb_2Cl_9$-based memristor exhibited lower V_{set}/V_{reset} and higher R_{On}/R_{Off} ratios compared to the devices based on $Cs_3Sb_2X_9$ (X = I, Br) (Table 6).[382] The large HRS resistance leads to a higher R_{On}/R_{Off} ratio of $Cs_3Sb_2Cl_9$-based devices.[382] The decrease in operating voltage (V_{set}/V_{reset}) from −0.40 V/1.55 V to −0.21 V/1.34 V and the increase of R_{On}/R_{Off} ratio from 10^2 to 10^3 were reported for doping of chloride in $Cs_2AgBiBr_6$ RS layer ($Cs_2AgBiBr_5Cl$).[381] The smaller V_{set}/V_{reset} is correlated to the increase of defect density in the $Cs_2AgBiBr_5Cl$ RS layer, confirmed by TRPL analysis.[381] The progress in performance and RS mechanism of PIM RS layers-based memristors are summarized in Table 6. The migration of halide vacancies (V_I, V_{Br}, V_{Cl}, valence change mechanism (VCM)), cation ions (Ag^+, Al^+, and Cu^+, electrochemical metallization mechanism (ECM)), and combination of VCM and ECM are responsible for the RS characteristics (conducting filaments) of PIM RS layers-based memristors (Table 6).

7.2. Flexible Memristor

A flexible memristor is one of the essential compounds of wearable electronic devices.[367] The various lead-free PIM such as Cu_3SbI_6,[391] $Cs_3Bi_2I_9$,[375] $Cs_3Bi_2Br_9$ QDs,[205] $AgBiI_4$,[392] Cu_2AgSbI_6,[393] $Cs_2AgBiBr_6$,[394] $Cs_2AgSbBr_6$,[395] $MASnBr_3$,[396] dual-phase ($AgBi_2I_7$-$CsBi_2I_9$),[397] ($(Cs_3Bi_2I_9)_{0.4}$-$(CsPbI_3)_{0.6}$)[378]) were investigated as RS layers for rigid and flexible memristor devices (Figure 21e and Table 6). The mechanical flexibility (stability) on the RS properties of flexible memristor was performed by bending cycles at various bending radii,[205,208,397,398] bending lengths[395] and bending angles.[391,393] The lead-free dual dual-phase halide perovskites ($AgBi_2I_7$-$Cs_3Bi_2I_9$) based memristor was fabricated on rigid (SiO_2/Ti-Pt/($AgBi_2I_7$-$Cs_3Bi_2I_9$)/PMMA/Au) and flexible (cyclo-olefin polymer (COP)) substrate with an inert electrode (Au).[397] The device implemented on a rigid substrate showed BRS with ultra-low V_{set}/V_{reset} (0.15 V/−0.07 V), a high R_{on}/R_{off} ratio (>10^7), an endurance of 10^3 cycles, and long retention times (>5×10^4s).[397] The RS properties of the flexible device were sustained up to a bending radius of 5 and 3 mm.[397] However, the RS properties (R_{on}/R_{off} ratio = 10^2) of the flexible memristor were reduced at a smaller bending radius of 1 mm; this could be due to the higher HRS current level caused by increased tensile stress in the flexible device at a smaller bending radius.[397] The R_{on}/R_{off} ratio of the device was retained even after 1 month air exposure.[397] The deterioration of the reset process was noticed in the memristor after a month in the air because of the reduction of crystallinity.[397] It is attributed to the impeded ion migration properties in dual-phase perovskite films.[397] The R_{on} /R_{off} ratio versus bending cycles of flexible memristors based various PIM based RS layers are shown in Figure 21g. The progress in other PIM RS layers-based memristors is summarized in Table 6. The experimental bending test and theoretical studies[391,395,399] (integrated crystal orbital Hamilton population (ICOHP) bending analysis) revealed that RS properties degrade even for smaller bending radii of <5 mm; attributed to the changes in the chemical bond lengths in the PIM crystal structure, formation of a cracks on the flexible substrate and RS layer, and elevated tensile strain in memristors.[391,395,399] Selecting mechanically durable substrates and electrode materials is highly recommended for obtaining reliable memristors with high-performance.

7.3. Multi-Functionalities of Memristors

In general, electro-forming and current compliance (CC) are required for the stable RS operation of memristors.[371,393] However, these are undesirable for their commercial applications,[400] specifically data processing in health care,[367] neuromorphic computing,[367] and others, because of the requirement of a high electric field and additional CC devices for the controlling current in the devices.[367,400] Recently, memristors with multi functionalities, such as electro-forming free (EFF), self-compliance (SC), multi-bit, and ultra-low power, have been emerging topics for global researchers. The correlation between the defects and multifunctionality of the memristor was discussed here.

The EFF characteristics of memristors were achieved by the non-stoichiometry of the PIM RS layer (halides ion migration

Table 6. Comparison of the key performance parameters of lead-free perovskite-based memristors.

Switching Material	Set/Reset [V]	R_{on}/R_{off} ratio	Endurance Cycle (#)	Resistive switching (RS) mechanism (filament type)	Stability (Air/thermal/mechanical)	Multifunctionalities (Multi-bit, self-compliance (SC), Electroforming free)	Ref.
ITO/CsBi₃I₁₀/Al	−1.7/0.9	10^3	150	VCM (V_I-CFs)	60 days in the air (RT, RH = 60%)		[376]
Si/SiO₂/Ti-Pt/Cs₃Bi₂I₉/Au	0.1/−0.27	$>10^7$	400	VCM (V_I-CFs)	N/A	CC-based multi-bit	[371]
Si/SiO₂/Ti-Pt/Rb₃Bi₂I₉/Au	0.09/−0.24	10^7	200	VCM (V_I-CFs)	Stable up to 30 days in a vacuum	CC-based multi-bit	[371]
SiO₂/Ti-Pt/AgBi₂I₇-CsBi₂I₉/PMMA/Au	0.15/−0.07	10^7	10^3	ECM (Ag-CFs)	30 days in the air	CC-based multi-bit	[397]
SiO₂/Ti-Pt/((Cs₃Bi₂I₉)₀.₄−(CsPbI₃)₀.₆/PMMA/Au	0.15/−0.12	$>10^8$	10^3	ECM (Ag-CFs)	Stable upto 21 days in air, V_{set}/V_{reset} increases after 30 days	CC-based multi-bit	[378]
ITO/Cs₃Bi₂Br₉ QDs/Al	−0.45/2.2	10^5	50	VCM (V_{Br}-CFs)	200 days in air (RT, RH = 60%) thermal stability upto 360K	light-assisted multi-bit	[205]
ITO/MA₃Bi₂I₉/Au	1.6/−0.6	10^2	300	VCM (V_I-CFs)	150days in air (RT, RH = 50–60%)	CC-based multi-bit	[413]
FTO/(PMA)₂CuBr₄/PMMA/Al	1.6/−1.8	50	100	VCM	N/A		[384]
Si/SiO₂/Ti-Pt/(BzA)₂CuBr₄/PMMA/Ag	0.2/−0.3	10^8	2000	ECM (Ag-CFs)	Stable 14 days in the glove box, thermal stability upto 358K	CC-based multi-bit	[206]
ITO/Cs₃Cu₂I₅/Al	−0.46/0.32	65	200	VCM (V_I-CFs)	N/A	CC-based multi-bit	[414]
ITO/Cs₃Cu₂I₅/PMMA/Ag	0.5/−0.7	10^2	100	ECM (Ag-CFs)	N/A		[415]
ITO/Cs₃Cu₂Br₅/Al	0.45/−0.39	10^2	100	ECM (Al-CFs)-VCM(V_{Br}-CFs)	Stable in high RH (40–80%)	CC-based multi-bit	[416]
ITO/Cu₃SbI₆/PMMA/Ag	0.71/−0.71	10^2	422	ECM (Ag-CFs)-VCM (V_I-CFs)	N/A		[393]
ITO/Cu₂AgSbI₆/PMMA/Ag	0.71/−0.74	10^2	1600	ECM (Ag-CFs)-VCM (V_I-CFs)	75 days in air (RT, RH = 40–60%)	V_{stop} and CC-based multi-bit	[393]
ITO/CuAg₂SbI₆/PMMA/Ag	0.91/−1.02	10^2	330	ECM (Ag-CFs)-VCM (V_I-CFs)	N/A		[393]
ITO/Ag₃SbI₆/PMMA/Ag	1.00/−1.15	$>10^1$	199	ECM (Ag-CFs)-VCM (V_I-CFs)	N/A		[393]
ITO/Cu₃SbI₆/PMMA/Ag	0.5/−0.4	$>10^1$	400	ECM (Ag-CFs)-VCM (V_I-CFs)	60 days in ambient conditions		[391]
ITO/Cs₃Sb₂I₉/PMMA/Ag	−0.34/0.25	66	120	ECM (Ag-CFs)-VCM (V_I-CFs)	10 days in ambient atmosphere		[399]
ITO/Cs₂AgBiBr₆/Au	1.53/−3.40	10	10^3	ECM(Ag-CFs)-VCM (V_{Br}-CFs)	100days (RH = 10–80%) thermal stability upto 403K	CC-based multi-bit	[394]
ITO/Cs₂AgBiBr₆/PMMA/Ag	–	10	110	ECM(Ag-CFs)-VCM(V_I-CFs)	N/A	light-assisted multi-bit	[417]
ITO/Cs₂AgBiBr₆/Pt	–	500	–	VCM	N/A		[418]
ITO/Cs₂AgBiBr₆/Au	0.6/−0.45	$>10^2$		VCM (V_{Br}-CFs)	N/A	V_{reset} and CC based multi bit	[409]
ITO/Cs₂AgSbBr₆/PMMA/Ag	0.5/−0.5	300	230	ECM(Ag-CFs)-VCM(V_{Br}-CFs)	N/A		[395]
Si/SiO₂/Ti-Pt/BA₂CsAgBiBr₇/PMMA/Ag	0.13/−0.2	10^7	1000	ECM(Ag-CFs)-VCM(V_I-CFs)	22 days in air (RT, RH = 30–50%) thermal stability upto 358K	CC-based multi-bit	[207]

(Continued)

Table 6. (Continued).

Switching Material	Set/Reset [V]	R_{on}/R_{off} ratio	Endurance) Cycle (#)	Resistive switching (RS) mechanism (filament type)	Stability — Air/ thermal/ mechanical	Multifunctionalities — Multi-bit,) self-compliance (SC),) Electroforming free	Ref.
ITO/Cs_2NaBiI_6 /Al	−0.3/2.3	10^2	200	VCM(V_I-CFs)	90 days, stable upto 403K	Multi-bit,) self-compliance (SC),) Electroforming free	[412]
ITO/$Cs_2AgEuBr_6$/Au	3.5/−1.5	10^4	100	ECM(Ag-CFs)-VCM(V_{Br}-CFs)	N/A		[419]
ITO/$Cs_2AgInCl_6$/Au	≈1/−1	$>10^2$	1000	VCM(V_{Cl}-CFs)	7 days in the air		[420]
ITO/$MASnBr_3$/Au	0.65/−3.1	10–10^3		VCM(V_{Br}-CFs)	thermal stability upto 358K	V_{reset} based multi bit	[396]
Flexible memristors							
PET/ITO / Cu_3SbI_6/PMMA/Ag	0.5/−0.4	$>10^1$	400	ECM(Ag-CFs)-VCM(V_I-CFs)	Bending 1000 cycles		[391]
PET/ITO / Cu_2AgSbI_6/PMMA/Ag	0.71/−0.74	10^2	1600	ECM(Ag-CFs)-VCM(V_I-CFs)	N/A	N/A	[393]
COP/Ti-Pt / $Cs_3Bi_2I_9)_{0.4}$−$(CsPbI_3)_{0.6}$ /PMMA/Au	0.15/−0.12	$>10^8$	10^2	ECM (Ag CFs)	Stable upto 21 days in air, V_{set}/V_{reset} increases after 30 days	N/A	[378]
PEN/ITO / $AgBiI_4$ /PMMA/Au	0.16/−0.16	10^2	1000	ECM(Ag-CFs)	Bending 1000 cycles	N/A	[392]
PET/ITO /$Cs_3Bi_2Br_9$ QDs/Al	−0.45/2.2	10^5	100	VCM (V_{Br} -CFs)		light-assisted multi-bit	[205]
PET/ITO/$Cs_2AgBiBr_6$/Au	1.53/−3.40	10	10^3	VCM (V_{Br} -CFs)	Bending 10000 cycles, thermal stability upto 373 K	N/A	[394]
PET/ITO/$Cs_2AgSbBr_6$/PMMA/Ag	0.85/−0.5	200	230	ECM(Ag-CFs)-VCM(V_{Br} –CFs)	Bending 1000 cycles	N/A	[395]
PET/ITO/PVA/ $CH_3NH_3SnCl_3$/Al	1.6/−1.8	$>10^3$	N/A	ECM-VCM	Bending 2000 cycle	N/A	[370]
PET/ITO/$MASnBr_3$/Au	0.65/−3.1	10–10^3	120	VCM (V_{Br} -CFs)	1000 bending cycle	N/A	[396]
PET/ITO/$Cs_3Sb_2I_9$/PMMA/Ag	−0.34/0.25	66		ECM(Ag-CFs)-VCM (V_I -CFs)	1000 bending cycle		[399]
Electroforming free (EFF) and self-compliance (SC) based memristors							
PET/ITO/$Cs_3Bi_2I_9$/Au	0.3/−0.5	90	10^4	VCM(V_I-CFs)	30 days, bending 100 cycles	electroforming free	[375]
Si/SiO_2/Ti-Pt/ $Rb_3Bi_{1.8}Na_{0.2}I_{8.6}$ /Au	0.09/−0.24	10^7	100	VCM (V_I- Na″$_{Bi}$ CFs)	N/A	electroforming free	[371]
ITO (BE)/$Cs_3Sb_2I_9$/Al (TE)	0.39/−2.91	10^4	100	VCM (Sb+V_I -CFs)	N/A	EFF and SC	[380]
ITO/$Cs_2AgBiBr_6$/Al	−0.40/1.55	10^3	100	VCM(V_{Br} –CFs)	N/A	electroforming free	[381]
ITO/Cs_2AgBi_5Cl/Al	−0.21/1.34	10^4	100	VCM (V_{Br}-V_{Cl}- CFs)	Stable in 100 days in air, thermal stability upto 358K	electroforming free	[381]
ITO /$Cs_3Sb_2I_9$/Al	0.67/−1.8	10	750	VCM (V_I-CFs)	100 days in air	Self-compliance (SC)	[382]
ITO /$Cs_3Sb_2Br_9$/Al	0.32/−0.98	30	750	VCM (V_{Br}-CFs)	N/A	Self-compliance (SC)	[382]
ITO /$Cs_3Sb_2Cl_9$/Al	0.11/−0.56	10^2	750	VCM (V_{Cl}-CFs)	N/A	Self-compliance (SC)	[382]
ITO / $Cs_3Bi_2I_6Cl_3$ /Al	−0.18/1.36	10^3	500	VCM (V_I-V_{Cl}- CFs)	N/A	Self-compliance (SC)	[405]
ITO / $Cs_3Bi_2I_9$/Al	0.22/−0.42	10^4	400	VCM (V_I-CFs)	N/A	Self-compliance (SC)	[383]

(Continued)

Table 6. (Continued).

Switching Material	Set/Reset [V]	R_{on}/R_{off} ratio	Endurance) Cycle (#)	Resistive switching (RS) mechanism (filament type)	Stability) Air/thermal/mechanical	Multifunctionalities: Multi-bit) self-compliance (SC),) Electroforming free	Ref.
ITO/Cs$_3$Bi$_2$Br$_9$/Al	0.67/−1.21	10	400	VCM (V$_{Br}$-CFs)	N/A	Self-compliance (SC)	[383]
ITO/Cs$_3$Bi$_2$Cl$_9$/Al	0.44/−0.97	10^2	400	VCM (V$_I$-CFs)	N/A	Self-compliance (SC)	[383]
ITO/Cs$_3$Bi$_2$Br$_9$/Ag	−0.5/1	10	3200	Interface face	7 days in air (RT, RH = 40%)	Self-compliance (SC) light-assisted multi-bit	[403]
FTO/CsBi$_3$I$_{10}$-AgO$_x$/Ag	−0.14/0.5	10^6	250	VCM (V$_I$-CFs)	thermal stability upto 290K	Self-compliance (SC), CC-based multi-bit	[379]
FTO/Cs$_3$Bi$_2$I$_9$-AgO$_x$/Ag	−0.12/1.0	10^6	250	VCM (V$_I$-CFs)	thermal stability upto 290K	Self-compliance (SC) CC-based multi-bit	[379]
ITO/Cs$_3$Bi$_2$Br$_9$/Ag	0.45/−0.38	10^2	10^4	Interface (V$_{Br}$)	37 days in air (RT, RH = 50%)	SC, CC-based multi-bit	[377]
ITO/MA$_3$Bi$_2$I$_9$/Cu	1/−6.4	10^4	1730	ECM (Cu-CFs)		SC, light-assisted, and CC-based multi-bit	[404]

and the presence of defects),[400] defect manipulation,[381,400] metal doping,[371] variation of active layer thickness.[401] For instance, Na incorporation into Rb$_3$Bi$_2$I$_9$[371] and substitution of Cl into Cs$_2$AgBiBr$_6$ RS layers[381] generate more defects (V$_I$ for Rb$_3$Bi$_{1.8}$Na$_{0.2}$I$_{8.6}$ and V$_{Br}$, V$_{Cl}$ for Cs$_2$AgBi$_5$Cl), thus leads to EFF characteristics of the memristors.[381] Furthermore, the reduction of interstitial Sb^{3+} to metallic Sb by the movement of a V$_{Br}$/V$_I$ in the MA$_3$Sb$_2$Br$_9$ / Cs$_3$Sb$_2$I$_9$ and RS layer is correlated with the EFF-RS properties of memristors.[380,400] According to previously reported literature, external doping of metal ions or internal conversion of metal state cations via halide vacancies generates more defects in the lead-free PIM RS layer, responsible for EFF characteristics of the memristors.[380,381,400] However, the underlying physics behind the EFF of the memristor is not well understood, and further studies are required to find its origin. The progress in the performance of Cs$_3$Bi$_2$I$_9$,[375] Rb$_3$Bi$_{1.8}$Na$_{0.2}$I$_{8.6}$,[371] Cs$_3$Sb$_2$I$_9$,[380] MA$_3$Sb$_2$Br$_9$,[400] (CH$_3$NH$_3$)$_3$Bi$_2$I$_9$,[402] Cs$_2$AgBiBr$_6$,[381] and Cs$_2$AgBi$_5$Cl[381] based memristors with EFF characteristics are summarized in Table 6.

Recently, Bi-based (Cs$_3$Bi$_2$I$_9$,[379] CsBi$_3$I$_{10}$,[379] Cs$_3$Bi$_2$Br$_9$[403]) and antimony-based (Cs$_3$Sb$_2$I$_9$[380] and MA$_3$Sb$_2$Br$_9$[400]) and other RS layers-based memristor devices[382,383,404,405] were under switching operation without CC represent their self-compliance characteristics (SCCs) (Table 6). The higher V$_{set}$/V$_{reset}$ value of SCC-based memristors was observed compared with devices with CC (Figure 21h).[393,406] The SCCs indicate the built-in current overshoot reduction capability of the memristor, thus simplifying device circuit design without any additional current-limiting devices.[379,380,400,403] The SCCs of Bi and the Sb-based devices might originate from intrinsic defects, non-stoichiometric chemical composition, interfacial defects (Br$^−$/I$^−$ and V$_{Br}$/V$_I$), and high potential barrier at the metal electrodes (BE or TE) /RS layer interface.[379,380,382,383,400,403,404,405,407,408] The progress in self-compliance-based memristor lead and PIM layer as RS layer is summarized in Table 6. Based on previously reported literature, the SCCs are partially associated with the VCM switching mechanism in the memristors (Table 6). However, further studies are essential for understanding the origin of SCCs in the emerging PIM RS layers for memristor devices.

The multi-level resistive states (multi-bit memory) of PIM RS layer-based memristor can be achieved by modulating the current compliance (CC)[205–207,377,371,397,402,404,393,400,409] or stop voltage (V$_{stop}$)[393] during the set process, tuning of V$_{reset}$ during the reset process,[396,409] and under the illumination of light with varying intensities.[205,404,410] The CC-based multi-level resistive states were observed in most of the reported literature on lead-free PIM RS layer-based memristors (Table 6). The increase in V$_{reset}$ value and different LRS states were observed for CC-based devices (Figure 21i).[411] The rise in V$_{reset}$ values and multiple LRS states with increased CC values are ascribed to the change in size and shape of CFs and the formation of several CFs.[371,393] The lower CCs lead to a lower LRS state resistance and smaller V$_{reset}$ and vice versa.[393] As per previous reports, the multi-level resistances originated from intrinsic and processing-dependent defects (halide vacancy, surface defects, and others), acting as charge-trapping sites in the RS layer[205–207,371,377,393,396,397,400,402,404,409] The multi-level resistances (multi-bit) memristors are helpful in circuit complexity simplification and have potential applications in high-density data

storage for next-generation computing systems.[205,371,400] The stability of a lead-free PIM RS layer is essential for obtaining reliable high-performance memristors.[338,349,381] All the previously reported inorganic lead-free Cu-,[356] Bi-, Ag-, and Sb-based PIM RS layers-based memristors were environmentally stable over >20 days[349] and operationally working conditions up to 358K[381] (Figure 21j, Al/Cs_2NaBiI_6/ITO device, Table 6), thus attributable to their structural stability over several months in ambient conditions.[349,356,381] On the other hand, the decreased R_{on}/R_{off} ratio value with increased temperature ascribes to the thermal activation of defects (V_I) (Figure 21j), thus leading to an increase in HRS current (Figure 21k).[412]

8. Conclusions and Outlook

In terms of optoelectronic properties and device performance, PIMs are lagging behind the conventional lead halide analogs, but they possess high potential for emerging applications, such as IPVs. Unlike LHPs, one of the setbacks of the wide-bandgap PIMs is the presence of high defect densities. We reviewed relevant studies on the defect properties of various families of PIMs, in turn providing a comprehensive picture of the chemical origin of defects, their nature (deep or shallow), density, and capture cross-section. We then correlated the influence of the defects on the material and device characteristics of the PIMs like charge carrier lifetime and V_{OC}, respectively. The defect mitigation pathways were also discussed. Finally, we summarized the state-of-the-art performance of the PIMs in outdoor and indoor photovoltaics, self-powered photodetectors, and memristors, and discussed the influence of defects and other factors restricting their device efficiencies, which still lie far below the theoretical limits. As follows, we provide our views on the future directions and potential solutions for the rapid advancement of the research on wide-bandgap PIMs.

1) In Section 3, we highlighted the rich and complex defect chemistry of PIMs. Further work is needed to better understand the role of defects in many of these emerging materials, and therefore rationally develop approaches to mitigate their effects. It will be important to approach this from both an experimental and computational perspective. Detailed measurements of the recombination centers in PIMs (e.g., through DLTS, PICTS, or FPTS) are needed, and correlated with defect calculations to help identify the origins of these defects. At the same time, simulating the defects present in materials is complicated by the complex chemistry of these materials, which often involve many elements, and, in the case of Ag-Bi-I and Cu-Ag-Bi-I semiconductors, involves cation disorder. Furthermore, as discussed in Section 3.1.3, accurately determining the energies of transition levels of defects is challenging, depending on the level of theory used, and this can be further complicated by the need to also account for Van der Waals interactions in these materials, many of which are low dimensional. It will also be important to establish the level of local dynamic disorder in PIMs. In LHPs, high levels of local dynamic disorder significantly complicate the accurate determination of the capture coefficient of defects, which often cannot be judged simply from the position of the transition

level to the band-edges. But whether similar challenges exist with fully inorganic PIMs remains to be established.

2) Further understanding the defects present in materials will not only be important to identify routes to improve them, it will also allow progress to be made to understand defect tolerance. As can be seen in Section 3.1, there is still significant debate within the community about why LHPs have exceptional optoelectronic properties, despite being processed by simple solution processing. A sizeable fraction of the community believes that this is due to most traps being shallow with low capture cross-sections (defect tolerance), but many others believe that it is due to self-healing (reduction in defect density after defect formation), or simply due to a low defect density being present. In PIMs, there is evidence among a small handful of materials for defect tolerance and self-healing, and it has also been possible to grow PIM single crystals with low defect densities. While it is clear so far that defect tolerance is not universally found in PIMs, there is still hope that tolerance to at least a selection of dominant defects can be found and identified through chemical and structural descriptors, such as the orbital composition of the band-extrema or lattice parameters.

3) As discussed in Section 3.1.3, the capture cross-sections can be increased (and traps become more detrimental) in wide-bandgap semiconductors due to the optical dielectric constant decreasing as bandgap increases. An approach to address this could be to find materials with a large ionic dielectric constant, since it was found that this was decoupled to changes in bandgap. This may be found in materials with highly polarization cations, or materials close to a polar phase transition, and could balance the effects of the decrease in optical dielectric constant.[80] However, a larger difference between static and optical dielectric constants would result in stronger coupling between charge-carriers and longitudinal optical phonons, which can reduce mobilities, and potentially also cause self-trapping if the coupling becomes strong.

4) As discussed in Section 3.3, there are a wide range of routes to mitigate the effects of deep recombination centers, such as through doping and heteroepitaxial passivation. Future efforts should expand upon these more generally among PIMs, and draw further inspiration from successful strategies made in LHPs. For example, Cl doping is thought to passivate defects, but it should be considered whether Cl (and Br) passivation can shift defect formation energies to higher values, as found for LHPs.[421] Further work is also needed to understand the role of H dopants in PIMs. For $Cs_2AgBiBr_6$, H-doping led to improved photocurrents through a reduction in the bandgap.[96] But is not clear whether H-doping could play a broader role by passivating dangling bonds, as they do in silicon.[422] Furthermore, whilst the H interstitial was found computationally to act as a deep defect in $CsPbBr_3$, it is not clear whether such impurities can easily migrate and passivate other defects, and therefore play a more beneficial role.[75,423] There is therefore a rich diversity of future opportunities to mitigate the effects of defects and improve the performance of PIMs.

5) The nature of ion migration is not a well-explored research topic in PIM devices. Defects aid ion migration (i.e., migration of defects) and grain boundary-driven ion migration

**ADVANCED
SCIENCE NEWS**

www.advancedsciencenews.com

**ADVANCED
FUNCTIONAL
MATERIALS**

www.afm-journal.de

under operation have been shown to cause irreversible damage to device performance and lead to J–V hysteresis in LHPs, and the corresponding mitigation pathways have also been proposed.[424–428] Such ion migration effects are anticipated to significantly impact the performance and stability of the devices employing PIMs because these materials possess high defect density and film morphologies typically inferior to LHPs. This may be one of the reasons for the poor operational stability observed in Bi/Sb PIM-based photovoltaic devices.[429] Unfortunately, the origin of ion migration and its influence on the device characteristics of wide-bandgap PIMs have still not been given the necessary attention, with a limited set of studies thus far.[430,431]

6) As discussed in section 5.3, the sub-par photovoltaic performance of PIMs is majorly due to deficits in J_{SC} and V_{OC}, majorly contributed by carrier-phonon coupling, limited selection for metal contacts and charge transport layers, and non-radiative recombination losses.[69,99,432] Carrier-phonon coupling may be suppressed by modifying the local structural distortion. On the other hand, the typical sub-standard morphologies of perovskite-inspired absorbers with pin holes and small crystal grains lead to high bulk recombination losses, which, in turn, causes a high V_{OC} deficit. Therefore, film morphologies of PIMs may be improved by controlling the crystallization process or adapting other strategies known to be successful on LHPs. Since high shunt resistance minimizes voltage losses at very low-light intensities, high-quality PIM absorber layers with negligible shunt pathways are a prerequisite for achieving photovoltaic efficiencies close to the very high theoretical limit of 50–60%. Even in the case of defect-tolerant PIMs such as BiOI, the film morphology has not been fully optimal, which alongside the charge carrier coupling, does not allow us to realize its true potential in photovoltaics. Furthermore, in addition to screening the existing ETL and HTL and designing new and suitable candidates for efficient charge carrier extraction in PIM-based devices, surface/interface passivation strategies should be employed to suppress the V_{OC} losses. It should be noted that the minimization of undesired recombination at the device interfaces contributed to the significant improvement in both PCE and operational stability of the high-performance LHP solar cells.[433] Despite the impressive stability of PIMs (under ambient air, moisture, and high temperatures), their device operational stabilities have been overlooked so far, which is known to depend on various factors such as absorber layer quality and its surface passivation, defect density, moisture infiltration due to hydrophilic dopants in HTL, and ion migration.[434] Operational stability should also be given equal priority as efficiency improvement.

7) As outlined in section 6, the operational stability (environmental and thermal) and performance of the PIM photoactive layers-based SPPDs can be further improved by optimizing the chemical composition, morphology, and thickness of the PIM films, minimizing the charge recombination at interfaces (metal/ETL or HTL or PIM/ETL or HTL), and developing an effective device encapsulation.[40,201–204,334,341,343,349,358,359,360–363] In addition, the lead-free PIM photoactive layers have been so far implemented in SPPDs for only UV and visible light detection,

with a few reports available for flexible SPPDs (Table 5). We suggest the focus on the following aspects to improve the performance and stability (thermal and mechanical) of SPPDs and their fabrication on flexible substrates:

i) Ionic liquids as solvents to control the morphology[435] or as additives may improve the crystallinity, reduce the process temperature of the PIM layer,[191] and passivate intrinsic[192] and interfacial defects[193,436] in devices, in turn enabling efficient and stable SPPDs.

ii) Polymer scaffolds, such as PEG,[437] PVA,[438] are known to improve the surface coverage and morphology,[437,438] control the phase of perovskites[439] and their grain size,[438] passivate the surface defects,[439] in turn enhancing the mechanical[440] and environmental stability of SPPDs.[437,440] The polymer scaffold protocol can be, thus, one of the best methods for fabricating high-performance flexible SPPDs.

iii) Proper design/selection of HTL/ETL to match the PIM active layers is vital for improving the performance of SPPDs.[195,188] For instance, the Cu_2AgBiI_6-based SPPDs (ITO/SnO$_2$/Cu_2AgBiI_6/HTL/Ag) fabricated with P3HT HTL displayed higher PDPs and faster t_r/t_d time as compared to Spiro-OMeTAD based devices.[195]

iv) The surface treatment of SPPDs with functional molecules, such as thiophene-2-carbohydrazide (TAH),[357] additive 4-amino-2, 3, 5, 6-tetra fluoro benzoic acid (ATFBA),[338] N-(2-aminoethyl) acetamide,[441] phenethylammonium iodide (PEAI),[195] and L-ascorbic acid, is one of the most effective ways to passivate nonradiative recombination sites (defects at the surface or grain boundary) and reduce defect density in perovskite films.[357] The surface-treated perovskite films become hydrophobic and form a barrier against ambient moisture,[195] hence this treatment may also contribute to enhanced moisture stability of SPPDs.[195]

8) As discussed in Section 7, ultralow operating voltage (V_{set}/V_{reset}), self-compliance, electroforming, and multi-bit are attractive properties of PIM-based (RS-type) memristors. However, the origin of these multi-functionalities of the memristors has been under debate, and further studies are required to comprehend these properties. Despite the decent progress on PIM-based memristors on rigid and flexible substrates, their performance is inferior to LHPs and other materials. The following aspects need to be addressed to enhance the performance and stability of memristors for their real-time applications:

i) The retention, endurance, consistent performance (device-to-device and cycle-to-cycle), stability, and power consumption of memristors are crucial for their practical applications. The lower endurance of PIM-based memristors compared to LHPs and perovskite oxides is a consequence of a high surface roughness of the PIM layer; thus, optimization of its surface coverage and roughness, and grain size is necessary to improve the endurance properties.

ii) A flexible memristor is a critical component for wearable electronic devices, which have potential applications

in healthcare and IoT. The degradation in RS properties of the memristors under high mechanical stress (at a bending radius <5 mm) was speculated due to the formation of the cracks in the PIM layer and delamination of the electrode|PIM interface. A detailed investigation is required to understand the origin of the degradation in RS properties.

iii) The PIMs show excellent optical properties, and constructing a multi-bit, high-performance photo memristor by selecting a suitable PIM RS layer is essential for their implementation in emerging applications like logic operations, neuromorphic computing, and artificial visual system.

iv) The patterning of PIM RS layers is vital for system-level implementation (cross-bar-array memristors). The degradation of the PIM RS layers during the conventional lithography process might cause a high Sneak current and an obstacle to develop cross-bar-arrays-based memristors. In addition to existing patterning techniques, such as dry etching-based lithography and polymer assist patterning, integrating threshold memristor and memristor (1S-1R), transistor and memristor (IT-1R) device configurations may minimize Sneak current paths in the cross-bar-array memristors.

In conclusion, the research on wide bandgap PIMs is in its early infancy and the full potential of these low-toxicity and air-stable semiconductors is yet to be realized for high-performance photovoltaics and other optoelectronics. We believe the thorough understanding of the defect chemistry is the key to overcome the challenges that still limit the performance and the operational stability of PIM-based devices. We hope that this work will inspire new material and device engineering strategies to boost the competitivity of PIMs for sustainable light harvesting and beyond.

Acknowledgements

Conflict of Interest

The authors declare no conflict of interest.

Author Contributions

Keywords

[1] J. Park, J. Kim, H.-S. Yun, M. J. Paik, E. Noh, H. J. Mun, M. G. Kim, T. J. Shin, S. Il Seok, *Nature* **2023**, *616*, 724.

[2] *Best Research-Cell Efficiency Chart | Photovoltaic Research | NREL* (accessed: September 2023).

[3] J. Li, J. Dagar, O. Shargaieva, O. Maus, M. Remec, Q. Emery, M. Khenkin, C. Ulbrich, F. Akhundova, J. A. Márquez, *Adv. Energy Mater.* **2023**, 2203898.

[4] J. Li, H.-L. Cao, W.-B. Jiao, Q. Wang, M. Wei, I. Cantone, J. Lü, A. Abate, *Nat. Commun.* **2020**, *11*, 310.

[5] A. Abate, *Joule* **2017**, *1*, 659.

[6] C. Ponti, G. Nasti, D. Di Girolamo, I. Cantone, F. A. Alharthi, A. Abate, *Trends Ecol. Evol.* **2022**.

[7] H. Zhang, J.-W. Lee, G. Nasti, R. Handy, A. Abate, M. Grätzel, N.-G. Park, *Nature* **2023**, *617*, 687.

[8] Q. A. Akkerman, L. Manna, *ACS Energy Lett.* **2020**, *5*, 604.

[9] Y.-T. Huang, S. R. Kavanagh, D. O. Scanlon, A. Walsh, R. L. Z. Hoye, *Nanotechnology* **2021**, *32*, 132004.

[10] C. C. Stoumpos, C. D. Malliakas, M. G. Kanatzidis, *Inorg. Chem.* **2013**, *52*, 9019.

[11] W. Shockley, H. J. Queisser, *J. Appl. Phys.* **1961**, *32*, 510.

[12] N. Glück, T. Bein, *Energy Environ. Sci.* **2020**, *13*, 4691.

[13] V. Pecunia, L. G. Occhipinti, A. Chakraborty, Y. Pan, Y. Peng, *APL Mater.* **2020**, *8*, 100901.

[14] H. Fu, *Sol. Energy Mater. Sol. Cells* **2019**, *193*, 107.

[15] F. Ünlü, M. Deo, S. Mathur, T. Kirchartz, A. Kulkarni, *J. Phys. D Appl. Phys.* **2021**, *55*, 113002.

[16] N. R. Wolf, B. A. Connor, A. H. Slavney, H. I. Karunadasa, *Angew. Chem., Int. Ed.* **2021**, *133*, 16400.

[17] U. V Ghorpade, M. P. Suryawanshi, M. A. Green, T. Wu, X. Hao, K. M. Ryan, *Chem. Rev.* **2023**, *123*, 327.

[18] B. Vargas, G. Rodríguez-López, D. Solis-Ibarra, *ACS Energy Lett.* **2020**, *5*, 3591.

[19] A. Chakraborty, N. Pai, J. Zhao, B. R. Tuttle, A. N. Simonov, V. Pecunia, *Adv. Funct. Mater.* **2022**.

[20] S. Ghosh, H. Shankar, P. Kar, *Mater. Adv.* **2022**, *3*, 3742.

[21] E. T. McClure, M. R. Ball, W. Windl, P. M. Woodward, *Chem. Mater.* **2016**, *28*, 1348.

[22] Y.-J. Li, T. Wu, L. Sun, R.-X. Yang, L. Jiang, P.-F. Cheng, Q.-Q. Hao, T.-J. Wang, R.-F. Lu, W.-Q. Deng, *RSC Adv.* **2017**, *7*, 35175.

[23] G. Meyer, *Z. Naturforsch. B* **1980**, *35*, 394.

[24] S. E. Creutz, E. N. Crites, M. C. De Siena, D. R. Gamelin, *Nano Lett.* **2018**, *18*, 1118.

**ADVANCED
SCIENCE NEWS**

www.advancedsciencenews.com

**ADVANCED
FUNCTIONAL
MATERIALS**

www.afm-journal.de

[25] E. Oomen, G. J. Dirksen, W. M. A. Smit, G. Blasse, *Met. Phys.* **1987**, *20*, 1161.

[26] Y. Sun, A. J. Fernandez-Carrion, Y. Liu, C. Yin, X. Ming, B.-M. Liu, J. Wang, H. Fu, X. Kuang, X. Xing, *Chem. Mater.* **2021**, *33*, 5905.

[27] P. Carmona-Monroy, B. Vargas, D. Solis-Ibarra, in *Low-Dimensional Halide Perovskites Structure, Synthesis, and Applications* (Eds.: Y. Zhan, M. Khalid, P. Vivo, N. Arshid), Elsevier, **2023**, pp. 447–475.

[28] Y. Liu, I. J. Cleveland, M. N. Tran, E. S. Aydil, *J. Phys. Chem. Lett.* **2023**, *14*, 3000.

[29] L. Mao, S. M. L. Teicher, C. C. Stoumpos, R. M. Kennard, R. A. DeCrescent, G. Wu, J. A. Schuller, M. L. Chabinyc, A. K. Cheetham, R. Seshadri, *J. Am. Chem. Soc.* **2019**, *141*, 19099.

[30] H. A. Evans, L. Mao, R. Seshadri, A. K. Cheetham, *Annu. Rev. Mater. Res.* **2021**, *51*, 351.

[31] X.-G. Zhao, D. Yang, J.-C. Ren, Y. Sun, Z. Xiao, L. Zhang, *Joule* **2018**, *2*, 1662.

[32] B. A. Connor, L. Leppert, M. D. Smith, J. B. Neaton, H. I. Karunadasa, *J. Am. Chem. Soc.* **2018**, *140*, 5235.

[33] B. Saparov, J.-P. Sun, W. Meng, Z. Xiao, H.-S. Duan, O. Gunawan, D. Shin, I. G. Hill, Y. Yan, D. B. Mitzi, *Chem. Mater.* **2016**, *28*, 2315.

[34] Y. Xu, B. Jiao, T.-B. Song, C. C. Stoumpos, Y. He, I. Hadar, W. Lin, W. Jie, M. G. Kanatzidis, *ACS Photonics.* **2018**, *6*, 196.

[35] M.-G. Ju, M. Chen, Y. Zhou, H. F. Garces, J. Dai, L. Ma, N. P. Padture, X. C. Zeng, *ACS Energy Lett.* **2018**, *3*, 297.

[36] S. Nobuya, H. A. Abbas, N. Simantini, R. Alexandra, W. Zhiping, G. Feliciano, H. J. Snaith, *J. Am. Chem. Soc.* **2017**, *139*, 6030.

[37] Z. Xiao, Y. Zhou, H. Hosono, T. Kamiya, *Phys. Chem. Chem. Phys.* **2015**, *17*, 18900.

[38] B. Lee, C. C. Stoumpos, N. Zhou, F. Hao, C. Malliakas, C.-Y. Yeh, T. J. Marks, M. G. Kanatzidis, R. P. H. Chang, *J. Am. Chem. Soc.* **2014**, *136*, 15379.

[39] R. Waykar, A. Bhorde, S. Nair, S. Pandharkar, B. Gabhale, R. Aher, S. Rondiya, A. Waghmare, V. Doiphode, A. Punde, *J. Phys. Chem. Solids* **2020**, *146*, 109608.

[40] W. Li, Y. Liu, Y. Gao, Z. Ji, Y. Fu, C. Zhao, W. Mai, *J. Mater. Chem. C* **2021**, *9*, 1008.

[41] T. D. Chonamada, A. B. Dey, P. K. Santra, *ACS Appl. Energy Mater.* **2020**, *3*, 47.

[42] S. W. Kim, R. Zhang, P. S. Halasyamani, M. A. Hayward, *Inorg. Chem.* **2015**, *54*, 6647.

[43] B. Vargas, E. Ramos, E. Pérez-Gutiérrez, J. C. Alonso, D. Solis-Ibarra, *J. Am. Chem. Soc.* **2017**, *139*, 9116.

[44] B. Vargas, D. T. Reyes-Castillo, E. Coutino-Gonzalez, C. Sánchez-Aké, C. Ramos, D. Falcony, D. Solis-Ibarra, *Chem. Mater.* **2020**, *32*, 9307.

[45] H. C. Sansom, G. F. S. Whitehead, M. S. Dyer, M. Zanella, T. D. Manning, M. J. Pitcher, T. J. Whittles, V. R. Dhanak, J. Alaria, J. B. Claridge, *Chem. Mater.* **2017**, *29*, 1538.

[46] H. C. Sansom, L. R. V Buizza, M. Zanella, J. T. Gibbon, M. J. Pitcher, M. S. Dyer, T. D. Manning, V. R. Dhanak, L. M. Herz, H. J. Snaith, *Inorg. Chem.* **2021**, *60*, 18154.

[47] T. Oldag, T. Aussieker, H. Keller, C. Preitschaft, A. Pfitzner, *Z. Anorg. Allg. Chem.* **2005**, *631*, 677.

[48] I. Turkevych, S. Kazaoui, E. Ito, T. Urano, K. Yamada, H. Tomiyasu, H. Yamagishi, M. Kondo, S. Aramaki, *ChemSusChem* **2017**, *10*, 3754.

[49] V. W. Rüdorff, H. Becker, *Z. Naturforsch* **1954**, *9b*, 613.

[50] Y. Kim, Z. Yang, A. Jain, O. Voznyy, G. Kim, M. Liu, L. N. Quan, F. P. García de Arquer, R. Comin, J. Z. Fan, *Angew. Chem. Inte. Ed.* **2016**, *55*, 9586.

[51] H. C. Sansom, G. Longo, A. D. Wright, L. R. V Buizza, S. Mahesh, B. Wenger, M. Zanella, M. Abdi-Jalebi, M. J. Pitcher, M. S. Dyer, *J. Am. Chem. Soc.* **2021**, *143*, 3983.

[52] M. Bernechea, N. Cates, G. Xercavins, D. So, A. Stavrinadis, G. Konstantatos, *Nat. Photonics* **2016**, *10*, 521.

[53] Y. Wang, S. R. Kavanagh, I. Burgués-Ceballos, A. Walsh, D. O. Scanlon, G. Konstantatos, *Nat. Photonics* **2022**, *16*, 235.

[54] J. Li, S. Han, S. Guo, *Eur. J. Inorg. Chem.* **2022**, *2022*, e202200419.

[55] F. Palazon, *Sol. RRL* **2022**, *6*, 2100829.

[56] R. Nie, J. Im, S. Il Seok, *Adv. Mater.* **2019**, *31*, 1808344.

[57] W. Lin, C. C. Stoumpos, O. Y. Kontsevoi, Z. Liu, Y. He, S. Das, Y. Xu, K. M. McCall, B. W. Wessels, M. G. Kanatzidis, *J. Am. Chem. Soc.* **2018**, *140*, 1894.

[58] T. Li, X. Wang, Y. Yan, D. B. Mitzi, *J. Phys. Chem. Lett.* **2018**, *9*, 3829.

[59] S. Toso, Q. A. Akkerman, B. Martín-García, M. Prato, J. Zito, I. Infante, Z. Dang, A. Moliterni, C. Giannini, E. Bladt, *J. Am. Chem. Soc.* **2020**, *142*, 10198.

[60] A. Walsh, A. Zunger, *Nat. Mater.* **2017**, *16*, 964.

[61] S. B. Zhang, S.-H. Wei, A. Zunger, *Phys. Rev. Lett.* **1997**, *78*, 4059.

[62] W.-J. Yin, T. Shi, Y. Yan, *Appl. Phys. Lett.* **2014**, *104*, 063903.

[63] A. Zakutayev, C. M. Caskey, A. N. Fioretti, D. S. Ginley, J. Vidal, V. Stevanovic, E. Tea, S. Lany, *J. Phys. Chem. Lett.* **2014**, *5*, 1117.

[64] D. Meggiolaro, S. G. Motti, E. Mosconi, A. J. Barker, J. Ball, C. A. R. Perini, F. Deschler, A. Petrozza, F. De Angelis, *Energy Environ. Sci.* **2018**, *11*, 702.

[65] J. Ye, M. M. Byranvand, C. O. Martínez, R. L. Z. Hoye, M. Saliba, L. Polavarapu, *Angew. Chem., Int. Ed.* **2021**, *133*, 21804.

[66] R. E. Brandt, V. Stevanović, D. S. Ginley, T. Buonassisi, *MRS Commun.* **2015**, *5*, 265.

[67] D. Cahen, L. Kronik, G. Hodes, *ACS Energy Lett.* **2021**, *6*, 4108.

[68] W. Shockley, W. T. Read Jr., *Phys. Rev.* **1952**, *87*, 835.

[69] S. R. Rondiya, R. A. Jagt, J. L. MacManus-Driscoll, A. Walsh, R. L. Z. Hoye, *Appl. Phys. Lett.* **2021**, *119*, 220501.

[70] L. R. V Buizza, L. M. Herz, *Adv. Mater.* **2021**, *33*, 2007057.

[71] B. Wu, W. Ning, Q. Xu, M. Manjappa, M. Feng, S. Ye, J. Fu, S. Lie, T. Yin, F. Wang, *Sci. Adv.* **2021**, *7*, eabd3160.

[72] Y.-T. Huang, S. R. Kavanagh, M. Righetto, M. Rusu, I. Levine, T. Unold, S. J. Zelewski, A. J. Sneyd, K. Zhang, L. Dai, *Nat. Commun.* **2022**, *13*, 4960.

[73] R. E. Brandt, J. R. Poindexter, P. Gorai, R. C. Kurchin, R. L. Z. Hoye, L. Nienhaus, M. W. B. Wilson, J. A. Polizzotti, R. Sereika, R. Zaltauskas, *Chem. Mater.* **2017**, *29*, 4667.

[74] A. M. Ganose, C. N. Savory, D. O. Scanlon, *Chem. Commun.* **2017**, *53*, 20.

[75] X. Zhang, M. E. Turiansky, J.-X. Shen, C. G. Van de Walle, *J. Appl. Phys.* **2022**, *131*, 090901.

[76] A. V Cohen, D. A. Egger, A. M. Rappe, L. Kronik, *J. Phys. Chem. Lett.* **2019**, *10*, 4490.

[77] D. P. Nenon, K. Pressler, J. Kang, B. A. Koscher, J. H. Olshansky, W. T. Osowiecki, M. A. Koc, L.-W. Wang, A. P. Alivisatos, *J. Am. Chem. Soc.* **2018**, *140*, 17760.

[78] K. X. Steirer, P. Schulz, G. Teeter, V. Stevanovic, M. Yang, K. Zhu, J. J. Berry, *ACS Energy Lett.* **2016**, *1*, 360.

[79] S. Heo, G. Seo, Y. Lee, D. Lee, M. Seol, J. Lee, J.-B. Park, K. Kim, D.-J. Yun, Y. S. Kim, *Energy Environ. Sci.* **2017**, *10*, 1128.

[80] A. M. Ganose, D. O. Scanlon, A. Walsh, R. L. Z. Hoye, *Nat. Commun.* **2022**, *13*, 1.

[81] S. Yang, Z. Xu, S. Xue, P. Kandlakunta, L. Cao, J. Huang, *Adv. Mater.* **2019**, *31*, 1805547.

[82] R. L. Z. Hoye, L. C. Lee, R. C. Kurchin, T. N. Huq, K. H. L. Zhang, M. Sponseller, L. Nienhaus, R. E. Brandt, J. Jean, J. A. Polizzotti, *Adv. Mater.* **2017**, *29*, 1702176.

[83] T. N. Huq, L. C. Lee, L. Eyre, W. Li, R. A. Jagt, C. Kim, S. Fearn, V. Pecunia, F. Deschler, J. L. MacManus-Driscoll, *Adv. Funct. Mater.* **2020**, *30*, 1909983.

[84] R. A. Jagt, I. Bravić, L. Eyre, K. Gałkowski, J. Borowiec, K. R. Dudipala, M. Baranowski, M. Dyksik, T. W. J. van de Goor, T. Kreouzis, *Nat. Commun.* **2023**, *14*, 2452.

**ADVANCED
SCIENCE NEWS**

www.advancedsciencenews.com

**ADVANCED
FUNCTIONAL
MATERIALS**

www.afm-journal.de

[85] A. E. Maughan, A. M. Ganose, M. M. Bordelon, E. M. Miller, D. O. Scanlon, J. R. Neilson, *J. Am. Chem. Soc.* **2016**, *138*, 8453.

[86] J. Wu, Z. Zhao, Y. Zhou, *Sci. Rep.* **2022**, *12*, 1.

[87] I. Vazquez-Fernandez, S. Mariotti, O. S. Hutter, M. Birkett, T. D. Veal, T. D. C. Hobson, L. J. Phillips, L. Danos, P. K. Nayak, H. J. Snaith, *Chem. Mater.* **2020**, *32*, 6676.

[88] R. C. Kurchin, P. Gorai, T. Buonassisi, V. Stevanovic, *Chem. Mater.* **2018**, *30*, 5583.

[89] W. Meng, B. Saparov, F. Hong, J. Wang, D. B. Mitzi, Y. Yan, *Chem. Mater.* **2016**, *28*, 821.

[90] X. Wu, W. Gao, J. Chai, C. Ming, M. Chen, H. Zeng, P. Zhang, S. Zhang, Y.-Y. Sun, *Sci. China Mater.* **2021**, *64*, 2976.

[91] J. Kim, C.-H. Chung, K.-H. Hong, *Phys. Chem. Chem. Phys.* **2016**, *18*, 27143.

[92] Z. Li, Y.-T. Huang, L. Mohan, S. J. Zelewski, R. H. Friend, R. L. Z. Hoye, *Sol. RRL* **2022**, *6*, 2200749.

[93] Z. Xiao, W. Meng, J. Wang, Y. Yan, *ChemSusChem* **2016**, *9*, 2628.

[94] R. L. Z. Hoye, L. Eyre, F. Wei, F. Brivio, A. Sadhanala, S. Sun, W. Li, K. H. L. Zhang, J. L. MacManus-Driscoll, P. D. Bristowe, *Adv. Mater. Interfaces* **2018**, *5*, 1800464.

[95] Z. Li, S. P. Senanayak, L. Dai, G. Kusch, R. Shivanna, Y. Zhang, D. Pradhan, J. Ye, Y. Huang, H. Sirringhaus, *Adv. Funct. Mater.* **2021**, *31*, 2104981.

[96] Z. Zhang, Q. Sun, Y. Lu, F. Lu, X. Mu, S.-H. Wei, M. Sui, *Nat. Commun.* **2022**, *13*, 3397.

[97] A. H. Slavney, T. Hu, A. M. Lindenberg, H. I. Karunadasa, *J. Am. Chem. Soc.* **2016**, *138*, 2138.

[98] A. D. Wright, L. R. V Buizza, K. J. Savill, G. Longo, H. J. Snaith, M. B. Johnston, L. M. Herz, *J. Phys. Chem. Lett.* **2021**, *12*, 3352.

[99] G. Longo, S. Mahesh, L. R. V Buizza, A. D. Wright, A. J. Ramadan, M. Abdi-Jalebi, P. K. Nayak, L. M. Herz, H. J. Snaith, *ACS Energy Lett.* **2020**, *5*, 2200.

[100] F. Iyoda, R. Nishikubo, A. Wakamiya, A. Saeki, *ACS Appl. Energy Mater.* **2020**, *3*, 8224.

[101] R. L. Z. Hoye, J. Hidalgo, R. A. Jagt, J. Correa-Baena, T. Fix, J. L. MacManus-Driscoll, *Adv. Energy Mater.* **2022**, *12*, 2100499.

[102] B. Saparov, F. Hong, J. P. Sun, H. S. Duan, W. Meng, S. Cameron, I. G. Hill, Y. Yan, D. B. Mitzi, *Chem. Mater.* **2015**, *27*, 5622.

[103] V. Pecunia, J. Zhao, C. Kim, B. R. Tuttle, J. Mei, F. Li, Y. Peng, T. N. Huq, R. L. Z. Hoye, N. D. Kelly, *Adv. Energy Mater.* **2021**, *11*, 2003968.

[104] P. C. Harikesh, H. K. Mulmudi, B. Ghosh, T. W. Goh, Y. T. Teng, K. Thirumal, M. Lockrey, K. Weber, T. M. Koh, S. Li, *Chem. Mater.* **2016**, *28*, 7496.

[105] B. Ghosh, S. Chakraborty, H. Wei, C. Guet, S. Li, S. Mhaisalkar, N. Mathews, *J. Phys. Chem. C* **2017**, *121*, 17062.

[106] M. Liu, H. Ali-löytty, A. Hiltunen, E. Sarlin, S. Qudsia, J. Smått, M. Valden, P. Vivo, *Small* **2021**, *17*, 2100101.

[107] R. F. Ali, I. Andreu, B. D. Gates, *Nanoscale Adv.* **2019**, *1*, 4442.

[108] M.-G. Ju, M. Chen, Y. Zhou, J. Dai, L. Ma, N. P. Padture, X. C. Zeng, *Joule* **2018**, *2*, 1231.

[109] M. Chen, M.-G. Ju, A. D. Carl, Y. Zong, R. L. Grimm, J. Gu, X. C. Zeng, Y. Zhou, N. P. Padture, *Joule* **2018**, *2*, 558.

[110] B. Parida, S. Iniyan, R. Goic, *Renew. Sust. Energ. Rev.* **2011**, *15*, 1625.

[111] N. Pai, J. Lu, T. R. Gengenbach, A. Seeber, A. S. R. Chesman, L. Jiang, D. C. Senevirathna, P. C. Andrews, U. Bach, Y. Cheng, *Adv. Energy Mater.* **2019**, *9*, 1803396.

[112] A. Merker, M. Morgenroth, M. Scholz, T. Lenzer, K. Oum, *J. Phys. Chem. C* **2023**, *127*, 1487.

[113] B. Ghosh, B. Wu, X. Guo, P. C. Harikesh, R. A. John, T. Baikie, A. T. S. Wee, C. Guet, T. C. Sum, S. Mhaisalkar, *Adv. Energy Mater.* **2018**, *8*, 1802051.

[114] M. Khazaee, K. Sardashti, C.-C. Chung, J.-P. Sun, H. Zhou, E. Bergmann, W. A. Dunlap-Shohl, Q. Han, I. G. Hill, J. L. Jones, *J. Mater. Chem. A* **2019**, *7*, 2095.

[115] L. R. V Buizza, H. C. Sansom, A. D. Wright, A. M. Ulatowski, M. B. Johnston, H. J. Snaith, L. M. Herz, *Adv. Funct. Mater.* **2022**, *32*, 2108392.

[116] A. M. Ganose, K. T. Butler, A. Walsh, D. O. Scanlon, *J. Mater. Chem. A* **2016**, *4*, 2060.

[117] D. Tiwari, F. Cardoso-Delgado, D. Alibhai, M. Mombru, D. J. Fermín, *ACS Appl. Energy Mater.* **2019**, *2*, 3878.

[118] A. M. Ganose, S. Matsumoto, J. Buckeridge, D. O. Scanlon, *Chem. Mater.* **2018**, *30*, 3827.

[119] B. Yang, W. Pan, H. Wu, G. Niu, J.-H. Yuan, K.-H. Xue, L. Yin, X. Du, X.-S. Miao, X. Yang, *Nat. Commun.* **2019**, *10*, 1989.

[120] R. L. Z. Hoye, R. E. Brandt, A. Osherov, V. Stevanović, S. D. Stranks, M. W. B. Wilson, H. Kim, A. J. Akey, J. D. Perkins, R. C. Kurchin, *Chem. - Eur. J.* **2016**, *22*, 2605.

[121] B. Yang, J. Chen, F. Hong, X. Mao, K. Zheng, S. Yang, Y. Li, T. Pullerits, W. Deng, K. Han, *Angew. Chem., Int. Ed.* **2017**, *56*, 12471.

[122] M. Leng, Y. Yang, Z. Chen, W. Gao, J. Zhang, G. Niu, D. Li, H. Song, J. Zhang, S. Jin, *Nano Lett.* **2018**, *18*, 6076.

[123] G. Paul, A. J. Pal, B. W. Larson, *Sol. RRL* **2021**, *5*, 2000422.

[124] W. A. Dunlap-Shohl, Y. Zhou, N. P. Padture, D. B. Mitzi, *Chem. Rev.* **2018**, *119*, 3193.

[125] S. De Wolf, J. Holovsky, S.-J. Moon, P. Loper, B. Niesen, M. Ledinsky, F.-J. Haug, J.-H. Yum, C. Ballif, *J. Phys. Chem. Lett.* **2014**, *5*, 1035.

[126] Z. Li, S. R. Kavanagh, M. Napari, R. G. Palgrave, M. Abdi-Jalebi, Z. Andaji-Garmaroudi, D. W. Davies, M. Laitinen, J. Julin, M. A. Isaacs, *J. Mater. Chem. A* **2020**, *8*, 21780.

[127] W. Pan, H. Wu, J. Luo, Z. Deng, C. Ge, C. Chen, X. Jiang, W.-J. Yin, G. Niu, L. Zhu, *Nat. Photonics* **2017**, *11*, 726.

[128] R. Kentsch, M. Scholz, J. Horn, D. Schlettwein, K. Oum, T. Lenzer, *J. Phys. Chem. C* **2018**, *122*, 25940.

[129] F. Umar, J. Zhang, Z. Jin, I. Muhammad, X. Yang, H. Deng, K. Jahangeer, Q. Hu, H. Song, J. Tang, *Adv. Opt. Mater.* **2019**, *7*, 1801368.

[130] J.-P. Correa-Baena, L. Nienhaus, R. C. Kurchin, S. S. Shin, S. Wieghold, N. T. Putri Hartono, M. Layurova, N. D. Klein, J. R. Poindexter, A. Polizzotti, *Chem. Mater.* **2018**, *30*, 3734.

[131] Y. Peng, F. Li, Y. Wang, Y. Li, R. L. Z. Hoye, L. Feng, K. Xia, V. Pecunia, *Appl. Mater. Today* **2020**, *19*, 100637.

[132] K. M. McCall, C. C. Stoumpos, S. S. Kostina, M. G. Kanatzidis, B. W. Wessels, *Chem. Mater.* **2017**, *29*, 4129.

[133] A. Hiltunen, N. Lamminen, H. Salonen, M. Liu, P. Vivo, *Sustain. Energy Fuels* **2022**, *6*, 217.

[134] A. Singh, K. M. Boopathi, A. Mohapatra, Y. F. Chen, G. Li, C. W. Chu, *ACS Appl. Mater. Interfaces* **2018**, *10*, 2566.

[135] Y. Zhang, Y. Liu, Z. Xu, H. Ye, Z. Yang, J. You, M. Liu, Y. He, M. G. Kanatzidis, S. Liu, *Nat. Commun.* **2020**, *11*, 2304.

[136] X. Zheng, W. Zhao, P. Wang, H. Tan, M. I. Saidaminov, S. Tie, L. Chen, Y. Peng, J. Long, W.-H. Zhang, *J. Energy Chem.* **2020**, *49*, 299.

[137] J. Euvrard, X. Wang, T. Li, Y. Yan, D. B. Mitzi, *J. Mater. Chem. A* **2020**, *8*, 4049.

[138] G. K. Grandhi, A. Matuhina, M. Liu, S. Annurakshita, H. Ali-Löytty, G. Bautista, P. Vivo, *Nanomaterials* **2021**, *11*, 1458.

[139] M. Krishnaiah, S. Kim, A. Kumar, D. Mishra, S. G. Seo, S. H. Jin, *Adv. Mate.* **2022**, *34*, 2109673.

[140] A. Chakraborty, N. Pai, J. Zhao, B. R. Tuttle, A. N. Simonov, V. Pecunia, *Adv. Funct. Mater.* **2022**, *32*, 2203300.

[141] C. Lu, J. Zhang, H. Sun, D. Hou, X. Gan, M. Shang, Y. Li, Z. Hu, Y. Zhu, L. Han, *ACS Appl. Energy Mater.* **2018**, *1*, 4485.

[142] R. Nie, H. Yun, M. Paik, A. Mehta, B. Park, Y. C. Choi, S. Il Seok, *Adv. Energy Mater.* **2018**, *8*, 1701901.

[143] P. Szperlich, M. Nowak, Ł. Bober, J. Szala, D. Stróż, *Ultrason. Sonochem.* **2009**, *16*, 398.

[144] A. J. Lehner, D. H. Fabini, H. A. Evans, C.-A. H. Hébert, S. R. Smock, J. Hu, H. Wang, J. W. Zwanziger, M. L. Chabinyc, R. Seshadri, *Chem. Mater.* **2015**, *27*, 7137.

[145] Z. Zhang, X. Li, X. Xia, Z. Wang, Z. Huang, B. Lei, Y. Gao, *J. Phys. Chem. Lett.* **2017**, *8*, 4300.

[146] C. Lan, G. Liang, S. Zhao, H. Lan, H. Peng, D. Zhang, H. Sun, J. Luo, P. Fan, *Sol. Energy* **2019**, *177*, 501.

[147] K. Ahmad, P. Kumar, H. Kim, S. M. Mobin, *ChemNanoMat.* **2022**, *8*, 202200061.

[148] M. B. Johansson, H. Zhu, E. M. J. Johansson, *J. Phys. Chem. Lett.* **2016**, *7*, 3467.

[149] P. Mariyappan, T. H. Chowdhury, S. Subashchandran, I. Bedja, H. M. Ghaithan, A. Islam, *Sustain. Energy Fuels* **2020**, *4*, 5042.

[150] P. Sebastia-Luna, M. C. Gélvez-Rueda, C. Dreessen, M. Sessolo, F. C. Grozema, F. Palazon, H. J. Bolink, *J. Mater. Chem. A* **2020**, *8*, 15670.

[151] M. Ghasemi, L. Zhang, J. H. Yun, M. Hao, D. He, P. Chen, Y. Bai, T. Lin, M. Xiao, A. Du, M. Lyu, L. Wang, *Adv. Funct. Mater.* **2020**, *30*, 2002342.

[152] C. Lu, J. Zhang, H. Sun, D. Hou, X. Gan, M. H. Shang, Y. Li, Z. Hu, Y. Zhu, L. Han, *ACS Appl. Energy Mater.* **2018**, *1*, 4485.

[153] M. Khazaee, K. Sardashti, C. C. Chung, J. P. Sun, H. Zhou, E. Bergmann, W. A. Dunlap-Shohl, Q. Han, I. G. Hill, J. L. Jones, D. C. Lupascu, D. B. Mitzi, *J. Mater. Chem. A* **2019**, *7*, 2095.

[154] C. Zhang, L. Gao, S. Teo, Z. Guo, Z. Xu, S. Zhao, T. Ma, *Sustain. Energy Fuels* **2018**, *2*, 2419.

[155] Y. Peng, T. N. Huq, J. Mei, L. Portilla, R. A. Jagt, L. G. Occhipinti, J. L. MacManus-Driscoll, R. L. Z. Hoye, V. Pecunia, *Adv. Energy Mater.* **2021**, *11*, 2002761.

[156] R. E. Brandt, J. R. Poindexter, P. Gorai, R. C. Kurchin, R. L. Z. Hoye, L. Nienhaus, M. W. B. Wilson, J. A. Polizzotti, R. Sereika, R. Žaltauskas, L. C. Lee, J. L. Macmanus-Driscoll, M. Bawendi, V. Stevanović, T. Buonassisi, *Chem. Mater.* **2017**, *29*, 4667.

[157] V. Arivazhagan, F. Gun, R. K. K. Reddy, T. Li, M. Adelt, N. Robertson, Y. Chen, A. Ivaturi, *Sustain. Energy Fuels* **2022**, *6*, 3179.

[158] N. Pai, M. Chatti, S. O. Fürer, A. D. Scully, S. R. Raga, N. Rai, B. Tan, A. S. R. Chesman, Z. Xu, K. J. Rietwyk, S. S. Reddy, Y. Hora, G. A. Sepalage, N. Glück, M. Lira-Cantú, U. Bach, A. N. Simonov, *Adv. Energy Mater.* **2022**, *12*, 202201482.

[159] G. K. Grandhi, R. Dhama, N. S. M. Viswanath, E. S. Lisitsyna, B. Al-Anesi, J. Dana, V. Sugathan, H. Caglayan, P. Vivo, *J. Phys. Chem. Lett.* **2023**, *14*, 4192.

[160] G. K. Grandhi, B. Al-Anesi, H. Pasanen, H. Ali-Löytty, K. Lahtonen, S. Granroth, N. Christian, A. Matuhina, M. Liu, A. Berdin, V. Pecunia, P. Vivo, G. K. Grandhi, B. Al-Anesi, H. Pasanen, N. Christian, A. Matuhina, M. Liu, P. Vivo, H. Ali-Löytty, K. Lahtonen, S. Granroth, A. Berdin, *Small* **2022**, *18*, 2203768.

[161] B. Al-Anesi, G. K. Grandhi, A. Pecoraro, V. Sugathan, N. S. M. Viswanath, H. Ali-Löytty, M. Liu, T.-P. Ruoko, K. Lahtonen, D. Manna, S. Toikkonen, A. B. Muñoz-García, M. Pavone, P. Vivo, **2023**, https://doi.org/10.26434/CHEMRXIV-2023-NB5JJ.

[162] Y. Yang, C. Liu, Y. Cai, Y. Liao, Y. Ding, S. Ma, X. Liu, M. Guli, S. Dai, M. K. Nazeeruddin, *ACS Appl. Mater. Interfaces* **2020**, *12*, 17062.

[163] N. Lamminen, G. K. Grandhi, F. Fasulo, A. Hiltunen, H. Pasanen, M. Liu, B. Al-Anesi, A. Efimov, H. Ali-Löytty, K. Lahtonen, P. Mäkinen, A. Matuhina, A. B. Muñoz-García, M. Pavone, P. Vivo, *Adv. Energy Mater.* **2023**, *13*, 2203175.

[164] Z. Li, S. R. Kavanagh, M. Napari, R. G. Palgrave, M. Abdi-Jalebi, Z. Andaji-Garmaroudi, D. W. Davies, M. Laitinen, J. Julin, M. A. Isaacs, R. H. Friend, D. O. Scanlon, A. Walsh, R. L. Z. Hoye, *J. Mater. Chem. A* **2020**, *8*, 21780.

[165] K. M. Boopathi, P. Karuppuswamy, A. Singh, C. Hanmandlu, L. Lin, S. A. Abbas, C. C. Chang, P. C. Wang, G. Li, C. W. Chu, *J. Mater. Chem. A* **2017**, *5*, 20843.

[166] R. Nie, A. Mehta, B. W. Park, H. W. Kwon, J. Im, S. Il Seok, *J. Am. Chem. Soc.* **2018**, *140*, 872.

[167] A. Hiltunen, N. Lamminen, H. Salonen, M. Liu, P. Vivo, *Sustain. Energy Fuels* **2021**, *6*, 217.

[168] P. C. Harikesh, H. K. Mulmudi, B. Ghosh, T. W. Goh, Y. T. Teng, K. Thirumal, M. Lockrey, K. Weber, T. M. Koh, S. Li, S. Mhaisalkar, N. Mathews, *Chem. Mater.* **2016**, *28*, 7496.

[169] Q. Mahmood, M. Hassan, N. Yousaf, A. A. AlObaid, T. I. Al-Muhimeed, M. Morsi, H. Albalawi, O. A. Alamri, *Mater. Sci. Semicond. Process* **2022**, *137*, 106180.

[170] M. Chen, M.-G. Ju, A. D. Carl, X. C. Zeng, Y. Zhou, N. P. Padture, *Joule* **2018**, *2*, 558.

[171] D. Tiwari, F. Cardoso-Delgado, D. Alibhai, M. Mombrú, D. J. Fermín, *ACS Appl. Energy Mater.* **2019**, *2*, 3878.

[172] R. Nie, H. Yun, M.-J. Paik, A. Mehta, B. Park, Y. Chan Choi, S. Il Seok, R. M. Nie, H. Yun, M. Paik, A. Mehta, B. Park, S. I. Seok, Y. C. Choi, *Adv. Energy Mater.* **2018**, *8*, 1701901.

[173] S. Ullah, J. Wang, P. Yang, L. Liu, J. khan, S. E. Yang, T. Xia, H. Guo, Y. Chen, *Sol. RRL* **2021**, *5*, 1.

[174] W. Cao, Z. Hu, Z. Lin, X. Guo, J. Su, J. Chang, Y. Hao, *J. Energy Chem.* **2022**, *68*, 420.

[175] X. Chen, M. Jia, W. Xu, G. Pan, J. Zhu, Y. Tian, D. Wu, X. Li, Z. Shi, *Adv. Opt. Mater.* **2023**, *11*, 202202153.

[176] V. M. Caselli, J. Thieme, H. J. Jöbsis, S. A. Phadke, J. Zhao, E. M. Hutter, T. J. Savenije, *Cell Rep. Phys. Sci.* **2022**, *3*, 101055.

[177] Y. Zhou, I. Poli, D. Meggiolaro, F. De Angelis, A. Petrozza, *Nat. Rev. Mater.* **2021**, *6*, 986.

[178] J. Shen, W. Zhu, Z. Lian, A. Lin, S. F. Shi, K. Yang, M. Li, D. Zhao, Y. Y. Sun, J. Lian, *ACS Appl. Electron. Mater.* **2022**, https://doi.org/10.1021/acsaelm.2c01265.

[179] F. Umar, J. Zhang, Z. Jin, I. Muhammad, X. Yang, H. Deng, K. Jahangeer, Q. Hu, H. Song, J. Tang, *Adv. Opt. Mater.* **2019**, *7*, 1.

[180] K. Park, J. H. Lee, J. W. Lee, *ACS Energy Lett.* **2022**, *7*, 1230.

[181] L. R. V. Buizza, A. D. Wright, G. Longo, H. C. Sansom, C. Q. Xia, M. J. Rosseinsky, M. B. Johnston, H. J. Snaith, L. M. Herz, *ACS Energy Lett.* **2021**, *6*, 1729.

[182] V. H. Vuong, S. V. N. Pammi, K. S. Pasupuleti, W. Hu, V. D. Tran, J. S. Jung, M. D. Kim, V. Pecunia, S. G. Yoon, *Adv. Opt. Mater.* **2021**, *9*, 202100192.

[183] M. Krishnaiah, S. Kim, A. Kumar, D. Mishra, S. G. Seo, S. H. Jin, *Adv. Mater.* **2022**, *34*, 1.

[184] F. Guo, Z. Lu, D. Mohanty, T. Wang, I. B. Bhat, S. Zhang, S. Shi, M. A. Washington, G. C. Wang, T. M. Lu, *Mater. Res. Lett.* **2017**, *5*, 540.

[185] R. Gegevičius, M. Franckevičius, V. Gulbinas, *Eur. J. Inorg. Chem.* **2021**, *2021*, 3519.

[186] C. Wehrenfennig, G. E. Eperon, M. B. Johnston, H. J. Snaith, L. M. Herz, *Adv. Mater.* **2014**, *26*, 1584.

[187] Y. Tang, C. H. Mak, G. Jia, K. C. Cheng, J. J. Kai, C. W. Hsieh, F. Meng, W. Niu, F. F. Li, H. M. Shen, X. Zhu, H. M. Chen, H. Y. Hsu, *J. Mater. Chem. A* **2022**, *10*, 12296.

[188] G. Yan, B. Jiang, Y. Xiao, C. Zhao, Y. Yuan, Z. Liang, *Appl. Surf. Sci.* **2022**, *579*, 152198.

[189] N. Ding, L. Shao, T. Xie, G. Pan, D. Zhou, X. Bai, S. Lu, S. Hu, J. Zhou, W. Xu, H. Song, *Laser Photon. Rev.* **2022**, *16*, 1.

[190] K. Kim, J. Han, S. Maruyama, M. Balaban, I. Jeon, *Sol. RRL* **2021**, *5*, 1.

[191] Z. Shuang, H. Zhou, D. Wu, X. Zhang, B. Xiao, G. Ma, J. Zhang, H. Wang, *Chem. Eng. J.* **2022**, *433*, 134544.

[192] Z. Gao, H. Zhou, K. Dong, C. Wang, J. Wei, Z. Li, J. Li, Y. Liu, J. Zhao, G. Fang, *Nanomicro Lett.* **2022**, *14*, 1.

[193] J. Li, X. Meng, Z. Wu, Y. Duan, R. Guo, W. Xiao, Y. Zhang, Y. Li, Y. Shen, W. Zhang, G. Shao, *Adv. Funct. Mater.* **2022**, *32*, 202112991.

[194] J. Yang, Y. Wang, L. Huang, G. Li, X. Qiu, X. Zhang, W. Sun, *J. Phys. Chem. Lett.* **2022**, *13*, 3904.

**ADVANCED
SCIENCE NEWS**

www.advancedsciencenews.com

**ADVANCED
FUNCTIONAL
MATERIALS**

www.afm-journal.de

[254] M. A. K. Khan, S. S. Urmi, T. T. Ferdous, S. Azam, M. A. Alim, *Super-lattices Microstruct.* **2021**, *156*, 106946.

[255] D. Liu, R. Sa, *Opt. Mater.* **2020**, *110*, 110497.

[256] P. Shrivastava, B. Kavaipatti, P. Bhargava, *Int. J. Energy Res.* **2021**, *45*, 8049.

[257] N. Sakai, A. A. Haghighirad, M. R. Filip, P. K. Nayak, S. Nayak, A. Ramadan, Z. Wang, F. Giustino, H. J. Snaith, *J. Am. Chem. Soc.* **2017**, *139*, 6030.

[258] P. Xu, F. Liu, *AIP Adv.* **2020**, *10*, 115203.

[259] A. E. Maughan, A. M. Ganose, M. A. Almaker, D. O. Scanlon, J. R. Neilson, *Chem. Mater.* **2018**, *30*, 3909.

[260] P. Day, *Inorg. Chem.* **1963**, *2*, 452.

[261] K. Prassides, P. Day, A. K. Cheetham, *Inorg. Chem.* **1985**, *24*, 545.

[262] B. Zhang, Y. Lei, R. Qi, H. Yu, X. Yang, T. Cai, Z. Zheng, *Sci. China Mater.* **2019**, *62*, 519.

[263] Y. Kim, Z. Yang, A. Jain, O. Voznyy, G. Kim, M. Liu, L. N. Quan, F. P. García de Arquer, R. Comin, J. Z. Fan, *Angew. Chem., Int. Ed.* **2016**, *55*, 9586.

[264] V. Pecunia, Y. Yuan, J. Zhao, K. Xia, Y. Wang, S. Duhm, L. Portilla, F. Li, *Nanomicro Lett.* **2020**, *12*, 1.

[265] K. W. Jung, M. R. Sohn, H. M. Lee, I. S. Yang, S. Do Sung, J. Kim, E. W.-G. Diau, W. I. Lee, *Sustain. Energy Fuels* **2018**, *2*, 294.

[266] Q. Zhang, C. Wu, X. Qi, F. Lv, Z. Zhang, Y. Liu, S. Wang, B. Qu, Z. Chen, L. Xiao, *ACS Appl. Energy Mater.* **2019**, *2*, 3651.

[267] Y. Yuan, N. Robertson, *Sustain. Energy Fuels* **2023**, *7*, 1067.

[268] K.-C. Hsiao, Y.-F. Yu, C.-M. Ho, M.-H. Jao, Y.-H. Chang, S.-H. Chen, Y.-H. Chang, W.-F. Su, K.-M. Lee, M.-C. Wu, *Chem. Eng. J.* **2023**, *451*, 138807.

[269] T. Zhang, F. Wang, H.-B. Kim, I.-W. Choi, C. Wang, E. Cho, R. Konefal, Y. Puttisong, K. Terado, L. Kobera, *Science* **2022**, *377*, 495.

[270] F. Yu, L. Wang, K. Ren, S. Yang, Z. Xu, Q. Han, T. Ma, *ACS Sustainable Chem. Eng.* **2020**, *8*, 9980.

[271] H. Zhu, A. Erbing, H. Wu, G. J. Man, S. Mukherjee, C. Kamal, M. B. Johansson, H. Rensmo, M. Odelius, E. M. J. Johansson, *ACS Appl. Energy Mater.* **2020**, *3*, 7372.

[272] S. Hosseini, M. Adelifard, *Phys. Status Solidi A* **2021**, *218*, 2000774.

[273] H. Wu, H. Zhu, A. Erbing, M. B. Johansson, S. Mukherjee, G. J. Man, H. Rensmo, M. Odelius, E. M. J. Johansson, *ACS Appl. Energy Mater.* **2019**, *2*, 5356.

[274] Y.-Y. Sun, J. Shi, J. Lian, W. Gao, M. L. Agiorgousis, P. Zhang, S. Zhang, *Nanoscale* **2016**, *8*, 6284.

[275] C. Zhang, S. Teo, L. Gao, Y. Kamata, M. A. Tingli, in *Physical Chemistry of Semiconductor Materials and Interfaces XVII*, SPIE, xx xx **2018**, pp. 19–27.

[276] F. Hong, B. Saparov, W. Meng, Z. Xiao, D. B. Mitzi, Y. Yan, *J. Phys. Chem. C* **2016**, *120*, 6435.

[277] R. Nie, A. Mehta, B. Park, H.-W. Kwon, J. Im, S. Il Seok, *J. Am. Chem. Soc.* **2018**, *140*, 872.

[278] J. Li, X. Liu, J. Xu, J. Chen, C. Zhao, M. Salma Maneno, B. Zhang, J. Yao, *Sol. RRL* **2019**, *3*, 1900218.

[279] C. Zhang, S. Teo, Z. Guo, L. Gao, Y. Kamata, Z. Xu, T. Ma, *Chem. Lett.* **2019**, *48*, 249.

[280] R. Nie, S. Il Seok, *Small Methods* **2020**, *4*, 1900698.

[281] Z. S. Aliev, S. S. Musayeva, F. Y. Jafarli, I. R. Amiraslanov, A. V Shevelkov, M. B. Babanly, *J. Alloys Compd.* **2014**, *610*, 522.

[282] R. Nie, K. S. Lee, M. Hu, M. J. Paik, S. Il Seok, *Matter* **2020**, *3*, 1701.

[283] P.-C. Huang, W.-C. Yang, M.-W. Lee, *J. Phys. Chem. C* **2013**, *117*, 18308.

[284] J. Liu, J. Wang, W. Zhao, Z. Zhou, L. Ye, *Sci. Bull.* **2023**, *68*, 251.

[285] Y.-Y. Sun, M. L. Agiorgousis, P. Zhang, S. Zhang, *Nano Lett.* **2015**, *15*, 581.

[286] S. Perera, H. Hui, C. Zhao, H. Xue, F. Sun, C. Deng, N. Gross, C. Milleville, X. Xu, D. F. Watson, *Nano Energy* **2016**, *22*, 129.

[287] A. Swarnkar, W. J. Mir, R. Chakraborty, M. Jagadeeswararao, T. Sheikh, A. Nag, *Chem. Mater.* **2019**, *31*, 565.

[288] K. V. Sopiha, C. Comparotto, J. A. Márquez, J. J. S. Scragg, *Adv. Opt. Mater.* **2022**, *10*, 2101704.

[289] T. Gupta, D. Ghoshal, A. Yoshimura, S. Basu, P. K. Chow, A. S. Lakhnot, J. Pandey, J. M. Warrender, H. Efstathiadis, A. Soni, *Adv. Funct. Mater.* **2020**, *30*, 2001387.

[290] S. Sharma, Z. Ward, K. Bhimani, K. Li, A. Lakhnot, R. Jain, S.-F. Shi, H. Terrones, N. Koratkar, *ACS Appl. Electr. Mater.* **2021**, *3*, 3306.

[291] E. Osei-Agyemang, N. Koratkar, G. Balasubramanian, *J. Mater. Chem. C* **2021**, *9*, 3892.

[292] A. Crovetto, R. Nielsen, M. Pandey, L. Watts, J. G. Labram, M. Geisler, N. Stenger, K. W. Jacobsen, O. Hansen, B. Seger, *Chem. Mater.* **2019**, *31*, 3359.

[293] A. Clearfield, *Acta Crystallogr.* **1963**, *16*, 135.

[294] Z. Yu, X. Wei, Y. Zheng, H. Hui, M. Bian, S. Dhole, J.-H. Seo, Y.-Y. Sun, Q. Jia, S. Zhang, *Nano Energy* **2021**, *85*, 105959.

[295] J. W. Turnley, K. C. Vincent, A. A. Pradhan, I. Panicker, R. Swope, M. C. Uible, S. C. Bart, R. Agrawal, *J. Am. Chem. Soc.* **2022**, *144*, 18234.

[296] D. Zilevu, O. O. Parks, S. E. Creutz, *Chem. Commun.* **2022**, *58*, 10512.

[297] D. Zilevu, S. E. Creutz, *Chem. Mater.* **2021**, *33*, 5137.

[298] A. A. Pradhan, M. C. Uible, S. Agarwal, J. W. Turnley, S. Khandelwal, J. M. Peterson, D. D. Blach, R. N. Swope, L. Huang, S. C. Bart, *Angew. Chem., Int. Ed.* **2023**, *62*, 202301049.

[299] R. Yang, A. D. Jess, C. Fai, C. J. Hages, *J. Am. Chem. Soc.* **2022**, *144*, 15928.

[300] I. Mathews, S. N. Kantareddy, T. Buonassisi, I. M. Peters, *Joule* **2019**, *3*, 1415.

[301] M. Freunek, M. Freunek, L. M. Reindl, *IEEE J Photovolt* **2012**, *3*, 59.

[302] Y. Peng, T. N. Huq, J. Mei, L. Portilla, R. A. Jagt, L. G. Occhipinti, J. L. Macmanus-driscoll, R. L. Z. Hoye, V. Pecunia, *Adv. Energy Mater.* **2020**, *11*, 2002761.

[303] Z. Guo, A. K. Jena, T. Miyasaka, *ACS Energy Lett.* **2022**, *8*, 90.

[304] C. Dong, X. Li, C. Ma, W. Yang, J. Cao, F. Igbari, Z. Wang, L. Liao, *Adv. Funct. Mater.* **2021**, *31*, 2011242.

[305] X. He, J. Chen, X. Ren, L. Zhang, Y. Liu, J. Feng, J. Fang, K. Zhao, S. Liu, *Adv. Mater.* **2021**, *33*, 2100770.

[306] J. K. W. Ho, H. Yin, S. K. So, *J. Mater. Chem. A* **2020**, *8*, 1717.

[307] R. H. Blube, *Photoconductivity of Solids*, Wiley, New York **1960**.

[308] I. Turkevych, S. Kazaoui, N. Shirakawa, N. Fukuda, *Jpn. J. Appl. Phys.* **2021**, *60*, 2.

[309] N. B. Correa Guerrero, Z. Guo, N. Shibayama, A. K. Jena, T. Miyasaka, *ACS Appl. Energy Mater.* **2023**, https://doi.org/10.1021/acsaem.3c00223.

[310] N. Lamminen, G. K. Grandhi, F. Fasulo, A. Hiltunen, H. Pasanen, M. Liu, B. Al-Anesi, A. Efimov, H. Ali-Löytty, K. Lahtonen, *Adv. Energy Mater.* **2023**, *13*, 2203175.

[311] H. Yin, J. K. W. Ho, S. H. Cheung, R. J. Yan, K. L. Chiu, X. Hao, S. K. So, *J. Mater. Chem. A* **2018**, *6*, 8579.

[312] S. Makuta, M. Liu, M. Endo, H. Nishimura, A. Wakamiya, Y. Tachibana, *Chem. Commun.* **2016**, *52*, 673.

[313] A. Singh, P.-T. Lai, A. Mohapatra, C.-Y. Chen, H.-W. Lin, Y.-J. Lu, C. W. Chu, *Chem. Eng. J.* **2021**, *419*, 129424.

[314] Z. Ding, R. Zhao, Y. Yu, J. Liu, *J. Mater. Chem. A* **2019**, *7*, 26533.

[315] I. Turkevych, S. Kazaoui, N. Shirakawa, N. Fukuda, *Jpn. J. Appl. Phys.* **2021**, *60*, SCCE06.

[316] Y. Pihosh, J. Uemura, I. Turkevych, K. Mawatari, Y. Kazoe, A. Smirnova, T. Kitamori, *Angew. Chem., Int. Ed.* **2017**, *129*, 8242.

[317] B. Al-Anesi, G. K. Grandhi, A. Pecoraro, V. Sugathan, N. S. M. Viswanath, H. Ali-Löytty, M. Liu, T.-P. Ruoko, K. Lahtonen, D. Manna, S. Toikkonen, A. B. Muñoz-García, M. Pavone, P. Vivo, *Small* **2023**, https://doi.org/10.1002/smll.202303575.

**ADVANCED
SCIENCE NEWS**

www.advancedsciencenews.com

**ADVANCED
FUNCTIONAL
MATERIALS**

www.afm-journal.de

[318] K.-L. Wang, Y.-H. Zhou, Y.-H. Lou, Z.-K. Wang, *Chem. Sci.* **2021**, *12*, 11936.

[319] Z. Bi, S. Zhang, M. Thandapani, Y. Zhu, Y. Zheng, N. Q. Liem, X. Xiao, G. Xu, A. Guerrero, X. Xu, *Adv Sustain Syst* **2021**, *5*, 2100120.

[320] B. Cucco, L. Pedesseau, C. Katan, J. Even, M. Kepenekian, G. Volonakis, *Sol. RRL* **2022**, 2200718.

[321] L. Yu, A. Zunger, *Phys. Rev. Lett.* **2012**, *108*, 068701.

[322] C. N. Savory, A. Walsh, D. O. Scanlon, *ACS Energy Lett.* **2016**, *1*, 949.

[323] A. Zakutayev, J. D. Major, X. Hao, A. Walsh, J. Tang, T. K. Todorov, L. H. Wong, E. Saucedo, *J. Phys. Energy* **2021**, *3*, 032003.

[324] S. Zeiske, O. J. Sandberg, N. Zarrabi, C. M. Wolff, M. Raoufi, F. Peña-Camargo, E. Gutierrez-Partida, P. Meredith, M. Stolterfoht, A. Armin, *J. Phys. Chem. Lett.* **2022**, *13*, 7280.

[325] B. Subedi, C. Li, C. Chen, D. Liu, M. M. Junda, Z. Song, Y. Yan, N. J. Podraza, *ACS Appl. Mater. Interfaces* **2022**, *14*, 7796.

[326] S. Zeiske, C. Kaiser, P. Meredith, A. Armin, *ACS Photonics* **2019**, *7*, 256.

[327] M. Baranowski, J. M. Urban, N. Zhang, A. Surrente, D. K. Maude, Z. Andaji-Garmaroudi, S. D. Stranks, P. Plochocka, *J. Phys. Chem. C* **2018**, *122*, 17473.

[328] H. Mehdizadeh-Rad, J. Singh, *ChemPhysChem* **2019**, *20*, 2712.

[329] J.-C. Hebig, I. Kuhn, J. Flohre, T. Kirchartz, *ACS Energy Lett.* **2016**, *1*, 309.

[330] N. K. Tailor, S. Satapathi, *ACS Appl. Energy Mater.* **2020**, *3*, 11732.

[331] A. Maiti, A. J. Pal, *J. Phys. Chem. C* **2021**, *125*, 16324.

[332] Y. Nishigaki, T. Nagai, M. Nishiwaki, T. Aizawa, M. Kozawa, K. Hanzawa, Y. Kato, H. Sai, H. Hiramatsu, H. Hosono, *Sol. RRL* **2020**, *4*, 1900555.

[333] M. He, Z. Xu, C. Zhao, Y. Gao, K. Ke, N. Liu, X. Yao, F. Kang, Y. Shen, L. Lin, G. Wei, *Adv. Funct. Mater.* **2023**, *33*, 2300282.

[334] Y. Cheng, C. Li, J. Li, T. Li, Y. Sun, J. Zhang, F. Wang, Y. Li, Y. Shi, L. Pan, *IEEE Electron Device Lett.* **2022**, *43*, 2137.

[335] Y. Luo, M. R. Abidian, J.-H. Ahn, D. Akinwande, A. M. Andrews, M. Antonietti, Z. Bao, M. Berggren, C. A. Berkey, C. J. Bettinger, J. Chen, P. Chen, W. Cheng, X. Cheng, S.-J. Choi, A. Chortos, C. Dagdeviren, R. H. Dauskardt, C. Di, M. D. Dickey, X. Duan, A. Facchetti, Z. Fan, Y. Fang, J. Feng, X. Feng, H. Gao, W. Gao, X. Gong, C. F. Guo, et al., *ACS Nano* **2023**, *17*, 5211.

[336] M. Peng, Z. Wen, X. Sun, *Adv. Funct. Mater.* **2023**, *33*, 2211548.

[337] F. Cao, T. Yan, Z. Li, L. Wu, X. Fang, *Adv. Opt. Mater.* **2022**, *10*, 202200786.

[338] L. He, G. Hu, J. Jiang, W. Wei, X. Xue, K. Fan, H. Huang, L. Shen, *Adv. Mater.* **2023**, *35*, 1.

[339] A. Mathur, H. Fan, V. Maheshwari, *Mater. Adv.* **2021**, *2*, 5274.

[340] S. Yin, Y. Cheng, Y. Li, W. Liang, T. Li, J. Ma, D. Wu, Z. Shi, X. Li, *J. Mater. Sci.* **2021**, *56*, 13633.

[341] A. A. Hussain, *ACS Appl. Mater. Interfaces* **2020**, *12*, 46317.

[342] S. Devasia, S. Shaji, D. A. Avellaneda, J. A. Aguilar Martinez, B. Krishnan, *Mater. Chem. Phys.* **2023**, *296*, 127295.

[343] D. Hao, D. Liu, S. Zhang, L. Li, B. Yang, J. Huang, *Adv. Opt. Mater.* **2022**, *10*, 202100786.

[344] L. Peng, L. Hu, X. Fang, *Adv. Funct. Mater.* **2014**, *24*, 2591.

[345] S. Sahare, P. Ghoderao, M. K. Sharma, M. Solovan, R. Aepuru, M. Kumar, Y. Chan, M. Ziółek, S. L. Lee, Z. H. Lin, *Nano Energy* **2023**, *107*, 08172.

[346] S. Ippili, V. Jella, A. M. Thomas, S.-G. Yoon, *Nanoenergy Advances* **2021**, *1*, 3.

[347] S. F. Leung, K. T. Ho, P. K. Kung, V. K. S. Hsiao, H. N. Alshareef, Z. L. Wang, J. H. He, *Adv. Mater.* **2018**, *30*, 1.

[348] R. Zhao, Z. Gu, P. Li, Y. Zhang, Y. Song, *Adv. Mater. Technol.* **2022**, *7*, 1.

[349] M. Krishnaiah, A. Kumar, D. Mishra, H. Bin Jo, G. Lee, S. Hun Jin, *Appl. Surf. Sci.* **2023**, *626*, 157251.

[350] J. Huang, C. Dong, Y. Mei, X. Lu, G. Yue, Y. Gao, R. Liu, W. Zhang, F. Tan, *J. Mater. Chem. C* **2021**, *9*, 14217.

[351] M. Sulaman, S. Y. Yang, Z. H. Zhang, A. Imran, A. Bukhtiar, Z. H. Ge, Y. Tang, Y. R. Jiang, L. B. Tang, B. S. Zou, *Mater. Today Phys.* **2022**, *27*, 100829.

[352] B. Jiang, G. Yan, Y. Xiao, Y. Yuan, C. Zhao, W. Mai, R. Hong, *J. Mater. Sci.* **2023**, *58*, 7076.

[353] X. Li, Y. Zhou, F. Huang, X. Tao, Y. Ouyang, X. Mo, J. Zhao, *J. Mater. Chem. C* **2023**, *11*, 5073.

[354] X. Zhou, C. Wang, J. Luo, L. Zhang, F. Zhao, Q. Ke, *Chem. Eng. J.* **2022**, *450*, 136364.

[355] J. Mei, M. Liu, P. Vivo, V. Pecunia, *Adv. Funct. Mater.* **2021**, *31*, 202106295.

[356] T. Ji, H. Zhang, J. Guo, Y. Wang, L. Shi, Y. Wu, W. Wang, G. Li, R. Wen, L. Xiao, Q. Su, B. Xu, H. Chen, Y. Cui, *Adv. Funct. Mater.* **2023**, *33*, 202210548.

[357] F. Liu, K. Liu, S. Rafique, Z. Xu, W. Niu, X. Li, Y. Wang, L. Deng, J. Wang, X. Yue, T. Li, J. Wang, P. Ayala, C. Cong, Y. Qin, A. Yu, N. Chi, Y. Zhan, *Adv. Sci.* **2023**, *10*, 1.

[358] K. Dong, H. Zhou, M. Xiao, P. Gui, Z. Gao, F. Yao, W. Shao, C. Liu, C. Tao, W. Ke, G. Fang, *Appl. Phys. Lett.* **2022**, *120*, 0090569.

[359] B. Yu, L. Zhou, F. Wang, *ACS Appl. Mater. Interfaces* **2020**, *12*, 30530.

[360] J. Ma, X. Xia, S. Yan, Y. Li, W. Liang, J. Yan, X. Chen, D. Wu, X. Li, Z. Shi, *ACS Appl. Mater. Interfaces* **2021**, *13*, 15409.

[361] W. Liang, L. Wang, Y. Li, F. Zhang, X. Chen, D. Wu, Y. Tian, X. Li, C. Shan, Z. Shi, *Mater. Today Physics* **2021**, *18*, 100398.

[362] M. Krishnaiah, A. Kumar, D. Mishra, N. Kumar, J. Song, S. Hun Jin, *Mater. Lett.* **2023**, *340*, 134112.

[363] M. Krishnaiah, A. Kumar, S. H. Jin, *Phys. Status Solidi RRL* **2023**, 2300107.

[364] W. Liang, L. Wang, Y. Li, F. Zhang, X. Chen, D. Wu, Y. Tian, X. Li, C. Shan, Z. Shi, *Mater. Today Phys.* **2021**, *18*, 100398.

[365] X. W. Tong, Z. X. Zhang, D. Wang, L. B. Luo, C. Xie, Y. C. Wu, *J. Mater. Chem. C* **2019**, *7*, 863.

[366] S. Shah, A. Bhorde, Y. Hase, R. Aher, V. Doiphode, A. Waghmare, A. Punde, P. Shinde, S. Rahane, B. R. Bade, H. M. Pathan, M. Prasad, M. Aleksandrova, S. P. Patole, S. R. Jadkar, *ACS Appl. Electron. Mater.* **2022**, *4*, 2793.

[367] H. J. Gogoi, K. Bajpai, A. T. Mallajosyula, A. Solanki, *J. Phys. Chem. Lett.* **2021**, *12*, 8798.

[368] M. Lanza, A. Sebastian, W. D. Lu, M. Le Gallo, M. F. Chang, D. Akinwande, F. M. Puglisi, H. N. Alshareef, M. Liu, J. B. Roldan, *Science* **2022**, *376*, 1066.

[369] Q. Liu, S. Gao, L. Xu, W. Yue, C. Zhang, H. Kan, Y. Li, G. Shen, *Chem. Soc. Rev.* **2022**, *51*, 3341.

[370] Y. Sun, D. Wen, *ACS Appl. Electron. Mater.* **2020**, *2*, 618.

[371] C. Cuhadar, S. G. Kim, J. M. Yang, J. Y. Seo, D. Lee, N. G. Park, *ACS Appl. Mater. Interfaces* **2018**, *10*, 29741.

[372] Y. Ren, H. Ma, W. Wang, Z. Wang, H. Xu, X. Zhao, W. Liu, J. Ma, Y. Liu, *Adv. Mater. Technol.* **2019**, *4*, 2.

[373] B. Li, W. Hui, X. Ran, Y. Xia, F. Xia, L. Chao, Y. Chen, W. Huang, *J. Mater. Chem. C* **2019**, *7*, 7476.

[374] D. Li, X. Dong, P. Cheng, L. Song, Z. Wu, Y. Chen, W. Huang, *Adv. Sci.* **2022**, *9*, 1.

[375] Y. Hu, S. Zhang, X. Miao, L. Su, F. Bai, T. Qiu, J. Liu, G. Yuan, *Adv. Mater. Interfaces* **2017**, *4*, 2.

[376] Z. Xiong, W. Hu, Y. She, Q. Lin, L. Hu, X. Tang, K. Sun, *ACS Appl. Mater. Interfaces* **2019**, *11*, 30037.

[377] S. Y. Kim, D. A. Park, N. G. Park, *ACS Appl. Electron. Mater.* **2022**, *37*, 739.

[378] S. G. Kim, Q. Van Le, J. S. Han, H. Kim, M. J. Choi, S. A. Lee, T. L. Kim, S. B. Kim, S. Y. Kim, H. W. Jang, *Adv. Funct. Mater.* **2019**, *29*, 1.

[379] S. Ge, X. Guan, Y. Wang, C. H. Lin, Y. Cui, Y. Huang, X. Zhang, R. Zhang, X. Yang, T. Wu, *Adv. Funct. Mater.* **2020**, *30*, 2002110.

[380] S. Paramanik, A. Maiti, S. Chatterjee, A. J. Pal, *Adv. Electron. Mater.* **2022**, *8*, 1.

[381] C. Sun, F. Luo, L. Ruan, J. Tong, L. Yan, Y. Zheng, X. Han, Y. Zhang, X. Zhang, *ChemPlusChem* **2021**, *86*, 1530.

[382] L. U. O. Feifei, W. U. Yanzhao, T. Junwei, X. U. Dake, Q. I. N. Gaowu, T. Fubo, Z. XianMin, **2023**, *66*, 1141.

[383] F. Luo, Y. Wu, J. Tong, F. Tian, X. Zhang, *Nano Res.* **2023**, *16*, 10108.

[384] K. Kang, W. Niu, Y. Zhang, A. Li, X. Zou, W. Hu, *J. Phys. Chem. Lett.* **2023**, *14*, 347.

[385] X. Cao, Y. Han, J. Zhou, W. Zuo, X. Gao, L. Han, X. Pang, L. Zhang, Y. Liu, S. Cao, *ACS Appl. Mater. Interfaces* **2019**, *11*, 35914.

[386] J. S. Han, Q. Van Le, J. Choi, H. Kim, S. G. Kim, K. Hong, C. W. Moon, T. L. Kim, S. Y. Kim, H. W. Jang, *ACS Appl. Mater. Interfaces* **2019**, *11*, 8155.

[387] Y. Park, J. S. Lee, *ACS Appl. Mater. Interfaces* **2022**, *14*, 4371.

[388] Y. Zheng, D. Yu, H. Lian, H. Yuan, Y. Zhou, S. Yang, *Sci. China Mater.* **2023**, *66*, 2383.

[389] Y. Shao, Y. Fang, T. Li, Q. Wang, Q. Dong, Y. Deng, Y. Yuan, H. Wei, M. Wang, A. Gruverman, J. Shield, J. Huang, *Energy Environ. Sci.* **2016**, *9*, 1752.

[390] Y. Yuan, J. Huang, *Acc. Chem. Res.* **2016**, *49*, 286.

[391] Y. Wang, Y. Yuan, W. Zhang, F. Qi, N. Zhang, T. Liu, X. Tang, *Appl. Phys. Lett.* **2022**, *120*, 263503.

[392] H. Ye, B. Sun, Z. Wang, Z. Liu, X. Zhang, X. Tan, T. Shi, Z. Tang, G. Liao, *J. Mater. Chem. C* **2020**, *8*, 14155.

[393] Y. Yuan, Y. Wang, X. Tang, N. Zhang, W. Zhang, *ACS Appl. Mater. Interfaces* **2022**, *14*, 53990.

[394] X. F. Cheng, W. H. Qian, J. Wang, C. Yu, J. H. He, H. Li, Q. F. Xu, D. Y. Chen, N. J. Li, J. M. Lu, *Small* **2019**, *15*, 1905731.

[395] Y. Wang, N. Xu, W. Zhang, Y. Yuan, F. Qi, N. Zhang, X. Tang, *IEEE Trans. Electron Devices* **2022**, *69*, 6676.

[396] W. H. Qian, X. F. Cheng, J. Zhou, J. H. He, H. Li, Q. F. Xu, N. J. Li, D. Y. Chen, Z. G. Yao, J. M. Lu, *InfoMat* **2020**, *2*, 743.

[397] J. S. Han, Q. Van Le, H. Kim, Y. J. Lee, D. E. Lee, I. H. Im, M. K. Lee, S. J. Kim, J. Kim, K. J. Kwak, M. Choi, S. A. Lee, K. Hong, S. Y. Kim, H. W. Jang, *Small* **2020**, *16*, 2003225.

[398] A. Siddik, P. K. Haldar, T. Paul, U. Das, A. Barman, A. Roy, P. K. Sarkar, *Nanoscale* **2021**, *13*, 8864.

[399] Y. Yuan, Y. Wang, W. Zhang, F. Qi, X. Tang, Z. Wang, *J. Alloys Compd.* **2023**, *937*, 168308.

[400] J. M. Yang, E. S. Choi, S. Y. Kim, J. H. Kim, J. H. Park, N. G. Park, *Nanoscale* **2019**, *11*, 6453.

[401] N. C. Das, M. Kim, J. R. Rani, S. M. Hong, J. H. Jang, *Micromachines* **2021**, *12*, 1049.

[402] B. Hwang, J. S. Lee, *Nanoscale* **2018**, *10*, 8578.

[403] J. Li, Y. Zhang, C. Yao, N. Qin, R. Chen, D. Bao, *Adv. Electron. Mater.* **2022**, *8*, 1.

[404] S. Poddar, Y. Zhang, Y. Zhu, Q. Zhang, Z. Fan, *Nanoscale* **2021**, *13*, 6184.

[405] F. Luo, Y. Wu, J. Tong, G. Qin, X. Zhang, *J. Alloys Compd.* **2023**, *938*, 168498.

[406] T. George, A. V. Murugan, *ACS Appl. Mater. Interfaces* **2022**, *14*, 51066.

[407] D. Liu, Q. Lin, Z. Zang, M. Wang, P. Wangyang, X. Tang, M. Zhou, W. Hu, *ACS Appl. Mater. Interfaces* **2017**, *9*, 6171.

[408] K. Rudrapal, G. Bhattacharya, V. Adyam, A. Roy Chaudhuri, *Adv. Electron. Mater.* **2022**, *8*, 1.

[409] M. Huang, M. Hou, H. Xing, J. Tu, S. Jia, *Ceram. Int.* **2023**, *49*, 10365.

[410] R. Ray, S. K. Pal, *IEEE Electron. Device Lett.* **2021**, *42*, 1284.

[411] Y. Yuan, Y. Wang, X. Tang, N. Zhang, W. Zhang, *ACS Appl. Mater. Interfaces* **2022**.

[412] Y. Zheng, F. Luo, L. Ruan, J. Tong, L. Yan, C. Sun, X. Zhang, *J. Alloys Compd.* **2022**, *909*, 164613.

[413] B. Hwang, J. Lee, *Nanoscale* **2018**, *10*, 8578.

[414] F. Zeng, Y. Tan, W. Hu, X. Tang, Z. Luo, Q. Huang, Y. Guo, X. Zhang, H. Yin, J. Feng, X. Zhao, B. Yang, *J. Phys. Chem. Lett.* **2021**, *12*, 1973.

[415] F. Zeng, Y. Guo, W. Hu, Y. Tan, X. Zhang, J. Feng, X. Tang, *ACS Appl. Mater. Interfaces* **2020**, *12*, 23094.

[416] Z. Guo, R. Xiong, Y. Zhu, Z. Wang, J. Zhou, Y. Liu, D. Luo, Y. Wang, H. Wang, *Appl. Phys. Lett.* **2023**, *122*, 053502.

[417] J. Lao, W. Xu, C. Jiang, N. Zhong, B. Tian, H. Lin, C. Luo, J. Travas-Sejdic, H. Peng, C. G. Duan, *J. Mater. Chem. C* **2021**, *9*, 5706.

[418] T. Zhong, Y. Qin, F. Lv, H. Qin, X. Tian, *Nanoscale Res. Lett.* **2021**, *16*, 1.

[419] T. Tong, C. Liu, J. Xu, H. Min, S. Chen, Y. Lyu, C. Lyu, *J. Mater. Chem. C* **2023**, *11*, 4946.

[420] M. Yeganeh, M. H. Rezvani, S. M. Laribaghal, *Colloids Surf A Physicochem. Eng. Asp.* **2021**, 127120.

[421] A. A. Vasilev, D. S. Saranin, P. A. Gostishchev, S. I. Didenko, A. Y. Polyakov, A. Di Carlo, *Opt. Mater.: X* **2022**, *16*, 100218.

[422] J. Ge, Z. P. Ling, J. Wong, T. Mueller, A. G. Aberle, *Energy Procedia.* **2012**, *15*, 107.

[423] M. W. Swift, J. L. Lyons, *J. Mater. Chem. A* **2021**, *9*, 7491.

[424] J. M. Azpiroz, E. Mosconi, J. Bisquert, F. De Angelis, *Energy Environ. Sci.* **2015**, *8*, 2118.

[425] S. Van Reenen, M. Kemerink, H. J. Snaith, *J. Phys. Chem. Lett.* **2015**, *6*, 3808.

[426] Y. Zhao, W. Zhou, Z. Han, D. Yu, Q. Zhao, *Phys. Chem. Chem. Phys.* **2021**, *23*, 94.

[427] Y. Shao, Y. Fang, T. Li, Q. Wang, Q. Dong, Y. Deng, Y. Yuan, H. Wei, M. Wang, A. Gruverman, *Energy Environ. Sci.* **2016**, *9*, 1752.

[428] P. Calado, A. M. Telford, D. Bryant, X. Li, J. Nelson, B. C. O'Regan, P. R. F. Barnes, *Nat. Commun.* **2016**, *7*, 13831.

[429] G. K. Grandhi, L. K. Jagadamma, V. Sugathan, B. Al-Anesi, D. Manna, P. Vivo, *Chem. Commun.* **2023**, *59*, 8616.

[430] G. Liu, Y. Wu, Y. Liu, B. Cai, Y. Dong, S. Zhang, H. Zeng, *Appl. Phys. Lett.* **2021**, *119*, 031902.

[431] N. K. Tailor, A. Mahapatra, A. Kalam, M. Pandey, P. Yadav, S. Satapathi, *Phys. Rev. Mater.* **2022**, *6*, 045401.

[432] M. T. Sirtl, F. Ebadi, B. T. van Gorkom, P. Ganswindt, R. A. J. Janssen, T. Bein, W. Tress, *Adv. Opt. Mater.* **2021**, *9*, 2100202.

[433] M. Stolterfoht, C. M. Wolff, J. A. Márquez, S. Zhang, C. J. Hages, D. Rothhardt, S. Albrecht, P. L. Burn, P. Meredith, T. Unold, *Nat. Energy* **2018**, *3*, 847.

[434] N. Li, X. Niu, Q. Chen, H. Zhou, *Chem. Soc. Rev.* **2020**, *49*, 8235.

[435] M. Shahiduzzaman, L. Wang, S. Fukaya, E. Y. Muslih, A. Kogo, M. Nakano, M. Karakawa, K. Takahashi, K. Tomita, J. M. Nunzi, T. Miyasaka, T. Taima, *ACS Appl. Mater. Interfaces* **2021**, *13*, 21194.

[436] P. Caprioglio, D. S. Cruz, S. Caicedo-Dávila, F. Zu, A. A. Sutanto, F. Peña-Camargo, L. Kegelmann, D. Meggiolaro, L. Gregori, C. M. Wolff, B. Stiller, L. Perdigón-Toro, H. Köbler, B. Li, E. Gutierrez-Partida, I. Lauermann, A. Abate, N. Koch, F. De Angelis, B. Rech, G. Grancini, D. Abou-Ras, M. K. Nazeeruddin, M. Stolterfoht, S. Albrecht, M. Antonietti, D. Neher, *Energy Environ. Sci.* **2021**, *14*, 4508.

[437] Y. Zhan, Q. Cheng, J. Peng, Y. Zhao, F. Vogelbacher, X. Lai, F. Wang, Y. Song, M. Li, *Nano Energy* **2022**, *98*, 107254.

[438] W. Cheng, W. Tian, F. Cao, L. Li, *InfoMat* **2022**, *4*, 1.

[439] B. Li, Y. Zhang, L. Fu, T. Yu, S. Zhou, L. Zhang, L. Yin, *Nat. Commun.* **2018**, *9*, 1.

[440] M. Li, Y. G. Yang, Z. K. Wang, T. Kang, Q. Wang, S. H. Turren-Cruz, X. Y. Gao, C. S. Hsu, L. S. Liao, A. Abate, *Adv. Mater.* **2019**, *31*, 1.

[441] W. Cheng, X. He, J. G. Wang, W. Tian, L. Li, *Adv. Mater.* **2022**, *34*, 1.

G. Krishnamurthy Grandhi received his Ph.D. in materials chemistry from Jawaharlal Nehru Centre for Advanced Scientific Research in 2017. Currently, he is a postdoctoral fellow at Hybrid Solar Cells group at Tampere University. His research interests mainly focus on the synthesis of halide perovskite-based nanocrystals and thin films for optoelectronic applications, particularly photovoltaics.

Diego Solis-Ibarra received his Bachelor's (with Honors, '08) and Ph.D. ('12) from UNAM under Vojtech Jancik's supervision. During this time, he spent a semester as an exchange student at UC Santa Barbara and one year as a research intern at MIT under Christopher Cummins'' tutelage. Following his Ph.D., he moved to Stanford University as postdoctoral researcher in Hema Karunadasa's group. In 2015, he returned to UNAM as an assistant professor at the Instituto de Investigaciones en Materiales, where he is currently a Full Professor. Recently, Diego has been selected as one of ACS' Chemical and Engineering News Talented 12.

Feng Gao is a professor at Linköping University in Sweden. He received his Ph.D. from the University of Cambridge (UK) in 2011, followed by a Marie Curie postdoc fellowship at Linköping University. His group currently focuses on research into solution-processed energy materials and devices, mainly based on organic semiconductors and metal halide perovskites.

Robert L. Z. Hoye is an associate professor in the Department of Chemistry at the University of Oxford. He completed his Ph.D. at the University of Cambridge (2012–2014), before working as a postdoctoral researcher at the Massachusetts Institute of Technology (2015–2016), followed by two College Research Fellowships at Cambridge, first at Magdalene College (2016–2019), then at Downing College (2019–2020). He moved to Imperial College London in 2020 as a Lecturer, then Senior Lecturer in 2022, before moving to Oxford later in 2022. His research focusses on defect-tolerant semiconductors, and their development into optoelectronic devices.

Paola Vivo is an associate professor at Tampere University (TAU). After pursuing her Ph.D. in chemistry (2010), she received several major grants as Principal Investigator, including the prestigious Academy of Finland Fellowship for postdoctoral research in 2013–2017. She currently leads the Hybrid Solar Cells group (https://www.research.tuni.fi/hsc/) at the Faculty of Engineering and Natural Sciences at TAU. Her research interests include developing novel materials for solar energy applications, with main emphasis on halide perovskites and perovskite-inspired materials.